

**Verification of Monte Carlo Transport Codes by  
Activation Experiments**

Dissertation  
zur Erlangung des Doktorgrades  
der Naturwissenschaften

vorgelegt beim Fachbereich Physik  
der Johann Wolfgang Goethe-Universität  
in Frankfurt am Main

von  
Vera Chetvertkova  
aus Obninsk, Russland

Frankfurt 2012

(D 30)

Vom Fachbereich Physik der

Johann Wolfgang Goethe-Universität als Dissertation angenommen.

Dekan: Prof. Dr. Michael Huth

Gutachter: Prof. Dr. Ulrich Ratzinger

Prof. Dr. Oliver Kester

Datum der Disputation: 18. Dezember 2012

# Contents

Zusammenfassung	v
Abstract	xv
Introduction.....	- 1 -
Chapter 1. Description of the MC codes: FLUKA, MARS and SHIELD.....	- 11 -
1.1. Transport module.....	- 12 -
1.1.1. FLUKA.....	- 12 -
1.1.2. SHIELD.....	- 15 -
1.1.3. MARS.....	- 19 -
1.2. Nuclide production module.....	- 21 -
1.2.1. FLUKA.....	- 21 -
1.2.2. SHIELD.....	- 24 -
1.2.3. MARS.....	- 27 -
Chapter 2. Experimental technique.....	- 31 -
2.1. Preliminary simulations.....	- 31 -
2.2. Types of targets.....	- 36 -
2.3. Irradiation and Measurements.....	- 38 -
2.4. Analysis of the Gamma-spectra.....	- 41 -
2.5. Uncertainty Assessment.....	- 48 -
Chapter 3. Experimental results and comparison with the simulations.....	- 51 -
3.1. Activation of aluminum.....	- 51 -
3.1.1. Activation of aluminum by a nitrogen beam.....	- 51 -
3.1.2. Activation of aluminum by an argon beam.....	- 54 -
3.1.3. Activation of aluminum by a uranium beam.....	- 56 -
3.2. Activation of copper.....	- 67 -
3.2.1. Activation of copper by a nitrogen beam.....	- 67 -
3.2.2. Activation of copper by an argon beam.....	- 72 -

## Contents

---

Chapter 4. Discussion.....	- 79 -
4.1. Thin target approach.....	- 79 -
4.2. Thick target approach.....	- 82 -
4.3. Activation studies for accelerator applications.....	- 89 -
Conclusion and Outlook.....	- 99 -
References.....	- 104 -
Acknowledgements.....	- 115 -
Curriculum Vitae.....	- 118 -



---

---

---

## Zusammenfassung

Die Aktivierung von Beschleunigerkomponenten durch Strahlverluste ist einer der wichtigsten Faktoren der Intensitätsbegrenzung für hochenergetische und hochintensive Hadronenbeschleuniger [1 – 3]. Erhöhte Dosisleistungen in der Nähe von bestrahlten Materialien erschweren die Hands-On-Wartung der Maschine. Daher ist eine Beschleunigerabschirmung notwendig, welche eine Strahlenexposition für das Personal während der Servicezeiten minimiert. Die Tatsache, daß bei hohen Intensitäten die Projektil-Target-Wechselwirkungen zunehmen und auf der anderen Seite bei hohen Energien die Eindringtiefe der Ionen größer ist, verstärkt diese Problematik. Deshalb ist die Aktivierung von Beschleunigerkomponenten von großem Belang für die „Facility for Antiproton and Ion Research“ (FAIR). Diese Anlage sieht eine Beschleunigung von  $5 \cdot 10^{11}$   $U^{28+}$  Ionen pro Puls bis zu einer Energie von 2.7 AGeV vor [5]. In diesem Fall wären gewöhnliche Verluste von nur wenigen Promille so intensiv wie der gesamte Strahl im Schwerionensynchrotron SIS18, der im GSI Helmholtzzentrum für Schwerionenforschung derzeit läuft. Dies führt zur Notwendigkeit einer Messung der Restaktivität in den Tiefenschichten von bestrahlten Festkörpern. Folgende Experimente fanden an der GSI statt: Edelstahl- und Kupfer-Targets wurden mit  $^{238}U^{+73}$  Uran bei 500 AMeV und 950 AMeV [6, 7], und Kupfer-Targets mit  $^{40}U^{+18}$  Ionen bei 500 AMeV und 1 AGeV [8] bestrahlt. Die Ergebnisse der Messungen führten dazu, Strahlverlust-Kriterien für Schwerionenbeschleuniger aufzustellen, um hohe Dosisraten in den Experimentierhallen zu vermeiden und eine Hands-On-Wartung der Maschine [9] zu ermöglichen. Diesen Kriterien liegt das „1 W/m – Kriterium“ für Protonenbeschleuniger zugrunde. Diese Skalierung ist möglich, weil festgestellt wurde, dass im Energiebereich oberhalb von 200 AMeV die Radionuklidproduktion unabhängig von der Projektilart ist, also die Zeit-Abhängigkeiten der relativen Aktivitäten und die jeweiligen Dosisraten gleich sind.

Die Schwerionen-Strahlverlust-Kriterien basieren auf Monte-Carlo-Berechnungen mit den Transportcodes FLUKA und SHIELD. Monte Carlo Transportcodes sind die

Werkzeuge für die Berechnung der Bewegung und Wechselwirkung von Teilchen mit Materie. Neben vielfältigen Anwendungen in Kern-, Teilchen- und Medizinphysik verwendet man sie in Beschleunigeranlagen für das Design von Beamstops und Strahlabschirmungen, wo die Aktivierung von Materialien und jeweiligen Dosisraten während Betrieb und Abschaltung von Interesse sind.

Die Schwerionen-Versionen der Monte Carlo Transportcodes wurden etwa vor fünfzehn Jahren eingeführt. Überprüft wurden diese Versionen vor allem durch den Vergleich mit den experimentellen Daten über Energiedeposition, Aktivierung von dicken Targets durch Protonenstrahlen und Wirkungsquerschnitte für die Neutronenproduktion und für die Spaltung von schweren Kernen mit Neutronen [26 – 32]. Die Aktivierung durch Protonenstrahlen konnte nicht ausreichend auf die Aktivierung durch Schwerionenstrahlen übertragen werden. Es gibt nur wenige Daten für die Aktivierung der Materialien durch Schwerionenstrahlen: publiziert sind jene Experimente an der GSI [6 – 8; 33 – 35]; die Aktivierung von Kupfer mit 278 AMeV Stickstoff am PPA (Princeton Particle Accelerator) [32]; mit 2083 AMeV Kohlenstoff, 2 AGeV Argon, 211 AMeV und 377 AMeV Neon am Bevalac [30, 36, 37]; mit 135 AMeV Kohlenstoff am RIKEN [38] und mit 200 AMeV Kohlenstoff am TWA-ITEP [39]; außerdem die Experimente mit Silber und 2.1 AGeV Kohlenstoff am Bevalac [31], und solche mit verschiedenen Targets (C, Al, Cr, Fe, Ni, Cu, Pb) und verschiedenen Ionen (He, C, Ne, Ar und Si) am HIMAC [40 – 45].

Die Verifikation der Monte-Carlo-Codes durch Aktivierungsexperimente mit Ionenstrahlen hat mehrere Vorteile im Vergleich zu der mit Messdaten der sekundären Neutronen. Zunächst werden die Primärteilchen beim Durchgang durch Materie aufgespalten: die schweren und leichten Ionen-Fragmente werden meist in der Tiefe von zwei Eindringtiefen des Primärstrahls gestoppt, während die sekundären Neutronen weiter durchdringen, daher sind sie nur indirekte Indikatoren für erzeugte schwerere Fragmente. Deshalb würden Simulationen, wenn sie präzise Ergebnisse für Projektil-Fragmente in der Tiefe der zweifachen Reichweite Primärionen gäben, auch gute Ergebnisse für die Anzahl der sekundären Neutronen in den weiteren Regionen liefern. Da das Target sowohl durch den Primärstrahl als auch durch Sekundärteilchen aktiviert wird, werden die Target-Fragmente im gesamten Targetvolumen auftauchen.

---

Art und Menge dieser restlichen Kerne kann in den Aktivierungsexperimenten erforscht werden, was direkte Informationen über das Strahlenrisiko nach Strahlabschaltung [9, 46] impliziert, wohingegen sekundäre Neutronen die Zunahme der Dosisrate in der Nähe der Beschleunigerkomponenten während die Strahlzeit offenlegt. Schließlich kann eine Tiefenprofilmessung der partiellen Restaktivitäten durchgeführt werden, um eine komplette Übersicht über die Performance der Codes zu liefern. Zusammenfassend ermöglichen die Aktivierungsexperimente die Überprüfung von Transport und nuklearer Erzeugung explizit durch den Vergleich der Typen, der Häufigkeit und der Tiefenprofils der Radionuklide, die im bestrahlten Material erzeugt oder gestoppt werden.

Die meisten der obengenannter Experimente [6 – 8; 30 – 45] liefern Informationen über die Wirkungsquerschnitte und nicht über die Tiefenprofile. Die Tiefenprofile wurden gemessen für die Aluminium und Kupfer Targets bestrahlt mit leichten ( $Z = 2 \div 18$ ) Ionen bei niedrigen Energien bis 230 AMeV [40, 41]; für die Kupfer Targets bestrahlt mit 500 AMeV und 1 AGeV Argon sowie mit 500 AMeV und 950 AMeV Uran ( $Z = 92$ ); und auch für die Edelstahl Targets bestrahlt mit 500 AMeV und 950 AMeV Uran. Für eine vollständigere Verifizierung der Monte-Carlo-Transportcodes ist es wichtig, die Aktivierung bei den anderen Projektil-Target-Kombinationen zu erforschen. Die erhaltenen Ergebnisse würden nicht nur eine Bestätigung dieser Monte-Carlo-Transportcodes ermöglichen, sondern auch deren weitere Entwicklung.

In der vorliegenden Arbeit wurden die Codes FLUKA, MARS und SHIELD für die Verifizierung gewählt. Im Überblick werden die Theorien für die sogenannten „transport“ and „nuclide production“ Module dieser Codes beschrieben. „Transport modules“ stehen für die Berechnung der Coulomb-Streuung, der elektrischen and nuklearen Bremskraft und der Ionisationschwankungen. Das „nuclear stopping module“ ist zuständig für die Wahl der Art der Wechselwirkung (elastisch/unelastisch) und für die Berechnung der Anzahl der Nuklide bestimmter Arten nach einer inelastischen Wechselwirkung. Alle drei Codes wurden so entwickelt, dass die eingebundenen Standardmodelle für nukleare Wechselwirkungen nicht geändert werden können.

Der Schwerpunkt der vorliegenden Studie war die Messung der Restaktivität im

## Zusammenfassung

---

Material, hervorgerufen durch Ionenstrahlen verschiedener Spezies: Stickstoff ( $Z = 7$ ), Argon ( $Z = 18$ ) und Uran ( $Z = 92$ ). Als zu bestrahlende Materialien wurden Aluminium und Kupfer ausgewählt. Aluminium wurde gewählt, weil es ein Material mit relativ niedrigem  $Z$  ( $Z = 13$ ) ist und Kupfer ist ein Material mit mittlerem  $Z$  ( $Z = 29$ ). Im Hinblick auf Beschleunigeranwendungen sollten Aluminiumkomponenten in den Bereichen mit hohen Strahlverlusten bevorzugt werden, da dieses Material offenbar weniger aktiviert wird als Hoch- $Z$ -Materialien, und Kupfer ist ein übliches Material für die Spulen der Magnete. Außerdem ergänzt diese Arbeit zuvor durchgeführte Experimente mit Kupfer [6 – 8] durch zusätzliche Projekttilarten.

Andere Ziele waren, die Grenzen der Anwendbarkeit der Schwerionenstrahlverlust-Kriterien zu erforschen und herauszufinden, welches Material in Beschleunigeranwendungen bezüglich des Strahlenschutzes zu bevorzugen ist.

Die experimentellen Daten wurden unter Verwendung der „Methode der induzierten Aktivität“ erhalten. Das allgemeine Schema dieser Methode besteht in zwei Schritten: Erstens in der Bestrahlung des Targets und zweitens in der Messung der restlichen  $\gamma$ -Aktivität.

Die zu untersuchenden Größen waren: die Art der erzeugten Radionuklide in den

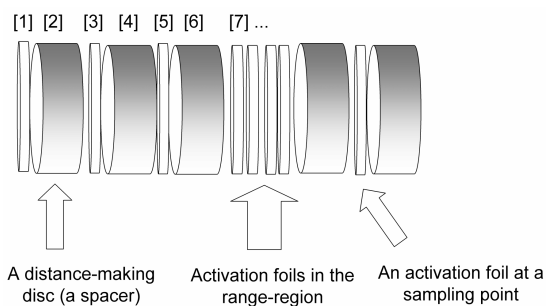


**Abb. 1. Das Schema der dicken Targets**

bestrahlten Targets, die jeweilige Anzahl von Radionukliden pro Primärteilchen und ihre Tiefenprofile. Zwei Arten von Targets wurden bestrahlt: gestapelte Folien- und Einzelfolien-Targets.

Die gestapelten Folien wurden verwendet, um die Erzeugung der radioaktiven Kerne und die Anzahl von Radionukliden in der Tiefe zu untersuchen. Die Targets sind aus dünnen Aktivierungsfolien und dicken Abstandshaltern aus dem gleichen Material (Abb. 1) aufgebaut. Die Abstandshalter wurden verwendet, um die Zunahme von Unsicherheiten in der Tiefe, verursacht

---

durch eine Vielzahl von dünnen Platten, zu vermeiden. Die Dicke der Aktivierungsfolien wurde so ausgewählt, dass (1) die Aktivierungstiefenprofile eine gute Auflösung im interessanten Bereich aufweisen und (2) die Eigenabsorption der  $\gamma$ -Quanten in der Folie ignoriert werden kann.

Die vorausgehenden Simulationen wurden durchgeführt, um die Targetkonfiguration, die Bestrahlungsbedingungen und  $\gamma$ -Spektroskopie-Einstellungen auszuwählen. Drei Parameter wurden berechnet: Die Eindringtiefe der ausgewählten Ionen in den interessierenden Materialien, Restaktivitäten der Nuklide in den bestrahlten Targets und die Dosisraten in der Nähe der bestrahlten Targets.

Die Information über die Eindringtiefe des Primärstrahls wurde für die Wahl der Gesamtdicke des Targets (wie oben erwähnt, sollte die Gesamtdicke der Target nicht weniger als zwei Eindringtiefen der Primärionen sein) und zur optimalen Positionierung der verwendeten Aktivierungsfolien benutzt. Die Eindringtiefe der Ionen wurde mithilfe von ATIMA [64] und FLUKA [19 – 20] berechnet. Um deren Genauigkeit grob abzuschätzen, wurden ergänzende Experimente mit einem diagonal durchgeschnittenen Zylindertarget, dessen Schnittfläche mit einer organischen Folie (Polyetheretherketon, PEEK) abgedeckt war, durchgeführt. Die Skizze eines solchen Targets ist in der Abb. 2 zu sehen. Dieses Verfahren basiert auf der Idee, dass die PEEK-Folie proportional zur Energiedeposition dunkler wird; damit würde die maximale Schwärzung die Position der Eindringtiefe anzeigen. Die Genauigkeit eines solchen Verfahrens hängt von der Geometrie des Zylinders ab.

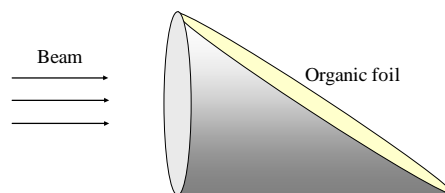


**Abb. 2. Der abgeschnittene Zylinder, mit PEEK-Folie abgedeckt**

Die jeweiligen Restaktivitäten der Radionuklide wurden berechnet, um herauszufinden, welche Bestrahlungszeit erforderlich ist, um die ausreichende Menge an Nukliden von Interesse zu erzeugen. Die Dosisraten wurden simuliert, um die Abkühlzeit nach der Bestrahlung abschätzen.

Aus Strahlenschutzgründen konnten hoch aktivierte dicke Targets nicht unmittelbar nach der Bestrahlung untersucht werden, daher konnten die kurzlebigen

## Zusammenfassung

Nuklide mit dieser Geometrie nicht ermittelt werden. Aus diesem Grund wurde eine Einzeltargetfolie bestrahlt. Die Dicke der Probe sollte ermöglichen, daß einerseits Energieverluste und  $\gamma$ -Quanten-Absorption in der Probe vernachlässigt werden konnten und andererseits die Bestrahlungszeit überschaubar wird und somit eine gute Statistik erhalten werden kann. Allerdings sollte man bei der Wahl der Targetdicke und der Bestrahlungszeit für die dünnen Folien die Erzeugungsrate der interessanten Kerne im Hinterkopf behalten.

Die bestrahlten Einzelfolientargets und Aktivierungsfolien aus den dicken Targets wurden mittels  $\gamma$ -Spektroskopie [125] untersucht. Die Messungen der restlichen  $\gamma$ -Aktivität wurden mit einem High Purity Germanium (HPGe)-Detektor durchgeführt.

Die Experimente wurden am Schwerionensynchrotron SIS 18 der GSI durchgeführt.

Die dünnen Aluminium-Folien werden bestrahlt mit

- 426 AMeV  $^{40}\text{Ar}^{18+}$ ;
- 85, 174, 279, 325, 381, 483, 584, 684, 785 and 935 AMeV  $^{238}\text{U}^{73+}$ .

Die dicken Aluminium-Targets wurden mit 498 AMeV Stickstoff  $^{14}\text{N}^{7+}$ , 496 AMeV Argon  $^{40}\text{Ar}^{18+}$  und 483 AMeV Uran  $^{238}\text{U}^{73+}$  und die dicken Kupfer-Targets wurden mit 498 AMeV Stickstoff und 496 AMeV Argon bestrahlt. Ein Experiment mit einem dicken Kupfer-Target und einem 496 AMeV Argonstrahl war eine Erweiterung einer früheren Untersuchung [8]: die Tiefenprofile der Aktivierung hinter

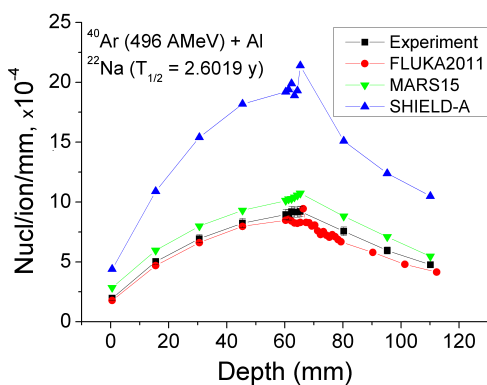


Abb. 3. Die Tiefenprofile der  $^{22}\text{Na}$ -Isotope im Aluminium-Target bestrahlt mit einem 496 AMeV Argonstrahl (die Zahlen sind am Ende der Bestrahlung gegeben).

der Eindringtiefe der Primärteilchen wurden mit einer höheren Auflösung erhalten.

Das experimentelle Tiefenprofil des  $^{22}\text{Na}$  im Aluminium-Targets, bestrahlt mit einem 496 AMeV Argonstrahl, ist zusammen mit den Tiefenprofilen, die mit FLUKA, MARS und SHIELD berechnet worden sind, als Beispiel in Abb. 3 angegeben.



Fünf dicke und zehn Einzelfolientargets wurden für die vorliegende Doktorarbeit bestrahlt. Mehr als 5000 Spektren wurden gemessen und analysiert, insgesamt 45 Tiefenprofile verschiedener Nuklide in den durchgeführten Experimenten erhalten.

Die experimentellen Ergebnisse wurden mit FLUKA, MARS und SHIELD verglichen. Das Stoppen der Ionen mit Energien von bis zu 500 AMeV wird von allen drei Codes gut beschrieben. Gemäß den durchgeführten Experimenten und Simulationen wird die Gesamtzahl der erkannten Nuklide im gesamten Targetvolumen von FLUKA mit durchschnittlich ~ 5% Abweichung, durch MARS mit einer ~ 15%-igen Abweichung angegeben, und SHIELD unterscheidet sich um ca. 50% vom Experiment.

Die Grenzen der Anwendbarkeit der Schwerionenstrahlverlust-Kriterien wurden untersucht. Es wurde festgestellt, dass bei Energien unterhalb von 200 AMeV die Zeitabhängigkeit der Restaktivität im Target durch keine allgemeine Kurve beschrieben werden kann, daher konnte auch keine Extrapolation durchgeführt werden. Die Dosisleistungen für jedes Targetmaterial and jede Bestrahlungsbedingung mussten separat berechnet werden (z.B. Abb. 4).

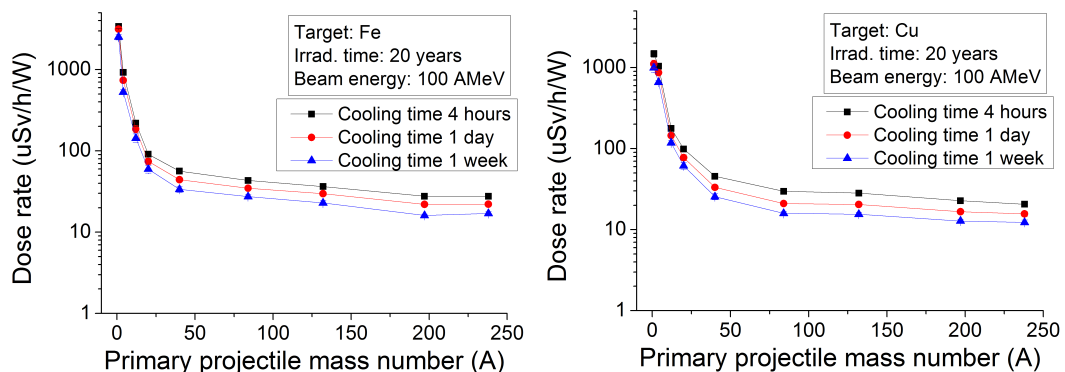


Abb. 4. Maximale Dosisleistungen in Abstand von 30 cm von der Eisen Target (links) und von der Kupfer Target (rechts), die mit 100 AMeV verschiedenen Ionen bestrahlt für 20 Jahre werden, am verschiedene Abklingzeiten.

Die Uran-strahlverlust-Kriterien, die Hands-On-Wartung (Dosisleistung weniger als 1 mSv/h in Abstand von 30 cm von der Oberfläche) der Eisen und Kupfer Komponenten erlauben, sind in Abb. 5 angegeben, für 100-tägige und 20-Jährige Bestrahlung, und für verschiedene Abklingzeiten.

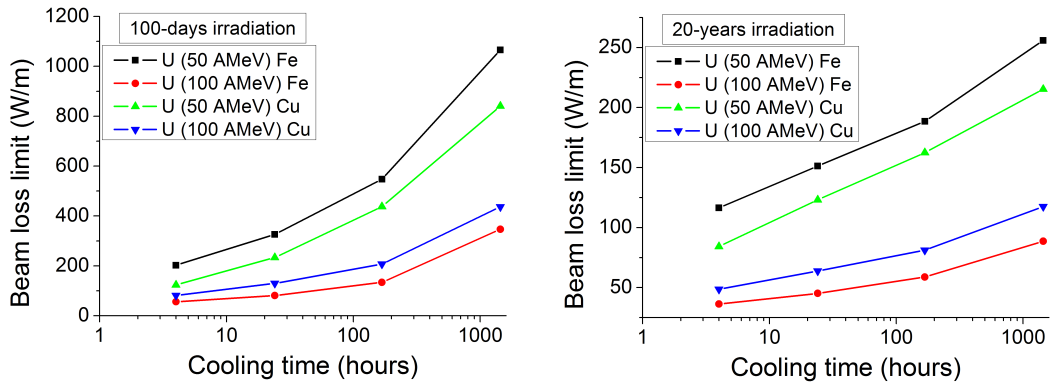


Abb. 5. Abklingzeitabhängigkeit von Uran-strahlverlust-Kriterien die Hands-On-Wartung der Eisen und Kupfer Komponenten, bestrahlt mit 50 AMeV und 100 AMeV Uran, erlauben, für verschiedene Abklingzeiten, und für 100-tägige (links) und 20-Jährige (rechts) Bestrahlung.

Die Schwerionenstrahlverlust-Kriterien für 4 Stunden Abklingzeit, 50 AMeV und 100 AMeV Uran und 100-Tage Bestrahlung sind 200 W/m und 55 W/m für Eisen; 120 W/m und 80 W/m für Kupfer (Abb. 5, links). Wenn die Bestrahlung 20 Jahre dauert und die Abklingzeit auch 4 Stunden ist, lauten die Kriterien entsprechend 120 W/m und 40 W/m für Eisen; 85 W/m und 50 W/m für Kupfer (Abb. 5, rechts).

Die Stichhaltigkeit von FLUKA für niedrige Energie ist noch nicht durchgehend bestätigt, aber der Vergleich von FLUKA mit diesen Experimenten zeigt gute Übereinstimmung.

Die Aktivierung derjenigen Materialien, die am häufigsten in Beschleunigern verwendet werden, wurde durchgeführt. Die Aktivierung von Komponenten aus rostfreiem Stahl (Ti, Cr, Mn, Fe, Ni, Nb, Mo) und anderen Materialien für Maschinenkomponenten oder Abschirmung (C, Al, Cu, Pb) wurde untersucht. FLUKA-Simulationen wurden durchgeführt, um die Gesamtaktivität in dicken Targets und die Dosisleistung im Abstand von 30 cm von der Targetoberfläche zu ermitteln. Dabei wurde angenommen, dass das Target 20 Jahre lang mit 1 GeV Protonen bestrahlt wurde.

Die Targets aus Nickel, Kupfer, Niob, Molybdän und Blei hatten die höchste Gesamtaktivität (Abb. 6). Dabei waren die Dosisleistungen im Abstand von 30 cm von der Targetfläche (Abb. 7) am höchsten für Nickel, Niob und Molybdän, sodass der Anteil dieser Materialien in den Beschleunigerkomponenten minimiert werden muss. Die Dosisleistungen in der Nähe der Targets aus Kohlenstoff, Aluminium, Titan, Chrom, Mangan, Eisen, Kupfer und Blei waren mindestens zweimal niedriger; deshalb können aus Sicht der Hands-On-Wartung diese Materialien eher verwendet werden. Bei langer Bestrahlung und Kühlzeit zeigten Aluminium, Titan, Mangan, Nickel und Kupfer die höchste Dosisleistung im Abstand 30 cm von der Targetoberfläche. Dies sollte berücksichtigt werden, wenn lange Bestrahlungszeiten vorgesehen sind und ferner eine Lagerung der bestrahlten Materialien erforderlich ist.

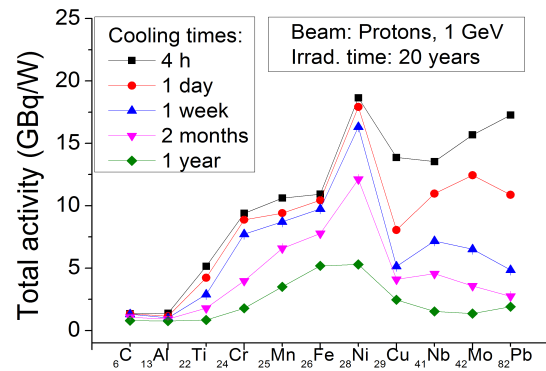


Abb. 6. FLUKA-Simulationsrechnungen der Gesamtaktivitäten von dicken Targets, die mit einem 1 GeV Protonenstrahl für 20 Jahre bestrahlt wurden, pro 1-W Strahl für verschiedene Abklingzeiten.

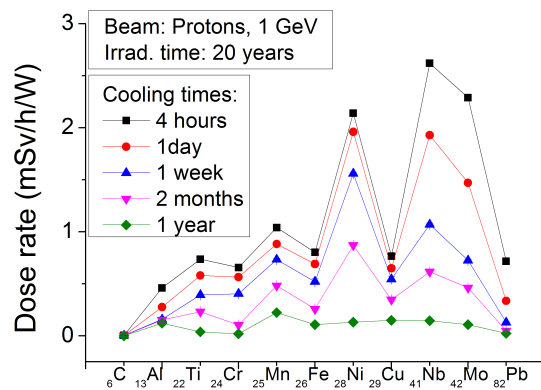


Abb. 7. Zugehörige maximale Dosisleistung im Abstand von 30 cm von der Oberfläche der Targets.

---

---

## Abstract

With the increasing energies and intensities of heavy-ion accelerator facilities, the problem of an excessive activation of the accelerator components caused by beam losses becomes more and more important. Numerical experiments using Monte Carlo transport codes are performed in order to assess the levels of activation. The heavy-ion versions of the codes were released approximately a decade ago, therefore the verification is needed to be sure that they give reasonable results. Present work is focused on obtaining the experimental data on activation of the targets by heavy-ion beams. Several experiments were performed at GSI Helmholtzzentrum für Schwerionenforschung. The interaction of nitrogen, argon and uranium beams with aluminum targets, as well as interaction of nitrogen and argon beams with copper targets was studied. After the irradiation of the targets by different ion beams from the SIS18 synchrotron at GSI, the  $\gamma$ -spectroscopy analysis was done: the  $\gamma$ -spectra of the residual activity were measured, the radioactive nuclides were identified, their amount and depth distribution were detected. The obtained experimental results were compared with the results of the Monte Carlo simulations using FLUKA, MARS and SHIELD. The discrepancies and agreements between experiment and simulations are pointed out. The origin of discrepancies is discussed. Obtained results allow for a better verification of the Monte Carlo transport codes, and also provide information for their further development. The necessity of the activation studies for accelerator applications is discussed. The limits of applicability of the heavy-ion beam-loss criteria were studied using the FLUKA code. FLUKA-simulations were done to determine the most preferable from the radiation protection point of view materials for use in accelerator components.

---

## INTRODUCTION

Activation of the accelerator components caused by the beam losses is one of the main intensity limiting factors for high energy and high intensity hadron accelerators [1 – 3]. It is the reason of the increased dose rates in the vicinity of the irradiated materials and therefore it puts restrictions on the hands-on maintenance of the machine and leads to the necessity of designing the accelerator shielding to avoid personnel exposure during the shutdown. This issue becomes more important at high beam intensities because of the increased number of projectile-target interactions, and at high energies because the beams are able to penetrate deeper through the matter. Moreover the higher the energy, the more channels of interaction become possible, the more types of particles are produced and the multiplicity of products is higher [4].

Activation studies of the accelerator relevant materials were started at GSI Hemholtzzentrum für Schwerionenforschung within the preparation for the high-current Facility for Antiproton and Ion Research (FAIR). This facility will be able to accelerate protons up to 29 GeV and uranium  $U^{28+}$  ions up to 2.7 AGeV. The intensities will be  $2.5 \cdot 10^{13}$  protons and  $3 \cdot 10^{11}$  uranium ions per pulse [5]. For a safe operation at such high intensities, of course, the beam losses should be avoided, however it is not always possible. The routine losses of just a few per mille would be as intense as a complete beam loss in the existing GSI heavy ion synchrotron SIS18. This brought the necessity of quantifying the residual activity induced by beam particles per unit thickness. Experiments were performed at GSI: stainless steel and copper targets were irradiated by  $^{238}U^{73+}$  beams at 500 AMeV and 950 AMeV [6; 7], and copper targets were irradiated by  $^{40}Ar^{18+}$  beams at 500 AMeV and 1 AGeV [8]. The results of the measurements inspired to establish the beam-loss criteria for heavy-ion accelerators in order to avoid high dose rates in the experimental halls and to allow for hands-on maintenance of the machine [9].

The heavy-ion beam-loss criteria were set by scaling the “1 W/m” proton beam-loss limit. In case of protons it was found from operation experience and proved by calculations that losing 1 W/m of a beam with an energy of about 1 GeV during 100 days of continuous operation is tolerable for the hands-on maintenance of the machine

## Introduction

four hours after shutdown, because it corresponds to a dose rate below 1 mSv/h at the distance 30 cm from the component surface [10; 11]. The beam-loss criteria for heavy ions satisfy the same dose rate restrictions. They were calculated for the same irradiation conditions and for two scenarios: (a) activation of a 2 mm thick beam pipe which models beam losses in the straight sections of the machine and (b) activation of a bulky target which models beam losses in bulky components like yokes and coils of the magnets. The study took into account production of the radioactive nuclei with a half-life below a few years. It was shown that the

nuclide inventory in the target does not strongly depend (Fig. 1) on the projectile species in the energy range between 0.2 and 1 AGeV because the main contribution comes from the target fragments, thus the evolution of the activity in the target would also be the same and would correlate to a generic curve (Fig. 2) [9]. Besides, the study

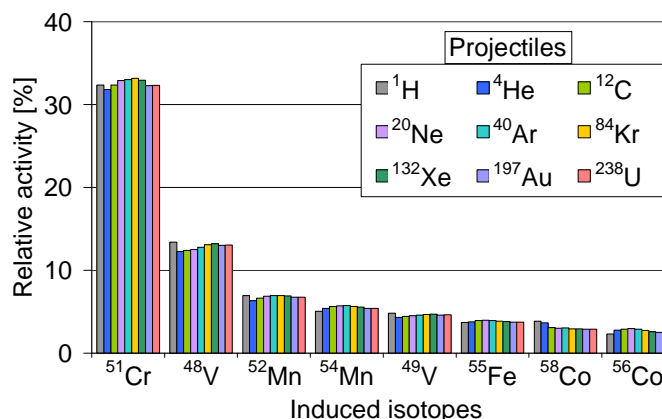


**Fig. 1. Relative activities of the isotopes induced by different beams of 1 AGeV in the stainless steel 304<sup>1</sup> beam pipe; cooling down time 1 day [9].**

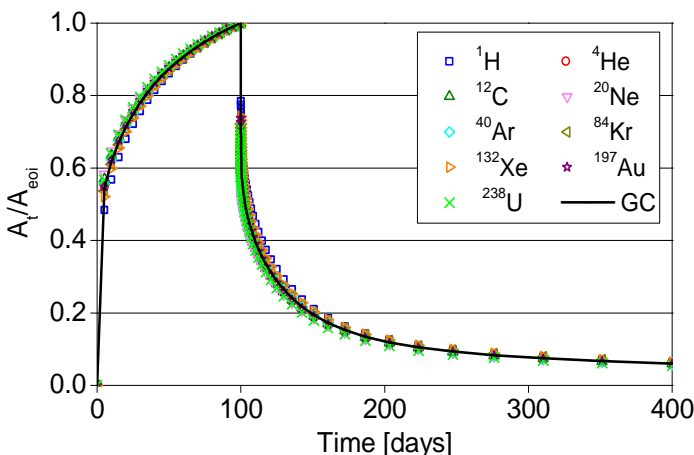


**Fig. 2. Relative activity dependence on time.  $A_t$  is the activity induced in the beam pipe by different projectiles at 500 AMeV as a function of time;  $A_{eoi}$  is the induced activity at the end of irradiation. The generic curve (GC) is an average of the data points corresponding to different primary ions [9].**

<sup>1</sup> Stainless steel 304 composition: Fe (69.4 wt%), C (0.07 wt%), Mn (2.0 wt%), Si (1.0 wt%), Cr (18 wt%), Ni (9.5 wt%) and S (0.03 wt%)



included the activity dependence on beam energy and on an ion species. It was found that the total activity induced in the beam pipe by a 1 W/m beam is decreasing with increasing ion mass and decreasing energy (Fig. 3).

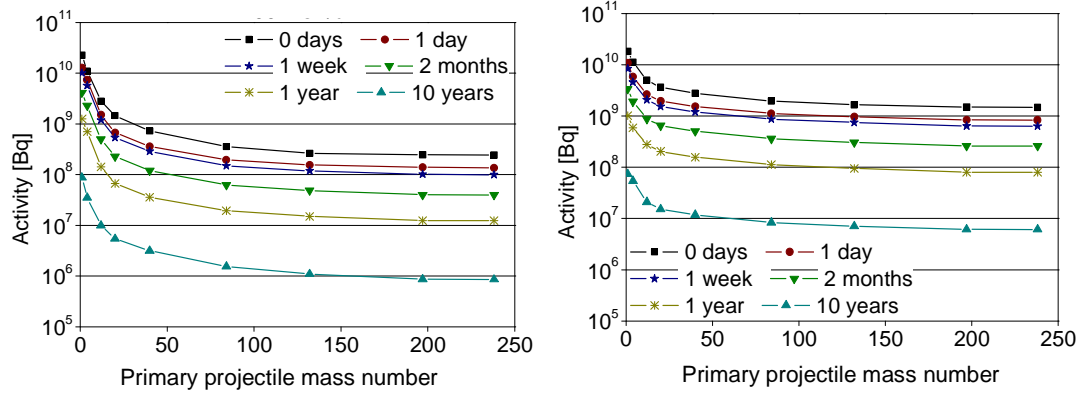


**Fig. 3.** FLUKA-simulations of the activity of the stainless steel 304 beam pipe induced by 1 W/m of primary beam loss at 200 AMeV (left) and at 1 AGeV (right) at different cooling times [9].

These findings made the scaling factor possible: it was calculated as a ratio of the total activity induced in the target by a 1 W/m proton beam at 1 GeV,  $A_p(1 \text{ GeV})$ , to the total activity induced by a 1 W/m beam of interest at a given energy  $A_i(E)$ . The tolerable levels of the beam losses in the stainless steel pipe were found to be 75 W/m

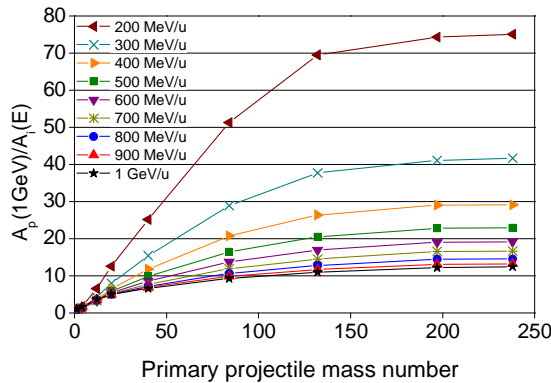


**Fig. 4.** Scaling factor for the beam-loss criteria as a function of primary-projectile mass. The scaling factor is a ratio of the activity induced by a 1 W/m proton beam at 1 GeV,  $A_p(1 \text{ GeV})$ , to the activity induced by 1 W/m beam of interest at a given energy,  $A_i(E)$ . The activities were calculated at zero cooling time [9].

for 200 AMeV, 23 W/m for 500 AMeV, and 12 W/m for 1 AGeV uranium beam (Fig. 4). If the structure is bulky the calculations are analogous, but the criteria are stricter: 60 W/m for 200 AMeV, 12 W/m for 500 AMeV, and 5 W/m for 1 AGeV uranium beam. In reality the beam-loss limits should lie in between these two cases, because a typical beam line is not a uniform structure, it is a mixture of vacuum chamber and bulky elements.

It should be underlined that heavy-ion beam-loss criteria were set for 100 days irradiation time and beam energies from 200 AMeV up to 1 AGeV. However the criteria should be checked for the ion beam energies below 100 AMeV and for long irradiation times. At low energies the stopping range of the heavy ions becomes shorter than the nuclear mean free-path, therefore the number of the produced target fragments would be approximately the same as the number of projectile fragments. In case of long machine operation times, the accumulation of the long-lived projectile fragments becomes an important part in the total activity of the bulky structure. In both cases the nuclide inventory in the target would differ for different projectiles. This fact shows that the heavy-ion beam-loss criteria [9] have limits of applicability and could significantly influence the estimation of cooling times until the hands-on maintenance, and the following radioactive waste disposal.

The tolerable beam-loss criteria for accelerators [9] were established using Monte Carlo (MC) transport codes. MC transport codes are the tools for simulating particle transport and interactions with matter based on Monte Carlo methods [12]. Calculations of neutron transport using this method started in the middle of 1940s [13, 14]; transport of the protons and other hadrons is calculated since the middle of 1960s (see e.g. [15]). The rapid success of accelerator technologies [16] allowed for obtaining diverse experimental data on interaction of hadrons which was used for further development of the theories as well as for verification and improvement of the codes. The codes now give reliable results simulating the interactions of hadrons with matter. Heavy-ion versions of the codes were introduced recently (e.g. SHIELD [17; 18], FLUKA [19; 20] and MARS15 [21 – 25] are able to calculate interactions of heavy ions since 1997, 1999 and 2004, respectively). Since then they are constantly being further improved and verified mostly by comparison with experimentally measured secondary neutron production cross-sections, cross-sections of fission of heavy nuclei with neutrons, activation of thick targets by proton beams [26 – 32]. The activation experiments performed with heavy-ion beams for a verification of the MC codes are: mentioned experiments with stainless steel and copper done at GSI [8; 33 – 35]; the experiment with copper and a 278 AMeV nitrogen beam at PPA (Princeton Particle Accelerator, USA) [32]; the experiments with silver irradiated by a 2.1 AGeV

---

carbon beam, and with copper irradiated by 2083 AMeV carbon, 2 AGeV argon, 211 AMeV and 377 AMeV neon beams at Bevalac, USA [30; 31; 36; 37]; the experiments with copper targets and 135 AMeV carbon at RIKEN – Institute of Physical and Chemical Research in Japan [38]; the irradiations of copper, cobalt and aluminum by 200 AMeV carbon at TWA-ITEP [39]; and finally the experiments performed at HIMAC (Heavy Ion Medical Accelerator in Chiba) with various targets (C, Al, Cr, Fe, Ni, Cu, Pb) irradiated by helium, carbon, neon and argon ions with energies up to 400 AMeV and silicon ions at 800 AMeV [40 – 45].

The verification of the Monte Carlo codes by activation experiments has several advantages in comparison to the verification by measurements of the secondary neutrons. At first, talking about reaction mechanisms, the secondary neutrons are produced in interactions of primary projectiles with target nuclei, when the heavy ions get fragmented. The projectile fragments are found beyond the range of the primary projectiles: heavy- and light-ion projectiles are mostly stopped in the depth of two stopping ranges of the primary beam, whereas secondary neutrons more farther. Therefore if the simulations give accurate results for projectile fragments in the depth of two stopping ranges of the primary ions, they would also give good results in the farther regions. Secondly, as the target is activated by the primary beam as well as by secondary projectiles, the target fragments would be present in the whole target volume. The types and amounts of these residual nuclei could be studied in activation experiments which gives direct information about the radiation hazard during the shutdown [9; 46], whereas secondary neutrons increase the dose rate in the vicinity of the accelerator components only during the operation of the facility. At last, the depth-profiling of the partial residual activities could be done which gives broader overview on the performance of the codes. Summarizing, activation experiments allow for checking transport and nuclear production modules explicitly by comparing the types, amount and depth-distribution of the radionuclides produced or stopped in the irradiated material.

The results of the above listed experiments do not provide sufficient information for a detailed verification of the codes, because most of those studies were focused on finding the reaction cross-sections and not the in-depth distribution of the activity.

## Introduction

---

The depth-profiling was done for light ( $Z = 2 \div 18$ ) ions irradiating different targets at energies below 230 AMeV, for copper targets at 500 AMeV and at 1 AGeV, and for uranium ( $Z = 92$ ) ions irradiating the targets of medium-weight nuclei ( $Z = 26 \div 29$ ) at 500 AMeV and 950 AMeV. For a more complete verification of the MC codes it is necessary to study the activation at different projectile-target combinations and energies. The GSI facility gives a unique opportunity (see e.g. [47]) for obtaining this kind of experimental data because it can accelerate various heavy ions to energies of up to 2 AGeV and gives high intensities up to  $\sim 4 \cdot 10^{10}$  ions/sec at extraction.

The present study is focused on a quantification of the residual activity induced in the material by ion beams of different species: nitrogen ( $Z = 7$ ), argon ( $Z = 18$ ) and uranium ( $Z = 92$ ). The materials chosen for the experiments are aluminum and copper. Aluminum was chosen because it represents a material with relatively low atomic number  $Z$  ( $Z = 13$ ) and copper represents a material with medium  $Z$  ( $Z = 29$ ). In terms of accelerator applications, aluminum components should be preferred in the areas with high beam losses, because this material is expected to get less activated than the higher- $Z$  materials; and copper is a common material for the yokes of the magnets. This study supplements previously performed experiments with copper [6 – 8; 30; 32; 36 – 43; 48] by studying the in-depth distribution of the residual activity at 500 AMeV irradiation. The region of interest for the present work includes the targets with thicknesses corresponding to two stopping ranges of the primary beam. As mentioned above, at such depths heavy-ion fragments of the primary beam still survive, interacting with target nuclei and contributing to the total activity of the target.

Obtained results are important for radiation shielding design; they will also allow for a better verification and further development of the Monte Carlo transport codes which have other applications in accelerator science besides calculation of the beam-loss criteria: they are used for the design of the beam dumps and of radiation shielding. Moreover, the MC codes are widely used in particle physics, nuclear physics, medical applications etc., where the interaction of the beam with the material is of interest.

---

**The goals of the present work** were

- Obtaining new experimental data on interaction of heavy ions with matter;
- Comparison of experimentally obtained data with Monte Carlo simulations using FLUKA, MARS and SHIELD;
- Studying the limits of applicability of the heavy-ion beam-loss criteria;
- Studying the activation and radiation hazards of the materials used in accelerator applications.

The following tasks were fulfilled

- Preparing and performing the experiments on an irradiation of the aluminum and copper targets by argon, nitrogen and uranium beams;
- Simulations of the stopping range of the respective ions in the target and activation of the target;
- Analysis of the experimental data: identification of the nuclides, calculation of their amounts at a certain depth in the targets;
- Comparison of the experimental results with the simulations;
- Simulations of a short- and a long-term irradiations of a bulky target by ion beams.

### **Structure of the thesis**

The thesis consists of the Introduction, four Chapters and Conclusion.

**The Introduction** explains the importance of the activation caused by the beam losses in accelerator facilities. The activation is estimated using Monte Carlo transport codes. The necessity of verification of the codes serves as a motivation for the present study. It is argued that the verification of the codes by activation experiments gives a good overview on the performance of the code.

**Chapter 1** is devoted to the theoretical description of FLUKA, MARS and SHIELD. It briefly mentions the basic idea of the Monte Carlo method and it is mostly focused on transport and nuclide production modules of these codes. This chapter is divided into two sections – one for each module, and further divided into subsections – one for each code. The basics of the theories included in each code are described; the similarities and differences between these codes are pointed out.

**Chapter 2** gives a description of the experimental technique. It has several sections which cover preliminary simulations done for preparing the experimental setup, types of the targets, irradiation conditions, measurements of the residual-activity  $\gamma$ -spectra, analysis of the  $\gamma$ -spectra and uncertainty assessment.

**Chapter 3** shows the results of six held experiments in comparison with the simulations. This chapter is divided into two sections corresponding to the target material, and subsections corresponding to the projectile species. The irradiation conditions and measurement settings are given. The agreements and discrepancies between simulations and experiments are pointed out.

**Chapter 4** is a discussion of the obtained results. This chapter consists of three sections: thin target approach, thick target approach and activation studies for accelerator applications. In the first two sections it is mentioned to what extent the Monte Carlo transport codes FLUKA, MARS and SHIELD give accurate results. The origin of the discrepancies of simulations and experiment are discussed, as well as the practical significance of these activation studies. The limits of applicability of the heavy-ion beam-loss criteria are discussed. The least radiation-hazardous accelerator relevant materials are listed.

**Conclusion** contains the main outcome of the work.

---

---



---

## CHAPTER 1. DESCRIPTION OF THE MONTE CARLO CODES: FLUKA, MARS AND SHIELD.

An interaction of a beam with matter is simulated in FLUKA, MARS and SHIELD using Monte Carlo methods. This computational method exploits sets of random numbers at each step of calculations: starting with a position where the projectile enters the target, then randomly choosing a path length of the particle until the interaction point, after this choosing the type of interaction (elastic or inelastic) and finally choosing the direction of the scattered particle in case of elastic interaction or parameters of the secondary projectiles in case of inelastic interaction [12]. After the interaction happened the same algorithm is repeated.

Modern versions of FLUKA, MARS and SHIELD simulate the interaction of the particles with matter using an exclusive approach. In such an approach all the possible channels of the reaction are treated and all the conservation laws typical for an occurring interaction are hold for all the individual reaction products [4]. Mentioned codes have well-developed modules for building geometry and chemical composition of the target [17 – 25].

Present work is devoted to the verification of the transport and nuclide production modules for energies of the primary projectiles up to 1 AGeV, therefore the following theoretical description is focused on this energy range. Other options needed for calculating the physical processes, such as electron-photon showers, meson decays, transport of the low energy neutrons etc., are less important for the present study and therefore are not discussed here.

The transport module calculates the stopping power of the material and therefore determines the stopping range of the projectile in matter (position of the Bragg peak). The nuclide production module calculates the total  $\sigma_{\text{tot}}$  and inelastic  $\sigma_{\text{in}}$  interaction cross-sections of the hadrons and nuclear fragments with nuclei of the target; the multiplicity, types, energy and angular distributions of the nuclear reaction products. The accuracy of the nuclear models used for simulating the inelastic nuclear

interactions in the target defines the quality of the nuclear production module and the quality of the transport code itself.

It should be noted that FLUKA, MARS and SHIELD codes calculate transport and interactions of incident particles with matter using a default set of implemented theories which can not be changed by the user. However some of the options could be altered. Such possibilities are discussed in this Chapter.

### 1.1 Transport module

A swift particle travelling through matter undergoes Coulomb scattering by atomic electrons and nuclei. The resulting energy losses of the projectile are described by electronic and nuclear stopping power. In addition to Coulomb scattering and energy losses, the ionization fluctuations could also be taken into account.

FLUKA, MARS and SHIELD have different ways of calculating the transport of the charged particles; therefore the following description is divided into three subsections – one for each code.

#### 1.1.1. FLUKA

The multiple Coulomb scattering is described in FLUKA using the original approach [49]. The model has two parts: a path length correction (PLC) algorithm and the correlation algorithm for the various angles involved in simulations. The first one accounts for the variance of PLC as well as its average value, the latter one chooses the position angles in such a way as to obtain the correct average value and correct distribution for the polar angle of the particle position vector with a proper correlation between the projected position and direction angles. This approach is still based on the Molière theory [49], but has several improvements: it is step length insensitive, it could account for correlations of scattering angles, for spin-relativistic corrections to the Rutherford cross-section, and for the effects of nuclear form factors.

The transport of charged particles in FLUKA [50] could be simulated in several ways. A first option is the continuous slowing down approximation (CSDA). In the CSDA it is assumed that the particle continuously loses its energy  $E$  along the length

of the trajectory. The range calculated in CSDA  $R_{CSDA}$  is a very close approximation to the path length  $x$  of the particle. It is given by the formula

$$R_{CSDA} = \int_0^{E_0} \left( \frac{dE}{dx} \right)^{-1} dE, \quad (1)$$

where  $E_0$  is the kinetic energy of the particle at the surface of the material. Ionization fluctuations as well as production of delta rays (knock-on atomic electrons with sufficient energy to ionize further atoms) are neglected in this case. A second option is taking into account ionization fluctuations, but no delta rays. A third option allows for calculating the production of delta rays above a chosen energy threshold and no ionization fluctuations below the threshold. A last option treats both delta rays above threshold and ionization fluctuations below.

Energy losses per unit path length resulting from interactions of the projectile with electrons are calculated using the Bethe-Bloch theory [51 – 55] and various corrections:

$$dE / dx = \frac{2\pi n_e r_e^2 m_e c^2 Z^2}{\beta^2} \left[ \ln \left( \frac{2m_e c^2 \beta^2 T_{max}}{I^2 (1 - \beta^2)} \right) - 2\beta^2 - \delta - 2\frac{C}{Z} + 2ZL_1(\beta) + 2ZL_2(\beta) + G \right], \quad (2)$$

where  $n_e$  is the electron density in the material,  $r_e$  – the classical electron radius,  $m_e c^2$  – the mass of the electron,  $Z$  – the charge of a projectile,  $\beta = v/c$  ( $v$  is the velocity of the projectile),  $I$  is the mean excitation energy in the material,  $T_{max}$  – the maximum energy transfer to an electron,  $\delta$  – the density correction of Fermi [56],  $C$  – the shell correction which arises due to orbital velocities of the target electrons,  $L_1$  – the Barkas correction ( $\sim Z^3$ ) which is responsible for difference in stopping power for particles and antiparticles [57],[58],  $L_2$  – the Bloch ( $\sim Z^4$ ) correction is important for high-velocity particles and minimal impact parameters [54],  $G$  – the Mott correction accounts for deviations from Rutherford cross-section at relativistic velocities which gives rise to contributions from small impact parameters [59 – 60].

The fraction of nuclear stopping in the total energy loss is negligible at high energies; however, the nuclear stopping power is important for low-energy heavy particles. The decrease of projectile's energy in interactions with atomic nuclei is described by the following formula [61]:

$$\frac{1}{\rho} S_n(T) = \frac{5105.3 Z_1 Z_2 \hat{S}_n(\varepsilon)}{(Z_1^{0.23} + Z_2^{0.23}) \left(1 + \frac{M_2}{M_1}\right) A}, \quad (3)$$

$$\text{if } \varepsilon < 30, \hat{S}_n(\varepsilon) = \frac{0.5 \ln(1 + 1.1383 \varepsilon)}{\varepsilon + 0.01321 \varepsilon^{0.21226} + 0.19593 \sqrt{\varepsilon}},$$

$$\text{if } \varepsilon \geq 30, \hat{S}_n(\varepsilon) = \frac{\ln(\varepsilon)}{2\varepsilon},$$

$$\text{where } \varepsilon = \frac{32.536 T}{(Z_1^{0.23} + Z_2^{0.23}) \left(1 + \frac{M_1}{M_2}\right) Z_1 Z_2}.$$

Higher order corrections (Barkas, Bloch and Mott), and calculations of the nuclear stopping power were included in the latest release of the code – FLUKA2011, issued in April 2011. There is a possibility to switch off the calculation of nuclear stopping, Barkas and Bloch terms; the other corrections are always taken into account. Figure 5 shows the energy deposition function of 500 AMeV uranium  $^{238}\text{U}$  in aluminum target. The calculations were done with different combinations of possible corrections in order to show how they change the energy deposition curve.

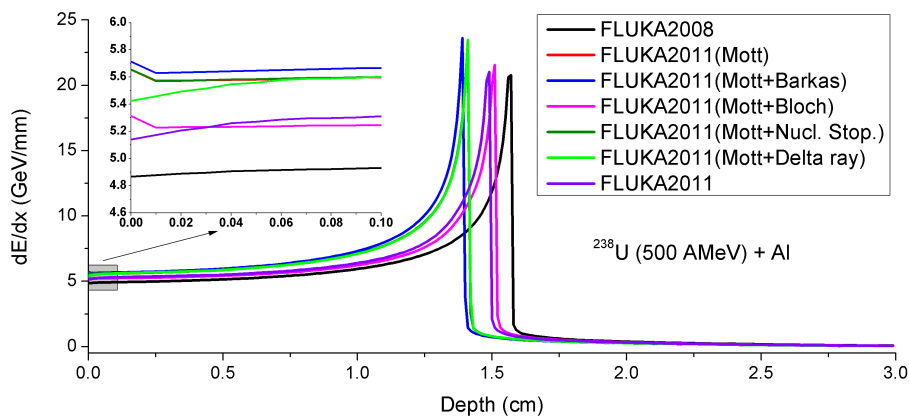


**Fig. 5. Energy deposition function of 500 AMeV uranium  $^{238}\text{U}$  in aluminum. Simulations using FLUKA 2008 (no Mott, no Barkas, no Bloch corrections, no nuclear stopping, no delta ray), FLUKA 2011 (Mott), FLUKA 2011 (Mott + Barkas), FLUKA 2011 (Mott + Bloch), FLUKA 2011 (Mott+Nuclear Stopping), FLUKA 2011 (Mott + Delta ray), FLUKA 2011 (Mott, Barkas, Bloch corrections, nuclear stopping, delta ray production). FLUKA 2011 (Mott+Nuclear Stopping) coincide with FLUKA 2011 (Mott) within 1 %. FLUKA 2011 (Mott + Delta ray) coincides in the range area with FLUKA 2011 (Mott + Nuclear Stopping) and FLUKA 2011 (Mott) within 4 %.**

The fluctuations of energy losses are calculated using original FLUKA algorithm [62], which is based on general statistical properties of the cumulants of a Poisson distribution. The expression for the  $m_{th}$  cumulant of the energy loss distribution  $k_m^{\Delta E}$  is the following:

$$k_m^{\Delta E} = \sum_{i=1}^{N_d} \langle n_i \rangle E_i^m + \langle n_{\delta}^{T_{min}} \rangle \langle T_{\delta}^m \rangle, \quad (4)$$

$$\langle n_i \rangle = n_e \sigma_i t \equiv \sum_i t, \quad (5)$$

$$\langle n_{\delta}^{T_{min}} \rangle = n_e t \int_{\eta}^{T_{min}} dT_e \frac{d\sigma_{\delta}}{dT_e}, \quad (6)$$

$$\langle T_{\delta}^m \rangle = n_e t \int_{\eta}^{T_{min}} dT_e T_e^m \frac{d\sigma_{\delta}}{dT_e}, \quad (7)$$

$$n_e = \sum_{j=1}^L \frac{Z_j \rho_j N_A}{A_j}, \quad (8)$$

where  $N_d$  – the number of discrete levels,  $E_i$  – the excitation and ionization energy,  $\sigma_i$  – the microscopic cross-sections,  $t$  is a step size,  $T_{min}$  is the threshold for explicit  $\delta$ -ray production,  $d\sigma_{\delta}/dT_e$  – the cross-section for  $\delta$ -ray production,  $n_e$  – the number of electrons per unit volume,  $N_A$  – the Avogadro number,  $L$  – the number of elements of the mixture or compound under consideration,  $Z_j$  – the atomic numbers,  $A_j$  – the atomic weights,  $\rho_j$  – the partial densities of the elements in the mixture. Using this algorithm, the first six moments of the energy loss distribution could be reproduced.

### 1.1.2. SHIELD

The multiple Coulomb scattering is calculated in SHIELD according to Molière theory. The Molière theory [49, 63] is based on small angle approximations of the total deviation from the initial direction of movement. According to this theory, the scattering is described by a single parameter – the screening angle  $\chi'_{\alpha}$ :

$$\chi'_{\alpha} = \tilde{\lambda} \sqrt{1.167(1.13 + 3.76\alpha^2)} / (0.885a_0 Z^{-1/3}), \quad (9)$$

$$\alpha = zZe^2 / \hbar v, \quad (10)$$

## Chapter 1. Description of the MC transport codes

---

here  $\lambda$  is the de Broglie wavelength of the electron,  $a_0$  is the Bohr radius,  $z$  and  $v$  are the scattered particle's charge and velocity,  $Z$  is the charge of the target,  $\hbar$  is the Dirac constant,  $e$  is the elementary charge.

The angular distribution depends only on the ratio of  $\chi_c$  to the screening angle  $\chi'_\alpha$  [63].  $\chi_c^2$  is given as

$$\chi_c^2 = 4\pi N t e^4 Z(Z+1) z^2 / (p v)^2, \quad (11)$$

here  $N$  is the number of scattering atoms per  $\text{cm}^3$ ,  $t$  is the thickness of the region,  $p$  is the momentum of the scattered particle. The total probability of single scattering through an angle greater than  $\chi_c$  is unity.

The angular distribution function is given in the following way

$$f(\theta)\theta d\theta = \vartheta d\vartheta [f^{(0)}(\vartheta) + B^{-1}f^{(1)}(\vartheta) + B^{-2}f^{(2)}(\vartheta) + \dots], \quad (12)$$

$$f^{(n)}(\vartheta) = n!^{-1} \int_0^\infty u du J_0(\vartheta u) \cdot \exp\left(-\frac{1}{4}u^2\right) \left[\frac{1}{4}u^2 \ln\left(\frac{1}{4}u^2\right)\right]^n, \quad (13)$$

where  $\theta$  is the scattering angle (small enough so that  $\text{Sin } \theta \approx \theta$ ),  $f(\theta)$  is the number of electrons in the angular interval  $d\theta$ , parameter  $B$  is defined using equation

$$B - \ln B = b, \quad (14)$$

$$\text{where } b = \ln\left(\frac{\chi_c}{\chi'_\alpha}\right)^2;$$

the variable  $\vartheta$  is defined by

$$\vartheta = \theta / (\chi_c B^{1/2}), \quad (15)$$

$J_0(\vartheta u)$  is the Bessel function.

The Molière theory is only valid when the number of scattering events is high enough ( $> 20$ ) and when the average deflection is less than one radian.

Energy losses could be calculated in SHIELD using one of the two options. One of them is, as well as in FLUKA, the CSDA and calculating the stopping power using Bethe-Bloch theory with corrections for charge changing processes at low energies and density effects at ultra-relativistic energies. The other option is to use the ATIMA code [64] which is included in SHIELD.

Energy straggling is modeled according to the theory of Vavilov [65] or, again, using the ATIMA code.

The SHIELD-simulations presented in this work were done using the ATIMA stopping module, therefore only the respective theoretical description would be given in this subsection.

At energies above 30 AMeV ATIMA calculates the stopping power following the Lindhard and Sørensen theory [66] which explicitly calculates the energy transfer in the collisions with target electrons.

The electronic stopping power could be written as

$$-\frac{dE}{dx} = \frac{4\pi Z_1^2 e^4}{mv^2} NZ_2 L, \quad (16)$$

where  $Z_1 e$  is the charge of the projectile nucleus,  $Z_2$  is the charge number of the target nucleus,  $NZ_2$  is the average density of electrons,  $m$  is the electron mass and  $L$  is given as

$$L = \Delta L + L_{stand} + \delta L_{shell} + \delta L_{Barkas} + \delta L_{scr}, \quad (17)$$

with  $\delta L_{shell}$  being the shell correction,  $\delta L_{Barkas}$  being the Barkas correction,  $\delta L_{scr}$  – the correction for screening of the ion potential. The standard function  $L_{stand}$  is the quantum mechanical perturbation formula

$$L_{stand} = \ln\left(\frac{2mv^2}{I} \gamma^2\right) - \frac{v^2}{c^2} - \frac{1}{2} \delta, \quad (18)$$

$I$  is the mean excitation energy,  $(-\delta/2)$  is the density correction,  $\gamma = (1 - v^2/c^2)^{-1/2}$ . It should be mentioned that  $L_{stand}$  does not present the full term belonging to first-order quantum perturbation theory; the full term also accounts for shell correction. This correction was omitted in  $L_{stand}$  for simplicity. The Mott correction presenting the higher order term of scattering theory was also omitted.

$\Delta L$  differs for relativistic and nonrelativistic cases. In nonrelativistic theory it represents Bloch's correction to the Bethe [67] formula:

$$\Delta L = \sum_{l=0} \left[ \frac{l+1}{(l+1)^2 + \kappa^2/4} - \frac{1}{l+1} \right], \quad (19)$$

$$\kappa = \frac{2Z_1 e^2}{\hbar v}, \quad (20)$$

where  $l$  is the angular momentum. This expression for  $\Delta L$  is not applicable for  $\kappa \gg 1$ , because in this case the ions will carry electrons which will change the stopping for heavy ions due to screening by electrons bound to the ion.

In relativistic case  $L$  depends weakly on target and projectile parameters:

$$L \rightarrow \ln(2c / R\omega_{pl}) - 0.2 = \ln(1.64c / R\omega_{pl}), \quad (21)$$

here  $\omega_{pl} = \sqrt{4\pi n e^2 / m}$  is the plasma frequency corresponding to the average density  $NZ_2$  of target electrons, and  $R$  is the nuclear radius.

The average square fluctuation in energy loss  $\Omega^2$  is given by  $\Omega^2 = \langle (\delta E - \langle \delta E \rangle)^2 \rangle$ , where  $\delta E$  is the energy loss. The increase of the average square fluctuation is formulated as

$$\frac{d\Omega^2}{dx} = 4\pi Z_1^2 e^4 NZ_2 \gamma^2 X, \quad (22)$$

$$X = 1 - \frac{v^2}{2c^2}. \quad (23)$$

Average square fluctuation of the energy loss depends on the thickness of the target. The parameter which distinguishes the type of the target is

$$\xi = \frac{2\pi Z_1^2 e^4 Z^2 N x}{mv^2 T_0 X}, \quad (24)$$

$T_0 X = 2mv^2 \gamma^2 X$  is the effective maximum energy transfer.

In case of a thick target ( $\xi \geq 10$ ) the distribution would be Gaussian. In case of a thin target ( $\xi < 5$ ) the distribution would be Landau-type with a smaller peak width and long tail towards large energy losses. In the intermediate region the interpolation between the two cases is done.

At energies below 10 AMeV ATIMA uses an older version of Ziegler's SRIM code [68]. Ionization fluctuations are described using the theory of Firsov [69] and Hvelplund [70].

In the energy region between 10 AMeV and 30 AMeV the stopping range is calculated by extrapolation.



### 1.1.3. MARS

A modified Molière theory is used for simulating multiple Coulomb scattering in MARS. The Molière theory itself is described in the previous subsection, the modifications were done in order to take into account the difference between scattering of atomic nuclei and electrons [71].

Energy losses of heavy ions are treated in MARS as a product of proton energy loss and effective charge of the ion  $Z_{\text{eff}}$  [72 – 75]. This approach is based on the experimental evidence of the correlation between the proton and heavy ion stopping power [73 – 75]. However the validity of the approach for very heavy ions is not yet proved.

The effective charge is described in different ways in different energy regions:

(1) Below 1 AMeV the theory of Ziegler is used [76];

(2) Above 3 AMeV and below 100 AMeV the modified formalism of Pierce and Blann [73] is used. In the original expression for the effective charge by Pierce and Blann [73], the dependence on target material is not taken into account:

$$\frac{Z_{\text{eff}}}{Z_1} = 1 - \exp(-0.95v_r), \quad (25)$$

where the reduced velocity  $v_r = v/(Z_1^{2/3} e^2 / \hbar)$ ,  $v$  and  $Z_1$  are the projectile velocity and atomic number. In the modified version the dependence of the  $Z_{\text{eff}}$  on the target material is added

$$\frac{Z_{\text{eff}}}{Z_1} = 1 - \exp(-0.95v_r f_c), \quad (26)$$

$f_c$  is the correction function which was found by fitting the experimental data for different ions and materials using the above mentioned expression. This function shows the reduction of the effective charge with target atomic number [74].

(3) In energy region between 1 AMeV and 3 AMeV the interpolation between (1) and (2) is done;

(4) At energies above 100 AMeV instead of the effective charge, the ion charge state distribution is used [77].

After defining the  $Z_{\text{eff}}$ , the stopping power is calculated in the following way [72]:

(a) At energies below 10 AMeV the proton stopping power from [76 – 78] is used and  $Z_{\text{eff}}$  is applied as multiplicative factor,

(b) In the energy region  $30 \text{ AMeV} < E < 80 \text{ AMeV}$  weighted average between proton stopping power calculated using Bethe-Bloch theory with shell, Barkas, and Lindhard-Sørensen corrections for proton and the same proton stopping power but with the correction for the ion using effective charge is used,

(c) At energies between 10 and 30 AMeV, an interpolation between (a) and (b) is performed,

(d) At energies above 80 AMeV, proton stopping power is calculated according to the Bethe-Bloch theory with above mentioned corrections calculated for the ion using effective charge.

Mentioned in (c) and (d) Bethe-Bloch theory with shell, Barkas and Lindhard-Sørensen corrections is basically ATIMA-approach (for energies  $> 30 \text{ AMeV}$ ) described in subsection “SHIELD”, however without correction for screening of the ion potential, because it is calculated for incident proton. It should be stressed that MARS does all the calculations for protons and then uses the ion effective charge as a multiplicative factor for finding the stopping of the heavy ions.

Fluctuations are calculated using the theory of Vavilov [65]. The straggling distribution in Vavilov theory is given as

$$f(\varepsilon, \delta s) = \frac{1}{\xi} \phi_v(\lambda_v, \kappa, \beta^2). \quad (27)$$

where  $\phi_v(\lambda_v, \kappa, \beta^2) = \frac{1}{2\pi i} \int_{c-i\infty}^{c+i\infty} \phi(s) \exp(\lambda s) ds$ ,  $c \geq 0$ ,

$$\phi(s) = \exp[\kappa(1 + \beta^2 \gamma)] \exp[\psi(s)],$$

$$\psi(s) = s \ln \kappa + (s + \beta^2 \kappa) [\ln(s/\kappa) + E_1(s/\kappa)] - \kappa \exp(-s/\kappa),$$

$$E_1(z) = \int_{\infty}^z t^{-1} e^{-t} dt,$$

$$\lambda_v = \kappa \left[ \frac{\varepsilon - \bar{\varepsilon}}{\xi} - \gamma' - \beta^2 \right]$$

$\gamma' \approx 0.422874$ ,  $\bar{\varepsilon}$  – the average energy loss,  $\varepsilon$  – the actual energy loss.

Vavilov theory takes into account the limit on the maximum energy transfer in a single collision:

$$E_{\max} = \frac{2m_e\beta^2\gamma^2}{1 + 2\gamma m_e/m_x + (m_e/m_x)^2}. \quad (28)$$

The parameter  $\kappa$  is a ratio of mean energy loss  $\xi$  to the maximum energy transfer  $E_{\max}$ :

$$\kappa = \frac{\xi}{E_{\max}}, \quad (29)$$

$\xi = \frac{2\pi z^2 e^4 N_{Av} Z \rho dx}{m_e \beta^2 c^2 A} = 153.4 \frac{z^2 Z}{\beta^2 A} \rho dx$ , where  $\rho$  is the density and  $\delta x$  is the thickness of the material.

### 1.2. Nuclide production module

A nuclear reaction could occur at an interaction point at the end of the path length of each projectile. The possibility of such an interaction is calculated taking into account the nuclear mean free path. The energy of the particle is known at this moment. The type of the interaction is chosen by comparing  $\sigma_{\text{tot}}$  and the inelastic cross-section  $\sigma_{\text{in}}$ . As an output the nuclear production module gives a number of nuclides of certain species after an interaction occurs. The following subsections are devoted to the description of the respective nuclear models used in FLUKA, SHIELD and MARS.

It should be added, that FLUKA is able to take into account irradiation time and to calculate radioactive decay-chains. SHIELD and MARS do not have included modules for this kind of calculations; separate programs like DCHAIN [79] or DeTra [80] should be used.

#### 1.2.1. FLUKA

FLUKA executes two different theories for describing nuclear-nuclear (AA) interactions in the energy region of interest. For the energies of the primary beam up to 100 AMeV the interactions are calculated using the Boltzmann Master Equation

(BME) theory [81 – 96]. For the energies from 100 AMeV up to 5 AGeV the Relativistic Quantum Molecular Dynamics (RQMD) [97 – 99] is used. Equilibrium de-excitation of the residual nuclei includes Fermi-breakup of the light nuclei ( $A < 17$ ), evaporation and fragmentation of the heavy nuclei.

The BME theory was introduced in FLUKA2011; earlier versions of FLUKA did not calculate the interactions of heavy ions ( $A > 1$ ) below this energy, but just transported them. The BME theory describes the interaction of the projectile and target nuclei, seen as two-component Fermi gases [83]. In this case the state of the nucleus is explicitly defined by the occupation numbers of single-particle nucleon states; therefore by calculating the time evolution of the occupation numbers it's possible to find the multiplicities of the emitted particles and their energies as well as the state of the residual nucleus. The BME theory was developed with the assumption that nuclear reaction has two steps. In the first, fast one, projectile and target nucleons interact pairwise which leads to the development of the intranuclear cascade in the target and possible emission of the nucleons [82]. However the majority of the particles (nucleons, gammas and clusters) are emitted during the second, slow step, when the excited residual nucleus deexcites. The dependence of the occupation numbers  $n_i$  on time, for the residual nucleus, is given by a set of master equations:

$$\begin{aligned} \frac{d(n_i g_i)^P}{dt} = & \sum_{jlm} [\omega_{lm \rightarrow ij}^{PP} g_l^P n_l^P g_m^P n_m^P (1 - n_i^P)(1 - n_j^P) - \omega_{ij \rightarrow lm}^{PP} g_i^P n_i^P g_j^P n_j^P (1 - n_l^P)(1 - n_m^P)] + \\ & + \sum_{jlm} [\omega_{lm \rightarrow ij}^{PN} g_l^P n_l^P g_m^N n_m^N (1 - n_i^P)(1 - n_j^N) - \omega_{ij \rightarrow lm}^{PN} g_i^P n_i^P g_j^N n_j^N (1 - n_l^P)(1 - n_m^N)] - \\ & - n_i^P g_i^P \omega_{i \rightarrow i}^P g_i^P \delta(\varepsilon_i^P - \varepsilon_F^P - B_i^P - \varepsilon_i^P) - \frac{dD_i^P}{dt}, \end{aligned} \quad (30)$$

where  $n$  is an occupation probability,  $0 \leq n \leq 1$ ,  $g$  is the total number of states in the bin,  $\varepsilon$  is the energy of the nucleon state. Superscripts P and N stand for protons and neutrons respectively, while the subscripts  $i, j, l, m$  refer to angles and energies of the particles. The number of protons emitted into the continuum from the bin  $i$ , as well as their energy in the time interval  $dt$  are given by

$$\frac{dn_i}{d\varepsilon_i} = n_i^P g_i^P \omega_{i \rightarrow i}^P g_i^P \delta(\varepsilon_i^P - \varepsilon_F^P - B_i^P - \varepsilon_i^P) dt \quad (31)$$

The quantities  $\omega_{lm \rightarrow ij}$  and  $\omega_{i \rightarrow i'}$  are internal transition decay rate and the decay rates for emission of single protons into the continuum [83]. The elementary nucleon-nucleon scattering cross-sections were taken from [100].

$\frac{dD_i^p}{dt}$  accounts for the emission of protons bound in clusters.

The solution of these equations gives, as a function of time, the occupation number  $n_i$ . The multiplicity spectrum of the emitted particles (from bin  $i$  to the continuum, in the time interval  $dt$ ) is described by

$$\frac{dn_i^c}{d\epsilon_{i'}} = n_i^p g_i^p \omega_{i \rightarrow i'}^p g_{i'}^p \delta(\epsilon_{i'}^p - \epsilon_F^p - B_i^p - \epsilon_{i'}^p) dt. \quad (32)$$

The decay rates for emission particles are given by

$$\omega_{i \rightarrow i'}^p = \frac{\sigma_{inv} v_{i'}}{g_i \Omega}, \quad (33)$$

where  $\sigma_{inv}$  is the inverse process cross-section,  $v_{i'}$  relative velocity between the emitted nucleon and residual nucleus,  $\Omega$  – laboratory volume. This expression is valid for protons, neutrons and clusters.

For the energies from 100 A MeV to 5 A GeV the nuclear reactions are simulated using the modified RQMD model (RQMD-2.4) [97 – 99]. In this microscopic model, as well as in BME theory, both projectile and target nuclei are treated in Fermi gas approximation with the experimental binding energies. This allows fixing the issues of energy-momentum conservation. The model is Lorentz invariant; it combines the classical propagation of hadrons with the stochastic scattering and Pauli blocking in collisions. The model explicitly follows the trajectories of the hadrons and takes into account the growth of the inelastic nuclear reactions with energy [99].

Both BME theory and RQMD are default options in FLUKA.

Another feature important for the present study that should be “switched on” separately is Electromagnetic Dissociation (EMD) [101]. FLUKA could take it into account in case of peripheral nuclear collisions. The lowest order diagram of the inelastic interaction of two ions  $A_1$  and  $A_2$  is shown in Fig. 6. The cross-section of this process  $\sigma_{EM}$  increases with energy and charge number  $Z$  of the target:

$$\sigma_{EM} = \int \frac{d\omega}{\omega} n_{A_1}(\omega) \sigma_{\gamma A_2}(\omega), \quad (34)$$

$$n_{A_1}(\omega) \propto Z_{A_1}^2$$

here  $\omega$  is the energy of a quasireal photon,  $n_{A_1}$  is the photon flux density,  $Z_{A_1}$  is the charge number of the target,  $\sigma_{\gamma A_2}$  is the cross-section of the  $\gamma A_2$  interaction (these cross-sections are taken from the experiments).

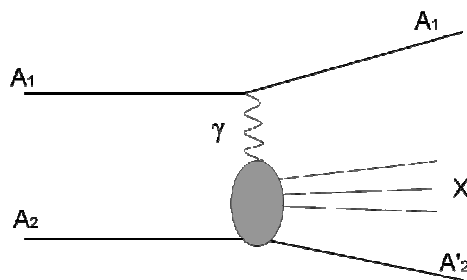


Fig. 6. One-photon process induced by peripheral collision of two ions [101].

### 1.2.2. SHIELD

The nuclide production module of SHIELD is based on the Multi Stage Dynamical Model (MSDM) [102 – 103]. The principal scheme of this generator is shown in Fig. 7.

It is assumed that the interaction process goes through the following stages: (1) fast stage which consists of cascade, coalescence and pre-equilibrium emission stages; (2) deexcitation stage which is realized through Fermi break up, evaporation of fission mechanisms.

In the fast cascade stage of the reaction the projectile-target interaction is treated as a series of binary collisions of nuclear constituents and/or produced hadrons. In the energy region of interest ( $E < 1$  AGeV) the considerations could be limited to nucleons, pions and  $\Delta$ -resonances whose interactions are described using Dubna Cascade Model (DCM) [104] extended to include pion dynamics for production and absorption processes [105]. DCM is based on the numerical solution of the system of Boltzmann-Uehling-Uhlenbeck relativistic kinetic equations.

$$p^\mu \partial_\mu f_i(x, p) = \sum_j C_{coll}(f_i, f_j) + \sum_k R_{k \rightarrow i}(f_k), \quad (35)$$

where  $f_i(x, p)$  is a one-particle distribution function for the hadrons of type  $i$ . The term  $\sum_j C_{coll}(f_i, f_j)$  accounts for two-body collisions, the other term  $\sum_k R_{k \rightarrow i}(f_k)$  describes the resonances decaying into particles of type  $i$  with 4-momentum  $p$  and 4-coordinate  $x$ .

The binding energy of the nucleus and Pauli principle are taken into account [104]. Total  $\sigma_{tot}$  and inelastic  $\sigma_{in}$  cross-sections of nucleon-nuclear, pion-nuclear and nuclear-nuclear interactions are calculated using the parameterization proposed by Barashenkov [106 – 109] and included in the code CROSEC [109] integrated in SHIELD. The cross-sections are found by fitting the existing experimental data on above-mentioned interactions. Kaon-nuclear and antinucleon-nuclear cross-sections are taken from Ref. [110].

During the coalescence stage the nucleons which are close to each other in the momentum space could form complex light particles due to the final state interaction [104].

The pre-equilibrium decay stage describes the thermalization of the nucleus formed in the cascade stage, i.e. the initial state of the excited nucleus is given by the calculations resulting from the cascade stage [104; 111]. The evolution towards equilibrium is treated by the Cascade-Exciton Model (CEM) [111; 112]. It takes into account all possible nuclear transitions and emission of the following particles – n, p, d, t,  $^3\text{He}$ , and  $^4\text{He}$  – which accompanies the thermalization process. The anisotropy of the angular distributions for the pre-equilibrium particles is taken into account.

The de-excitation stage deals with slow disintegration of the nuclei. The process could go different competing ways: through Fermi decay, evaporation of the fragments or nuclear fission. The path of the de-excitation depends on the input parameters. In case of light excited nuclei ( $A^* \leq 16$ ) the de-excitation goes is an explosive way, breaking the nuclei into several small clusters which described by Fermi model [113]. All final fragments are assumed to be in ground or low-excited states. If the excited nucleus is heavy ( $A^* > 16$ ) and the excitation energy is small

## Chapter 1. Description of the MC transport codes

( $U^* < 2$  A MeV), such a nucleus undergoes either successive particle evaporation or fission which is calculated using the evaporation-fission model [114 – 116]. Using this approach it is possible to account for heavy ejectiles up to  $^{18}\text{O}$  as well as for light particles (nucleons, d, t,  $\alpha$ ) in ground and particle-stable states [114].

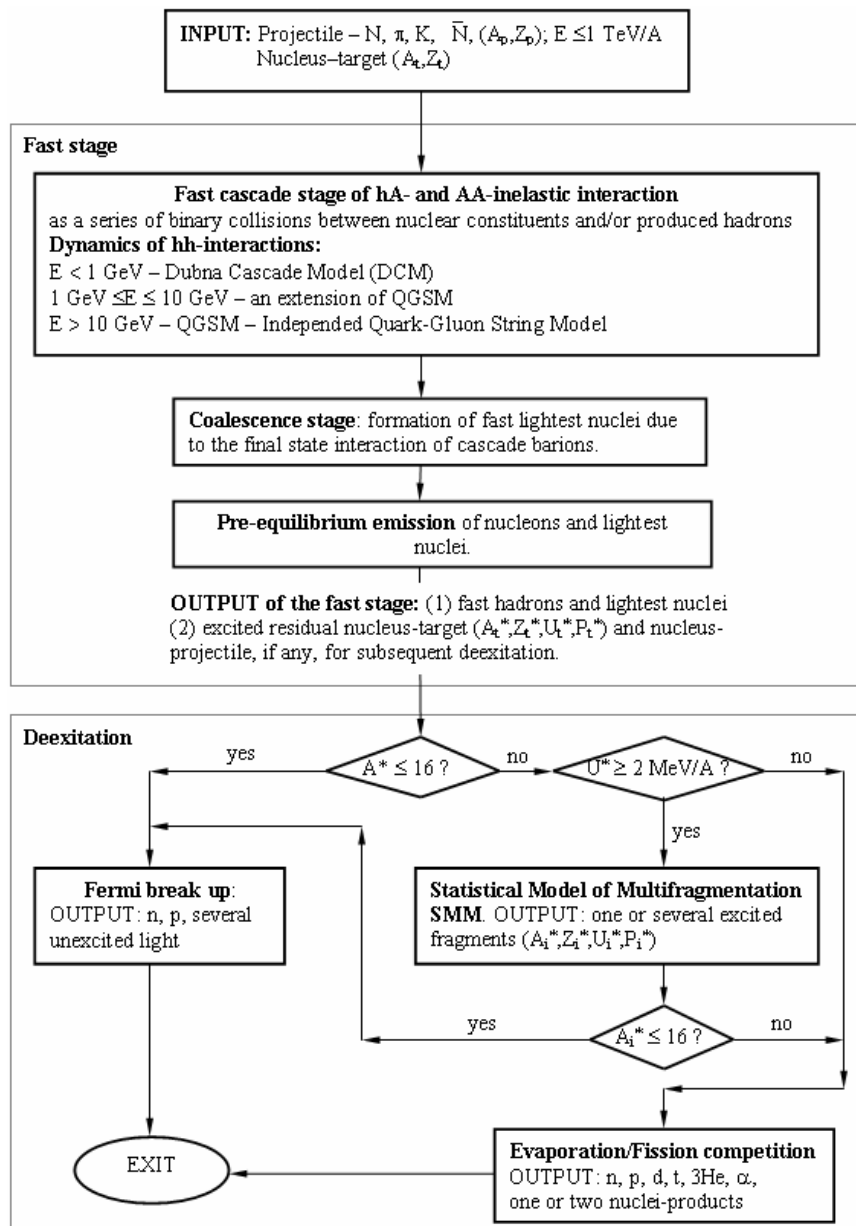


Fig. 7. Scheme of the Multi Stage Dynamical Model generator of nuclear reactions [102 – 103].



This model is an extension of the Weisskopf evaporation scheme. At high excitation energy the main de-excitation mechanism is a multifragmentation, which is calculated according to the statistical model of multifragmentation [114; 116; 117]. After the break-up of the nucleus, the secondary projectiles propagate independently and undergo further interactions and decays. The de-excitation of large and small fragments is described by evaporation-fission and Fermi models, respectively.

### 1.2.3. MARS

Nuclear interactions in MARS in the energy range from 10 AMeV up to 800 AGeV [118] are calculated in the Los Alamos Quark-Gluon String Model (LAQGSM) [119], which only slightly differs from the Multi Stage Dynamical Model (MSDM) included in SHIELD.

As well as MSDM in the energy range of interest, LAQGSM includes the Dubna Cascade Model for nuclear interactions (see previous subsection). However the version of DCM included in LAQGSM has several differences from the above mentioned one.

- It takes into account interactions of two cascade particles with each other.
- This model uses continuous nuclear density distribution therefore there is no need to account for border effects and refraction/reflection of the cascade particles.
- The calculations of inelastic cross-sections for heavy-ion nuclear interactions and also elastic cross-sections needed for full particle transport [118] are based on the JINR model [120]. Photonuclear interaction cross-sections are described in great details for all nuclei and energies from a few MeV up to 40 TeV using approximations from [121].
- It keeps track of the time of intranuclear collisions  $\tau_f$  and of the depletion of the nuclear density during the development of the cascade [119].

For spectator nucleons of the target the system of equations is the following:

$$p^\mu \partial_\mu f_S(x, p) = -f_T(x, p) \left[ \sum_{j=R,S,P} \int d\omega_j f_j(x, p_j) Q_{Tj} \sigma^{Tj} \right]. \quad (36)$$

For spectator nucleons of the projectile the replacement  $P \rightarrow T$  and  $T \rightarrow P$  is done.

Stable hadron participants are described by

$$\begin{aligned}
 p^\mu \partial_\mu f_S(x, p) = & -f_T(x, p) \left[ \sum_{j=T, P, R, S'} \int d\omega_j f_j(x, p_j) Q_{Sj} \sigma^{Sj} \right] + \int d\omega_p d\omega_T \Phi(p_p, p_T | x, p, \tau_f) + \\
 & + \sum_{j=T, P} \sum_{k=R, S'} \int d\omega_j d\omega_k \Phi(p_j, p_k | x, p, \tau_f) + \sum_{j=T, P} \sum_{k=R, S'} \int d\omega_j d\omega_k \Phi(p_j, p_k | x, p, \tau_f) + \\
 & + \sum_{j=R', S'} \sum_{k=R, S'} \int d\omega_j d\omega_k \Phi(p_j, p_k | x, p, \tau_f) + \\
 & + \sum_R \int d\omega_{S'} d\omega_R f_R(x, p_R) \Gamma^{R \rightarrow S+S'} \delta^{(4)}(p_R - p_{S'} - p). \quad (37)
 \end{aligned}$$

The quantity  $Q_{ij} = \sqrt{(p_i p_j)^2 - p_i^2 p_j^2}$  is related to the relative velocity of the colliding hadrons  $v_{rel} = Q_{ij} / E_i E_j$  and  $d\omega = d^3 p / E$  is the invariant volume element in momentum space. The rate of hadron formation is expressed as

$$\Phi(p_i, p_j | x, p, \tau_f) = \int dx' f_i(x', p_i) f_j(x', p_j) Q_{ij} \sigma^{ij} \phi(x' | x, p, \tau_f), \quad (38)$$

where  $\phi(x' | x, p, \tau_f)$  is the transition probability of detecting a hadron at point  $x$  if the collision took place at the space-time point  $x'$ .

The cascade particles could be absorbed by or escape from the target or projectile. The coalescence could also happen, which is described using the same theory [104] as in MSDM of SHIELD. After this the pre-equilibrium stage starts. In contrast to MSDM, LAQGSM calculates the pre-equilibrium emission, using Cascade-Exciton Model [111] as realized in the CEM03 code [122]. The preequilibrium emission is less in the CEM03 code than in the original CEM (only transitions that increase the number of excitons are allowed). It also reduces masses of particles in the calculation, taking into account recoils.

The following de-excitation phase is calculated using either mentioned Fermi break-up model when the mass number of residual nucleus is  $A \leq 12$ , or it is calculated using Furihata's Generalized Evaporation-fission Model (GEM2) [123] when the mass number is  $A > 12$ . GEM2 could calculate evaporation not only of those six particles – n, p, d, t,  $^3\text{He}$ , and  $^4\text{He}$  – but also 60 other ones, which satisfy the

## 1. 2. Nuclide production module

---

criteria: (1) isotopes with  $Z \leq 12$ , (2) naturally existing isotopes or isotopes near the stability line, (3) isotopes with half-life longer than 1 ms.

It should be outlined that the mass number taken as a trigger for choosing a type of de-excitation is  $A = 16$  in SHIELD and  $A = 12$  in MARS.

---

---

## CHAPTER 2. EXPERIMENTAL TECHNIQUE

The experimental data for verification of the codes were collected in activation experiments. At first, the experimental targets were irradiated; afterwards, the measurements of the residual activity were done. The goal of the experiments was to study the nuclide production and depth profiles of the partial residual activities. The configuration of the targets and irradiation properties were chosen based on the results of the preliminary simulations using ATIMA [64] and FLUKA, and complementary experiments.

The following chapter describes the experimental technique in general and gives examples from actual experiments. It consists of the description of preliminary simulations, types of targets, irradiation and measurements, analysis of the  $\gamma$ -spectra and uncertainty assessment.

### 2.1. Preliminary Simulations

The goal of the present work was to obtain the experimental data for verification of the transport and nuclide production modules, therefore three types of simulations were done. At first, the stopping range of the primary ions was found using ATIMA1.2 and FLUKA (FLUKA2008.3b was used until the new release was issued in April 2011; later all the presented parameters were also recalculated using the newest version – FLUKA2011; unless specially stated, only the newest results are given according to FLUKA license agreement). Secondly, the nuclide production was studied using FLUKA. Thirdly, the additional FLUKA-simulations of the equivalent dose of the sample were performed in order to estimate cooling time until the sample could be handled after the irradiation.

All the simulations were done taking into account that a beam of a certain energy (nominal energy at an accelerator) passes through a 0.1 mm thick stainless steel (Table 1) vacuum window and a 1 m air gap before hitting the target. The loss of the beam energy in the vacuum window and air depends on the projectile species and the nominal energy before extraction. The list of all the projectiles that were studied in

## Chapter 2. Experimental technique

this work, their nominal energies at the SIS18 and the primary energies on the target as calculated using ATIMA are given in Table 2.

**Table 1. Chemical composition of the stainless steel vacuum window (in wt%).**

Fe	Cr	Ni	Mn	Mo	Si	Ti	V
72.76	17.9	6.8	1.05	0.49	0.48	0.42	0.1

**Table 2. Projectile species, their nominal energies at SIS18 and their energies after passing 0.1 mm stainless steel vacuum window and 1 m air gap (primary energy of the beam on the target).**

Projectile	$^{14}\text{N}^{7+}$	$^{40}\text{Ar}^{18+}$		$^{238}\text{U}^{73+}$									
Nominal energy, MeV	500	430	500	120	200	300	345	400	500	600	700	800	950
Primary energy on the target, MeV	498	426	496	85	174	279	325	381	483	584	684	785	935

The energy deposition function was calculated for finding the range of the primary ions. The definition of the stopping range was taken as the depth in the target where the half-maximum on the descending part of the Bragg peak is located. Table 3 shows the stopping ranges and range straggling for nitrogen, argon and uranium ions of different energies in aluminum and copper as calculated using ATIMA and two different releases of FLUKA. FLUKA2011 takes into account nuclear stopping power as well as Mott, Barkas and Bloch corrections for electronic stopping power (see Chapter 1, Section 1.1).

**Table 3. Stopping ranges and range straggling calculated using ATIMA and FLUKA for nitrogen, argon and uranium ions in aluminum and copper targets.**

Target	Projectile	Energy, AMeV	Stopping range $\pm$ range straggling, cm		
			ATIMA1.2	FLUKA2008.3b	FLUKA2011.2.4
Al	N	498	$15.647 \pm 0.042$	$15.721 \pm 0.012$	$15.622 \pm 0.012$
Al	Ar	496	$6.670 \pm 0.011$	$6.774 \pm 0.022$	$6.646 \pm 0.022$
Al	U	483	$1.523 \pm 0.001$	$1.575 \pm 0.030$	$1.496 \pm 0.030$
Cu	N	498	$5.362 \pm 0.015$	$5.496 \pm 0.013$	$5.452 \pm 0.013$
Cu	Ar	496	$2.283 \pm 0.004$	$2.320 \pm 0.015$	$2.316 \pm 0.015$

The region of interest includes the depth of two stopping ranges of the primary projectiles; therefore the total thicknesses of the experimental targets were chosen accordingly. Besides, the information about the position of the Bragg peak was used for studying the activation of this region with more precision.

## 2. 1. Preliminary simulations

For studying the nuclide production and depth-distribution, each target was divided into many discs and the partial residual activity (or the number of radioactive nuclei of certain species) of each disc was calculated at the end of the irradiation. The beam cross-section was taken to be Gaussian, with the FWHM = 2.5 cm. The targets were cylinders with the diameter  $d = 5$  cm. The obtained partial numbers of radioactive nuclei in each disc were normalized per primary projectile and per unit thickness. The simulations were done with  $1 \div 10$  million initial seeds. The production rate of the residual nuclei of interest was considered before choosing the experimental irradiation conditions.

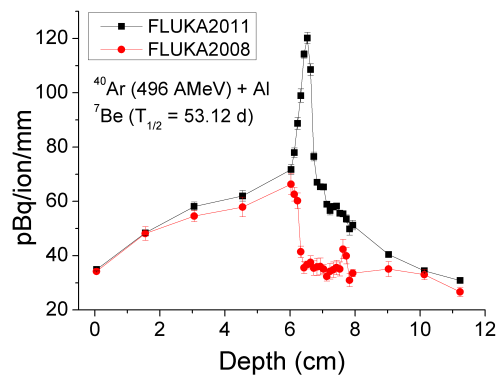


Fig. 8. FLUKA 2011 and FLUKA 2008 simulations of the residual activity depth-distribution of  ${}^7\text{Be}$  induced in an aluminum target by a 496 AMeV argon beam.

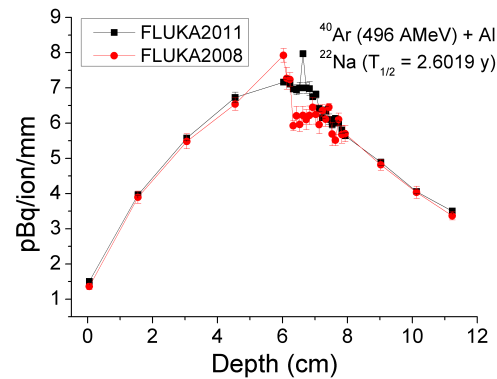


Fig. 9. FLUKA 2011 and FLUKA 2008 simulations of the residual activity depth-distribution of  ${}^{22}\text{Na}$  induced in an aluminum target by a 496 AMeV argon beam.

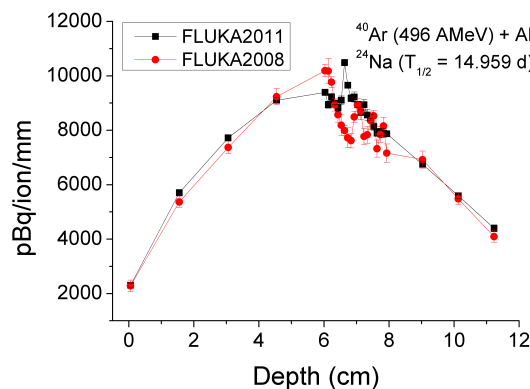


Fig. 10. FLUKA 2011 and FLUKA 2008 simulations of the residual activity depth-distribution of  ${}^{24}\text{Na}$  induced in an aluminum target by a 496 AMeV argon beam.

## Chapter 2. Experimental technique

---

Depth profiles of the residual activities of  $^7\text{Be}$ ,  $^{22}\text{Na}$  and  $^{24}\text{Na}$  produced in aluminum target irradiated by 496 AMeV argon beam as simulated by two different versions of FLUKA are shown at zero cooling down time in Figs. 8 – 10 as examples of the obtained distributions. The difference in the results appears because FLUKA2011 has several features, important for calculating the activation of a material, that were not included in the earlier version: the Barkas, Bloch and Mott corrections for electronic stopping power, nuclear stopping power (see Chapter 1, Section 1.1) and the model for heavy-ion ( $A \geq 4$ ) interactions at energies below 100 AMeV (see Chapter 1, Section 1. 2).

The simulations of the equivalent dose on the surface of the sample were done with the chosen target geometry and irradiation conditions. The decrease of the dose rate was calculated at several time points after the end of the irradiation. An example of such simulations for the surface of the aluminum target ( $d = 5$  cm,  $l = 11$  cm) irradiated by argon beam of 496 AMeV for 200 sec with the intensity  $1.08 \cdot 10^{10}$  ions/sec is shown in double logarithmic scale in Fig. 11.

The experimental total number of the projectiles on the target should be chosen very carefully. On one hand the choice is determined by the necessity of producing a sufficient amount of radioactive nuclei of interest in the material, on the other hand it is restricted by the radiation protection regulations, because high total intensities lead to high activation and therefore high dose rates.

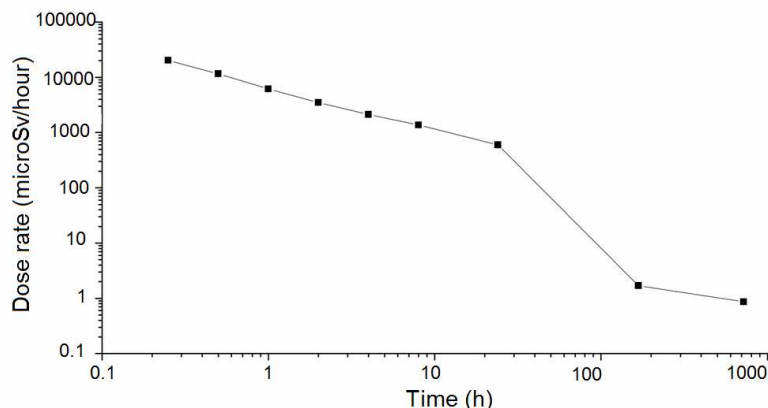


**Fig. 11.** The dose rate simulated on the surface of a thick aluminum target, irradiated by a 496 AMeV argon beam for 200 sec with the intensity  $1.08 \cdot 10^{10}$  ions/sec at different delay times.



According to Radiation Protection Regulations [124], the working areas for occupational radiation exposed persons are divided into three types: supervised areas, controlled areas and inaccessible areas. Supervised areas are those where the effective dose exceeds 1 mSv per year; in controlled areas the effective dose exceeds 6 mSv per year. The area is inaccessible when the dose rate is higher than 3 mSv/h. These rules put restrictions on handling the irradiated samples: removing them from the experimental cave, transporting to the storage room and measuring the spectra of the residual activity. The dose rates of the samples allowed for handling at GSI are typically below 20  $\mu$ Sv/h.

The cooling time of the sample could be estimated analyzing results of the dose rate simulations. The activities (or the number) of the nuclides after the irradiation could be calculated using the depth profiles of the residual activity and the radioactive decay law (see e.g. [125])

$$A(t) = A_0 \cdot \exp(-\lambda t), \quad (39)$$

where  $A_0$  is the activity (or the number of radioactive nuclei) at  $t = 0$  being the end of the irradiation,  $A(t)$  is the activity at time  $t$ ,  $\lambda$  is the decay constant  $\lambda = \ln(2)/T_{1/2}$ , and  $T_{1/2}$  is the life-time of the radioactive nucleus.

(According to the results of the simulations presented in Figs. 8 – 11, the irradiated aluminum target could be removed from the experimental cave not earlier than 3 days after the end of the irradiation; the activities of  $^7\text{Be}$ ,  $^{22}\text{Na}$  and  $^{24}\text{Na}$  in the first disc would be  $72.5 \pm 1.2$  Bq,  $3.24 \pm 0.07$  Bq and  $177.05 \pm 5.03$  Bq, respectively).

For studying the production of short-lived nuclei, the target should be handled as early as possible to measure the  $\gamma$ -spectra of residual activity. As could be seen from Figs. 8 – 10, the activation is higher in the middle of the target, where the primary beam is stopped, therefore the discs from that area should be cooled down longer before handling, than those at the front and back sides of the target. However the target could not always be accessed at a certain, optimum for removal, delay time because of the other experiments running at the facility. The thin-foil configuration was chosen to avoid high doses. Except the advantage of being removed early and measuring the decays of short-lived radioactive nuclei, such a target has the

disadvantage – the depth-profiling of the activity could not be done.

The FLUKA-simulations for studying the dependence of radioactive nuclide production on energy were done for several primary-beam energies of uranium ions: 85 AMeV, 174 AMeV, 279 AMeV, 325 AMeV, 381 AMeV, 483 AMeV, 584 AMeV, 684 AMeV, 785 AMeV and 935 AMeV (the respective nominal energies of the accelerator could be found in Table 2). The targets were aluminum discs with a diameter  $d = 5$  cm and a thickness  $t = 0.1$  cm. Energy loss in the disc could be neglected. The beam cross-section was Gaussian with FWHM = 1.5 cm and the total intensity on each target was  $1.8 \cdot 10^{14}$  ions. Ten cycles of simulations with 1 million initial seeds per cycle were run. The number of produced radioactive nuclei at the end of the irradiation was normalized per primary ion and unit thickness.

### 2.2. Types of targets

The simulations of the stopping range reveal discrepancies in the predicted values. These discrepancies are especially noticeable for heavy ions like uranium and higher energies ( $> 500$  AMeV). Complementary irradiations were done in order to check the position of the Bragg peak. A truncated cylinder covered with organic (Polyether ether ketone, PEEK) material (Fig. 12) was used for these purposes. The technique is based on the idea, that ions leave a trace on the PEEK foil if they have enough energy to reach it. The deposited energy density leaves a footprint on the foil by darkening it proportionally, thus the stopping range of the primary ions is identified by the darkest zone of the foil. Depending on the geometry of the truncated cylinder it could give different precision.

This technique was used for checking the stopping ranges of 483 AMeV uranium ions in an aluminum target (Fig. 12). The position of the maximum and comparison with the simulations is shown in Table 4.

**Table 4. Stopping range of 483 AMeV uranium in aluminum, simulations and experimental results obtained using the truncated cylinder technique.**

Stopping range $\pm$ error, cm	Stopping range $\pm$ straggling, cm		
Truncated cylinder	ATIMA	FLUKA2008.3b	FLUKA2011.2.4
$1.48 \pm 0.02$	$1.523 \pm 0.001$	$1.575 \pm 0.030$	$1.496 \pm 0.030$

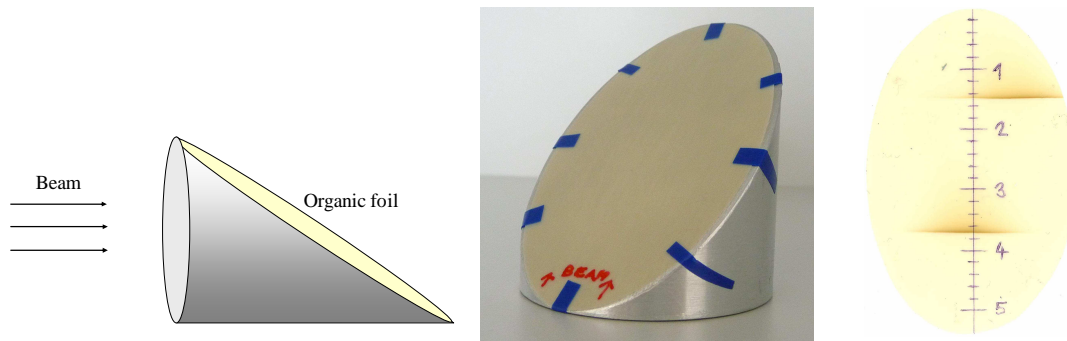


**Fig. 12.** Sketch of the truncated cylinder covered with the PEEK foil and pictures of the truncated cylinder and of the PEEK foil before (middle) and after the irradiation by 483 AMeV and 935 AMeV uranium ions (right).

The experimental targets for studying the nuclide production and depth distribution could be divided according to their configuration into two types: stacked-foil and single-foil targets.

The stacked-foil technique was used for studying the radioactive nuclei production and the in-depth distribution of activity.

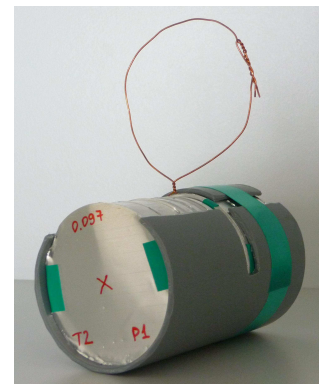
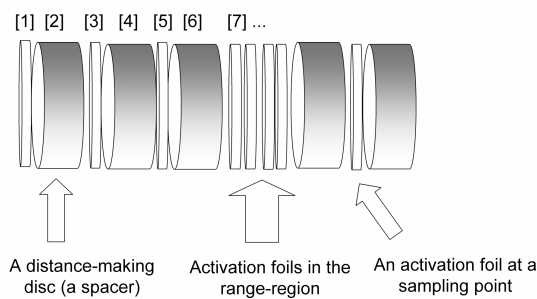


**Fig. 13.** Schematic arrangement of the thick target and the picture of the experimental target.

The thick targets were composed of thin activation foils and thick spacers of the same material (Fig. 13). The spacers were used in order to avoid the increase of uncertainties in depth introduced by a large number of thin discs. The information about the stopping range of the primary beam was used for choosing the total thickness of the target and for placing the activation foils in an optimum way. The thickness of the activation foils was chosen in a way that the activation depth profiles

would have a good resolution in the range area, and that the self-absorption of the  $\gamma$ -quanta in the foil could be neglected. These foils were analyzed using  $\gamma$ -spectroscopy methods [125] after the irradiation of the target. The number of activation foils along the full length is usually not more than fifteen, which is restricted by the capacity of the  $\gamma$ -detector to measure spectra of all these foils before the nuclei decay. Such a configuration of the target was successfully used in previous experiments of this series (see e.g. [9]).

The thin foil targets were irradiated for studying the activity of the short-lived target fragments. The thin samples should allow, on one hand, for neglecting the energy loss and  $\gamma$ -quanta absorption in the sample, and on the other hand, for irradiating the target for a reasonable time and accommodating good statistics. Thus, choosing the thickness and irradiation conditions for the thin target one should keep in mind the production rate of the nuclei of interest. Besides, such a target configuration was chosen due to radiation protection reasons, which allowed handling the target shortly after the end of the irradiation, as was mentioned above.

### 2.3. Irradiation and Measurements

The experiments were performed at the SIS18 synchrotron of GSI. All the irradiations were done in the beam dump HHD, because this extraction area provides appropriate radiation shielding allowing for high activities in the cave. Figure 14 shows the beam extraction area with the target handling system and the beam dump. The target handling system was used for installing the targets (Fig. 15) and facilitating the irradiation of several probes without entering the area.

The targets were irradiated with energies up to  $\sim 1$  AGeV in the fast-extraction regime with repetition rates of 2-3 s. The beam energy before extraction was defined by the synchrotron settings and the energy of the beam on the target after passing the vacuum window and air gap was estimated using ATIMA (see Section 2.1, Table 2). The beam cross-section was approximately Gaussian according to the profile-meter. The beam spot size (checked visually on a scintillation screen and measured using a profile-meter) was less than 3 cm in horizontal and vertical planes. Ability to focus

## 2. 3. Irradiation and measurements

the beam in such a spot size plays an important role in the experiment, because it allows for accommodating the entire beam on the target and makes the calculation of the total intensity on the target straightforward using a current transformer, which has about 3% uncertainty [126].

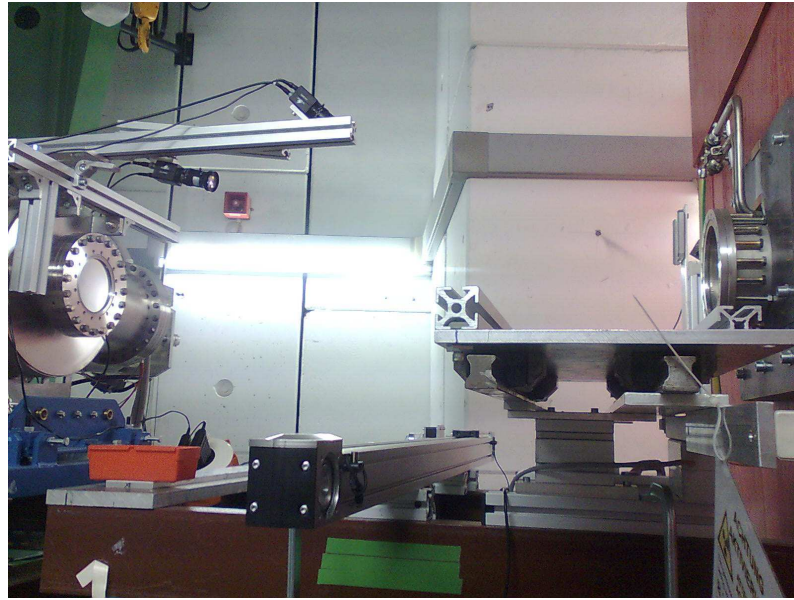


**Fig. 14. Picture of the extraction area: beam pipe, target handling system and the beam dump.**

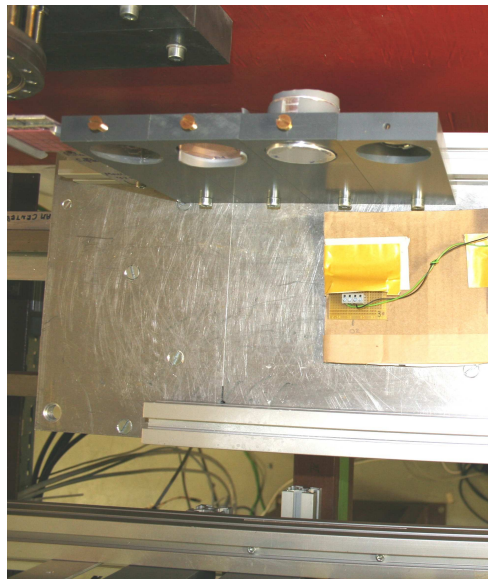


**Fig. 15. Target handling system with a scintillating target, a thin target and a thick target.**

## Chapter 2. Experimental technique

The examples of the shot-to-shot intensity of fast extracted beams are shown in Fig. 16. Differences in stability may be due to different types of ion sources and to synchrotron extraction settings.

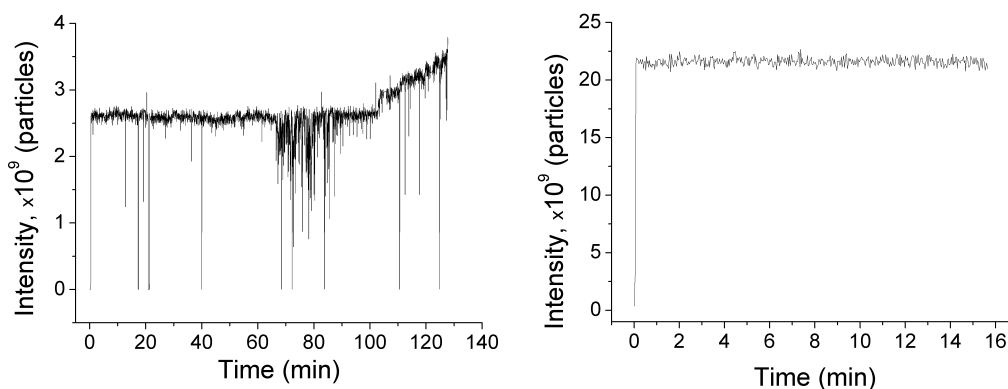


**Fig. 16. Examples of the intensity dependence on time during fast beam extraction (left side: 500 AMeV uranium beam; right side: 500 AMeV argon beam).**

After the irradiation, the targets were removed from the experimental cave and transported to the detector laboratory where the residual activity  $\gamma$ -spectra of the foils were measured using a high purity germanium (HPGe) detector. The calibration of the

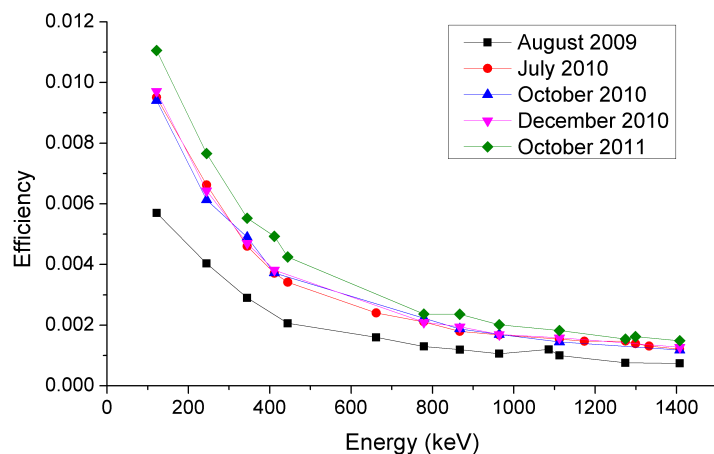


**Fig. 17. Examples of absolute efficiency curves.**

detector was done with  $^{22}\text{Na}$ ,  $^{60}\text{Co}$ ,  $^{137}\text{Cs}$  and  $^{152}\text{Eu}$  certified sources. All the targets were measured at a distance of 7 cm from the surface of the detector. The absolute efficiency of the detector at such a distance was measured before each set of

experiments. Several efficiency curves are shown as an example in Fig. 17 for different cases: Ortec GEM-20P4 detector (August 2009), the same detector after the maintenance (July 2010 – December 2010) and finally, the same detector after

before each set of

applying higher operation voltage (October 2011).

The background spectrum was measured several times at different time points for having an overview of its influence on the experimental  $\gamma$ -spectra. The sample of background  $\gamma$ -spectrum measured for 24 hours is shown in Fig. 18.

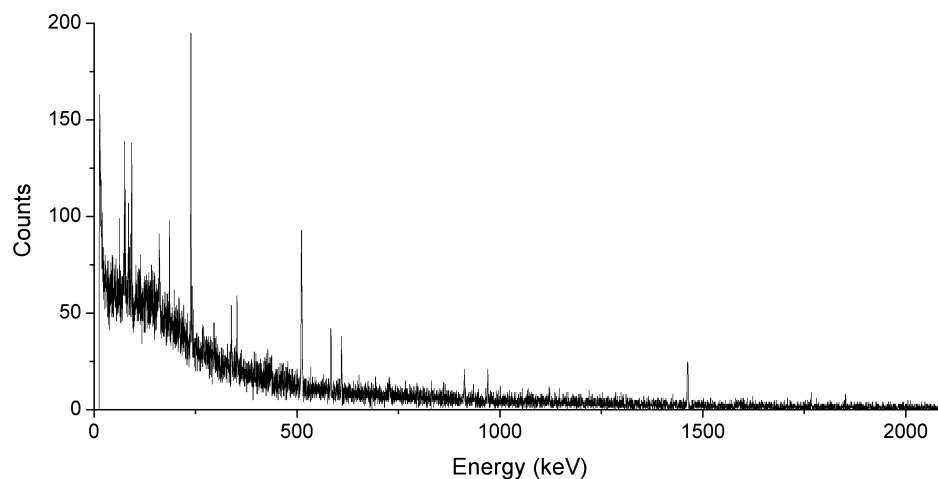


**Fig. 18. Background  $\gamma$ -spectrum measured for 24 hours.**

The measurements of the experimental  $\gamma$ -spectra started as soon as the dose rate allowed for handling the samples and the access to the beam-dump area was possible (several hours to several months after the end of irradiation). All the samples were measured several times with the same duration of the spectrum acquisition for calculating the decay constants of the  $\gamma$ -lines in the spectra. More than 5000 spectra were measured and analyzed in total.

### **2.4. Analysis of the Gamma-spectra**

Gamma-spectroscopy analysis [125] was performed in order to find the types and amounts of the produced nuclei after the irradiation. The identification of the nuclei was based on the energy of the  $\gamma$ -line, its half-life and the relations of the  $\gamma$ -emission probabilities [127; 128]. The analysis of the  $\gamma$ -spectra was done using GammaVision32 and Peakdeco [129] software packages.

An example of the  $\gamma$ -spectra of a thin aluminum foil irradiated by a 426 AMeV argon beam is shown in Fig. 19. Presented spectra were measured for one hour, the spectrum acquisition started 4 and 55 hours after the irradiation.

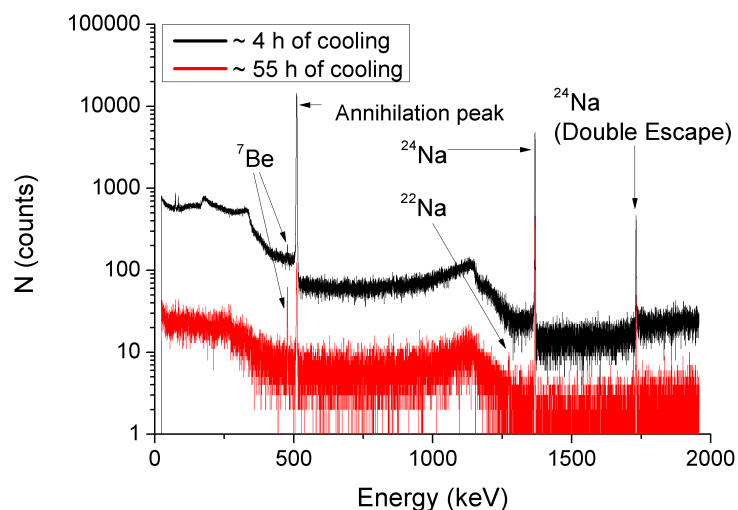


**Fig. 19.** Gamma-spectra of a thin-foil aluminum target irradiated by a 426 AMeV argon beam and measured for one hour after 4 hours and after 55 hours of cooling down, respectively.

The identification of the radioactive products was done in the following way:

- (1) FLUKA simulations were run for having an overview about the type and amount of the nuclides that can be produced in a thin-foil aluminum target irradiated by an argon beam at 426 AMeV. The results – the number of nuclides produced by one incident ion per unit thickness at the end of irradiation – are presented in Table 5. Most of the listed nuclides are too short-lived with respect to the time point of the earliest possible measurement (half life below 30 min), or are not  $\gamma$ -emitters or both, thus their presence could not be verified in the present activation experiment. The only nuclides that could be registered are  $^7\text{Be}$ ,  $^{22}\text{Na}$ ,  $^{24}\text{Na}$ ,  $^{52}\text{Mn}$  and  $^{58}\text{Co}$ .  $^{58}\text{Co}$  was below the minimum detectable activity (MDA) of 10 Bq determined from the earliest (96 minutes after the end of irradiation) measured spectrum. The MDA was calculated using the Curie concept with 95% confidence level, it corresponds to the  $3.71 \cdot 10^{-6}$  nuclides per



primary ion per mm. The production of  $^{52}\text{Mn}$  was  $(1.88 \pm 0.33) \cdot 10^{-7}$  nuclides/ion/mm, which is in agreement with the FLUKA prediction. However, it is about 3 orders of magnitude less than the production of  $^7\text{Be}$ ,  $^{22}\text{Na}$  and  $^{24}\text{Na}$ . Moreover,  $^{52}\text{Mn}$  and  $^{58}\text{Co}$  are not the products of aluminum target-nuclei. They are generated due to the presence of other elements in the target material. That is why only  $^7\text{Be}$ ,  $^{22}\text{Na}$  and  $^{24}\text{Na}$  were subject to further studies;

- (2) The energies of the  $\gamma$ -maxima in the spectrum were compared with those from the data bases [127; 128];  $\gamma$ -quanta with energies 477.6 keV, 1274.5 keV and 1368.6 keV correspond to  $^7\text{Be}$ ,  $^{22}\text{Na}$  and  $^{24}\text{Na}$  decays, respectively;
- (3) The  $\gamma$ -spectra were measured several times in order to check the decrease of the intensity and the half-lives of the decaying nuclides (e.g. Fig. 19);
- (4) The rest of the  $\gamma$ -quanta present in the spectrum are not emitted as a result of de-excitation of nuclear levels, and therefore could not be used in  $\gamma$ -spectroscopy. Gammas at 511 keV represent the annihilation peak, which appears in the spectrum due to annihilation of the positrons and electrons in the target [125]. Gammas at 1732 keV are caused by the escape from the detector of two annihilation photons (double escape peak) during the absorption of the initial gamma-ray having 2754 keV (Table 6, Fig. 20).

## Chapter 2. Experimental technique

**Table 5. The results of FLUKA-simulations on thin-foil aluminum target activation by a 426 AMeV argon beam.**

Nuclide	Nuclide/ion/mm	Decay mode	Half-life	Nuclide	nuclide/ion/mm	Decay mode	Half-life
<sup>3</sup> H	$(4.57 \pm 0.12) \cdot 10^{-4}$	$\beta^-$	12.323 y	<sup>20</sup> O	$(2.37 \pm 1.69) \cdot 10^{-9}$	$\beta^-$	13.51 s
<sup>6</sup> He	$(2.74 \pm 0.38) \cdot 10^{-9}$	$\beta^-$	806.7 ms	<sup>17</sup> F	$(7.55 \pm 1.95) \cdot 10^{-8}$	$\epsilon + \beta^+$	64.5 s
<sup>8</sup> He	$(9.75 \pm 2.58) \cdot 10^{-11}$	$\beta^-, \beta^- n$	119.0 ms	<sup>18</sup> F	$(3.21 \pm 0.28) \cdot 10^{-6}$	$\epsilon + \beta^+$	109.7 m
<sup>8</sup> Li	$(5.23 \pm 0.32) \cdot 10^{-9}$	$\beta^-, \beta^- 2\alpha$	840.3 ms	<sup>20</sup> F	$(2.02 \pm 0.54) \cdot 10^{-8}$	$\beta^-$	11.0 s
<sup>9</sup> Li	$(2.40 \pm 0.54) \cdot 10^{-10}$	$\beta^-, \beta^- n 2\alpha$	178.3 ms	<sup>21</sup> F	$(2.43 \pm 0.73) \cdot 10^{-9}$	$\beta^-$	4.16 s
<sup>11</sup> Li	$(1.51 \pm 1.07) \cdot 10^{-12}$	$\beta^-, \beta^- n 2\alpha$	8.5 ms	<sup>22</sup> F	$(2.48 \pm 2.48) \cdot 10^{-10}$	$\beta^-$	4.23 s
<sup>7</sup> Be	$(2.01 \pm 0.11) \cdot 10^{-4}$	$\epsilon$	53.29 d	<sup>17</sup> Ne	$(6.39 \pm 6.39) \cdot 10^{-12}$	$\epsilon + \beta^+, \epsilon p, \epsilon \alpha$	109.2 ms
<sup>8</sup> Be	$(6.12 \pm 0.48) \cdot 10^{-25}$	$2\alpha$	$6.70 \cdot 10^{-17}$ s	<sup>18</sup> Ne	$(3.91 \pm 2.61) \cdot 10^{-10}$	$\epsilon + \beta^+$	1672 ms
<sup>10</sup> Be	$(6.36 \pm 1.02) \cdot 10^{-5}$	$\beta^-$	$1.6 \cdot 10^6$ y	<sup>19</sup> Ne	$(1.92 \pm 0.49) \cdot 10^{-9}$	$\epsilon + \beta^+$	17.22 ms
<sup>11</sup> Be	$(5.80 \pm 1.79) \cdot 10^{-9}$	$\beta^-, \beta^- \alpha$	13.81 s	<sup>23</sup> Ne	$(3.49 \pm 0.81) \cdot 10^{-8}$	$\beta^-$	37.24 s
<sup>12</sup> Be	$(2.49 \pm 1.66) \cdot 10^{-12}$	$\beta^-$	23.6 ms	<sup>24</sup> Ne	$(4.75 \pm 1.94) \cdot 10^{-8}$	$\beta^-$	3.38 m
<sup>14</sup> Be	$(2.55 \pm 2.55) \cdot 10^{-13}$	$\beta^-, \beta^- n, \beta^- 2n$	4.35 ms	<sup>21</sup> Na	$(1.58 \pm 0.43) \cdot 10^{-8}$	$\epsilon + \beta^+$	22.49 s
<sup>8</sup> B	$(1.44 \pm 0.29) \cdot 10^{-9}$	$\epsilon + \beta^+, \epsilon 2\alpha$	770 ms	<sup>22</sup> Na	$(1.62 \pm 0.16) \cdot 10^{-4}$	$\epsilon + \beta^+$	2.603 y
<sup>9</sup> B	$(2.81 \pm 0.77) \cdot 10^{-28}$	$2\alpha p$	$8.0010^{-19}$ s	<sup>24</sup> Na	$(1.10 \pm 0.11) \cdot 10^{-4}$	$\beta^-$	14.958 h
<sup>12</sup> B	$(3.67 \pm 0.94) \cdot 10^{-11}$	$\beta^-, \beta^- 3\alpha$	20.20 ms	<sup>24m</sup> Na	$(7.40 \pm 1.49) \cdot 10^{-11}$	IT, $\beta^-$	20.20 ms
<sup>13</sup> B	$(1.81 \pm 0.41) \cdot 10^{-11}$	$\beta^-, \beta^- n$	17.33 ms	<sup>25</sup> Na	$(2.14 \pm 0.26) \cdot 10^{-8}$	$\beta^-$	59.1 s
<sup>14</sup> B	$(1.54 \pm 0.95) \cdot 10^{-12}$	$\beta^-$	13.8 ms	<sup>22</sup> Mg	$(6.77 \pm 3.45) \cdot 10^{-10}$	$\epsilon + \beta^+$	3.857 s
<sup>9</sup> C	$(4.44 \pm 1.21) \cdot 10^{-11}$	$\epsilon + \beta^+, \epsilon p 2\alpha$	126.5 ms	<sup>23</sup> Mg	$(1.66 \pm 0.33) \cdot 10^{-8}$	$\epsilon + \beta^+$	11.3 s
<sup>10</sup> C	$(2.03 \pm 0.62) \cdot 10^{-8}$	$\epsilon + \beta^+$	19.3 s	<sup>27</sup> Mg	$(1.18 \pm 0.44) \cdot 10^{-7}$	$\beta^-$	9.458 s
<sup>11</sup> C	$(1.04 \pm 0.09) \cdot 10^{-5}$	$\epsilon + \beta^+$	20.38 m	<sup>24</sup> Al	$(1.09 \pm 1.09) \cdot 10^{-10}$	$\epsilon + \beta^+, \epsilon \alpha$	2.053 s
<sup>14</sup> C	$(3.71 \pm 0.48) \cdot 10^{-5}$	$\beta^-$	5730 y	<sup>25</sup> Al	$(1.09 \pm 0.21) \cdot 10^{-8}$	$\epsilon + \beta^+$	7.18 s
<sup>15</sup> C	$(2.87 \pm 1.91) \cdot 10^{-10}$	$\beta^-$	2.449 s	<sup>26</sup> Al	$(3.07 \pm 0.13) \cdot 10^{-4}$	$\epsilon + \beta^+$	7.2E+5 y
<sup>16</sup> C	$(1.75 \pm 0.71) \cdot 10^{-10}$	$\beta^-, \beta^- n$	0.747 s	<sup>26m</sup> Al	$(1.14 \pm 0.54) \cdot 10^{-7}$	$\epsilon + \beta^+$	6.3452 s
<sup>12</sup> N	$(1.29 \pm 8.58) \cdot 10^{-12}$	$\epsilon + \beta^+, \epsilon 3\alpha$	11.0 ms	<sup>26</sup> Si	$(1.31 \pm 1.31) \cdot 10^{-10}$	$\epsilon + \beta^+$	2.234 s
<sup>13</sup> N	$(8.40 \pm 2.23) \cdot 10^{-7}$	$\epsilon + \beta^+$	9.96 m	<sup>27</sup> Si	$(2.43 \pm 2.44) \cdot 10^{-10}$	$\epsilon + \beta^+$	4.16 s
<sup>16</sup> N	$(1.46 \pm 0.24) \cdot 10^{-8}$	$\beta^-, \beta^- \alpha$	7.13 s	<sup>39</sup> Ar	$(9.98 \pm 9.98) \cdot 10^{-7}$	$\beta^-$	269 y
<sup>17</sup> N	$(1.22 \pm 0.55) \cdot 10^{-9}$	$\beta^-, \beta^- n$	4.17 s	<sup>49</sup> V	$(9.74 \pm 9.74) \cdot 10^{-7}$	$\epsilon$	330 d
<sup>13</sup> O	$(1.00 \pm 0.67) \cdot 10^{-12}$	$\epsilon + \beta^+, \epsilon p$	8.58 ms	<sup>51</sup> Cr	$(1.99 \pm 1.32) \cdot 10^{-6}$	$\epsilon$	27.7025 d
<sup>14</sup> O	$(8.26 \pm 5.50) \cdot 10^{-9}$	$\epsilon + \beta^+$	70.606 s	<sup>52</sup> Mn	$(4.98 \pm 4.98) \cdot 10^{-7}$	$\epsilon + \beta^+$	5.591 d
<sup>15</sup> O	$(2.22 \pm 0.46) \cdot 10^{-7}$	$\epsilon + \beta^+$	2.03 m	<sup>55</sup> Fe	$(9.98 \pm 9.98) \cdot 10^{-7}$	$\epsilon$	2.73 y
<sup>19</sup> O	$(9.29 \pm 4.72) \cdot 10^{-9}$	$\beta^-$	26.91 s	<sup>58</sup> Co	$(6.07 \pm 6.07) \cdot 10^{-7}$	$\epsilon + \beta^+$	70.86 d

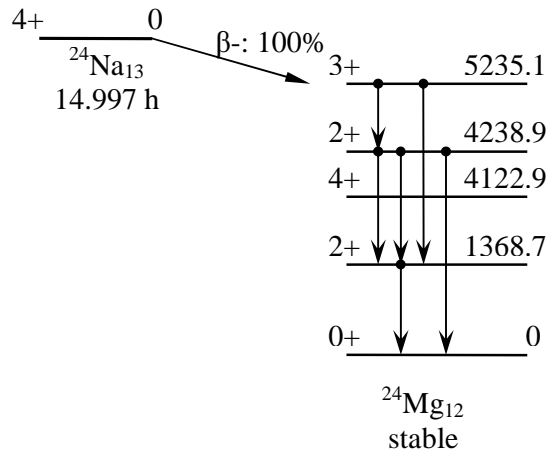


Table 6.  $\beta^-$  decay of  $^{24}\text{Na}$ : energies of the  $\gamma$ -quanta and probabilities of their emission, with uncertainties indicated in italic [128].

$E_\gamma$ , keV	$I_\gamma$ , %
996.6 <i>10</i>	0.00210 <i>20</i>
1368.626 <i>5</i>	99.9936 <i>15</i>
2754.007 <i>11</i>	99.855 <i>5</i>
2871.0 <i>10</i>	0.00025 <i>4</i>
3866.22 <i>15</i>	0.074 <i>3</i>
4238.9 <i>10</i>	0.00084 <i>10</i>

Fig. 20.  $\beta^-$ -decay scheme of  $^{24}\text{Na}$ .

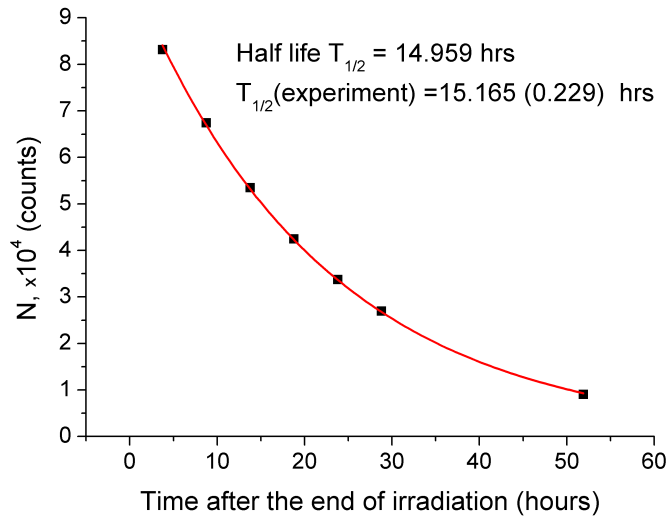
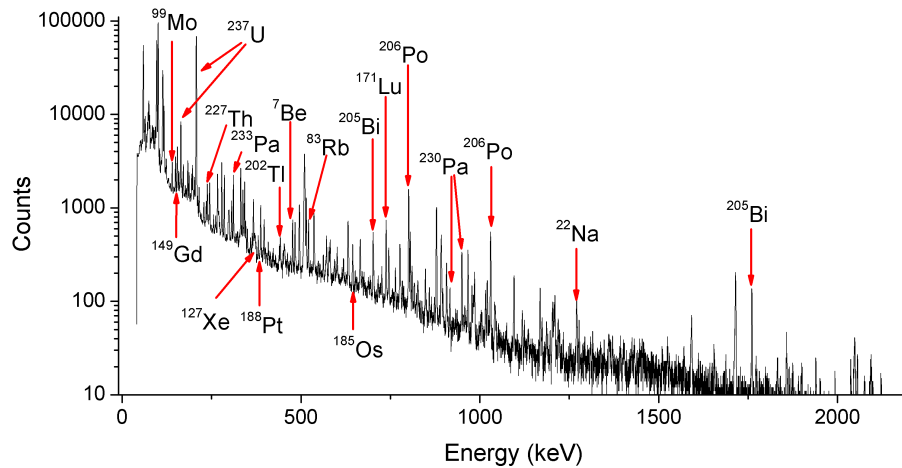


Fig. 21. Intensity dependence on time for  $\gamma$ -line with  $E = 1368.6$  keV, measured data and fit.

In case of heavy targets or projectiles the number of produced radioactive nuclei dramatically increases. For example, a  $\gamma$ -spectrum of one of the foils in the range area of the 483 AMeV uranium beam in an aluminum target is presented in Fig. 22.



**Fig. 22. Gamma-spectrum of an activation foil located in the middle of a thick aluminum target irradiated by a 483 AMeV uranium beam.**

The identification of the nuclei was done following the steps described above:

- (1) FLUKA-simulations showed that 1723 radioactive nuclei could be produced in a thick aluminum target irradiated by uranium. Of course, not all of them could be detected by using the chosen experimental technique; however the number of  $\gamma$ -emitting nuclei with appropriate half-lives would be quite big.
- (2) Energy search revealed many nuclei with similar energies of emitted  $\gamma$ -quanta.
- (3) Measurements of half-lives confirmed that some of the  $\gamma$ -peaks are created by several decaying nuclei. In case when one of these nuclei is long-lived it is possible to distinguish its percentage on the total activity by waiting until the short-lived nuclei decay and measuring the  $\gamma$ -spectra at a later time.
- (4) Extra  $\gamma$ -lines appearing in the spectrum, but not identified by their energies could be [125]:
  - a. Single and double escape peaks (escape of one or two annihilation photons from the detector);

- b. True coincidence summing effects (summation by a detector of two or more  $\gamma$ -quanta emitted in coincidence and their interpretation as a single  $\gamma$ -line).

When the nuclei of type  $i$  are accurately identified, their amount at the end of irradiation  $N_{eoi}$  is calculated from the radioactivity decay law (see e.g. [125]) and is found using the formula

$$N_{eoi} = \frac{\Delta N_i}{\exp(-\lambda_i \cdot t_d) \cdot [1 - \exp(-\lambda_i \cdot t_m)] \cdot P_{i\gamma} \cdot eff}, \quad (40)$$

where  $\Delta N_i$  is the peak-net-area determined by GammaVision32 or Peakdeco software from the  $\gamma$ -spectrum acquired at time  $t_d$  after the end of irradiation ( $t_d$  being the start of the measurement),  $\lambda_i$  is the decay constant of a certain nuclide,  $t_m$  is the live time of the spectrum acquisition (effective time during which the signal builds up),  $P_{i\gamma}$  is the gamma emission probability according to the decay scheme of the nuclide [127; 128] and  $eff$  is the detector absolute efficiency. This number was normalized per primary projectile and per unit thickness.

It should be kept in mind that radioactive nuclei are produced not only directly in nuclear reactions, but also through decays of the other radioactive nuclei or de-excitation of isomeric states. In this case the amount of radioactive daughter nuclei of interest could not be calculated at the end of irradiation using eq. (40). The goal of the present work is verification of the Monte Carlo transport codes, therefore for verification purposes it is enough to calculate the amount of certain nuclei at any later time point taking into account the creation through all the possible channels. However most of the isotopes detected in these experiments were not produced through decay chains; their amount is given at the end of irradiation. Every other case would be discussed separately in the respective section.

The results of the performed experiments in comparison with the simulations are discussed in Chapter 3.

### 2.5. Uncertainty Assessment

The accuracy of the number of nuclides (or their activities), obtained in thin- and thick-target experiments, is determined by the accuracy of the following components:

- (1) Peak net area. The uncertainty of this component depends on the number of counts in the peak and on the peak-to-Compton ratio. It is indicated by the software: Gamma-Vision 32 and Paekdeco.
- (2) Half-life and gamma emission probability. These values and their uncertainties are taken from the data bases [127].
- (3) Absolute efficiency of the detector. Uncertainty of this parameter comprises several components: uncertainty of the calibration source (certified relative standard-uncertainty is less than 2 %), uncertainty of the peak net area (is less than 2%) and uncertainty of fitting the curve (depends on energy and varies from 1% to 7%).
- (4) Thickness of the activation foil. The thickness is measured with an uncertainty of less than 0.5%.
- (5) Total beam current on the target. Is measured using the current transformer, the uncertainty is 3 %. The resulting error from many shots was then calculated adequately. However there is an exception when the machine is unstable and intensities at the extraction vary by more than one order of magnitude: In this case the current transformer is not able to scale and measure properly. Therefore the uncertainties become even larger, depending on the number of miscalculated shots. Cycles varying more then in a certain limit are dropped.

In case of a thick target experiment, besides an uncertainty of the number of nuclides there is also a depth and a resolution uncertainty. Depth uncertainty is interpreted as the uncertainty of the foil position in the target; it can be measured with 0.05 mm precision. Resolution of the experiment is defined by the thickness of an activation foil and its uncertainty, which is measured to be less than 0.5 %.

---

---



---

## CHAPTER 3. EXPERIMENTAL RESULTS AND COMPARISON WITH THE SIMULATIONS

This Chapter presents the results of the completed experiments in comparison with the according simulations. The chapter is divided into two sections. The first one is devoted to the activation of aluminum; the second one describes the activation of copper. Each section is divided into subsections according to projectile species.

### 3.1. Activation of aluminum

The target material consisted of Al (99.2 wt%), Si (0.25 wt%), Fe (0.4 wt%), Mn (0.05 wt%), Cu (0.05 wt%) and Mg (0.05 wt%). Aluminum targets were irradiated by nitrogen, argon, and uranium ions.

#### 3.1.1. Activation of aluminum by a nitrogen beam

A thick aluminum target was irradiated by a nitrogen beam  $^{14}\text{N}^{7+}$  of 498 AMeV. The stopping range of 498 AMeV nitrogen ions in aluminum is approximately 15.63 cm according to FLUKA2011 simulations (see Table 3), therefore the total thickness of the target was chosen to be ~30 cm. The configuration of the irradiated target is presented in Table 7. The total intensity accumulated on the target within 20 minutes was  $1.01 \cdot 10^{13} \pm 1.25 \cdot 10^{10}$  ions, the beam cross-section was Gaussian with a FWHM of 3 cm. Measurements of the  $\gamma$ -spectra of activation foils started 45 hours after the end of the irradiation. Each activation foil was measured several times after different time delays. The real time of the measurement varied from 30 minutes to 2 hours, the dead time due to count rate varied from ~3% to 0.1%. Seventy two spectra were acquired and analyzed in total. Spectra of the first disc measured approximately 2 days and 10 days after the end of irradiation are shown as an example in Fig. 23.

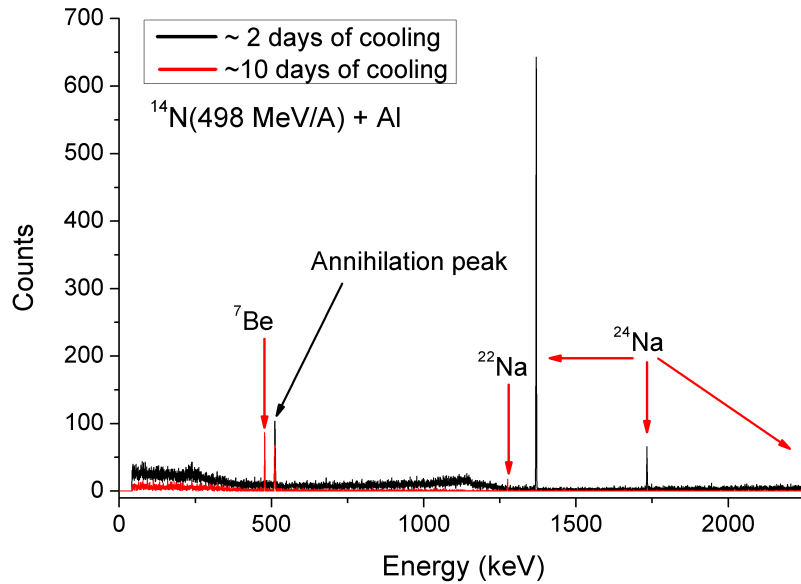


Fig. 23. Spectra of the disc # 1 measured approximately 2 days and 10 days after the end of the irradiation of an aluminum target by a 498 AMeV nitrogen beam.

Table 7. Configuration of the thick aluminum target irradiated by a 498 AMeV nitrogen beam.

Disc number	[1]	[2]	[3]	[4]	[5]	[6]	[7]
Disc thickness, mm	0.999	53.98	0.998	54.03	0.998	33.98	5.025
Disc number	[8]	[9]	[10]	[11]	[12]	[13]	[14]
Disc thickness, mm	0.999	2.995	1	0.998	0.998	0.999	0.997
Disc number	[15]	[16]	[17]	[18]	[19]	[20]	[21]
Disc thickness, mm	0.997	34.02	0.998	54.03	1	54.01	1

Irradiation of aluminum by a nitrogen ( $Z = 7$ ) beam leads to a production of three  $\gamma$ -emitting radioactive nuclei which are sufficiently long-lived to be detected in present experiment:  ${}^7\text{Be}$ ,  ${}^{22}\text{Na}$  and  ${}^{24}\text{Na}$ . Both  ${}^{22}\text{Na}$  and  ${}^{24}\text{Na}$  are fragments of the target, whereas  ${}^7\text{Be}$  is a target fragment when positioned upstream the stopping range of nitrogen. Downstream of the nitrogen range there is a mixture of target and stopped projectile fragments.

None of the produced isotopes are intermediate products in the chain reactions; therefore eq. (40) was applicable. The number of isotopes at the end of irradiation was normalized to unit thickness and to the integrated projectile number on the target. The experimental results in comparison with FLUKA-simulations are shown in Figs. 24 – 26.

### 3. 1. Activation of aluminum

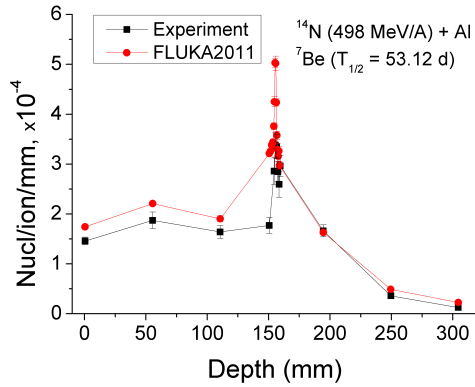


Fig. 24. Depth profile of  ${}^7\text{Be}$  produced in the aluminum target irradiated by a 498 AMeV nitrogen beam.

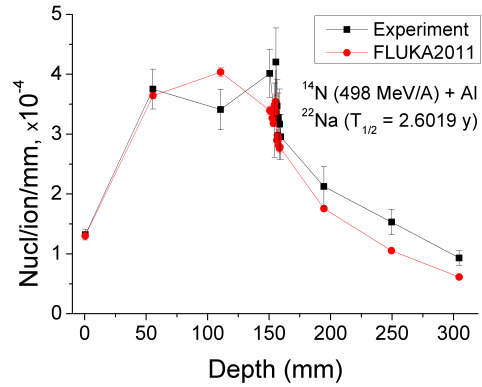


Fig. 25. Depth profile of  ${}^{22}\text{Na}$  produced in the aluminum target irradiated by a 498 AMeV nitrogen beam.

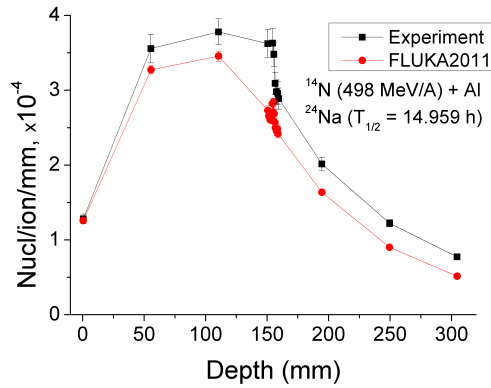


Fig. 26. Depth profile of  ${}^{24}\text{Na}$  produced in the aluminum target irradiated by a 498 AMeV nitrogen beam.

Total numbers of each identified isotope deposited in the whole target volume are shown in Table 8 for zero cooling time.

**Table 8. Partial number of deposited isotopes in the whole aluminum target volume ( $l \approx 30$  cm,  $d = 5$  cm) per projectile. The incident beam was 498 AMeV nitrogen. The numbers are given for zero cooling time.**

Nuclide	Experiment, Nuclides/ion	FLUKA, Nuclides/ion
${}^7\text{Be}$	$0.0431 \pm 0.0035$	$0.0515 \pm 0.0012$
${}^{22}\text{Na}$	$0.0774 \pm 0.0086$	$0.0727 \pm 0.0032$
${}^{24}\text{Na}$	$0.0743 \pm 0.0036$	$0.0636 \pm 0.0013$

FLUKA agrees with the experiment in simulating the  ${}^7\text{Be}$  and  ${}^{22}\text{Na}$  depth profiles within 10% on average and within 15% in simulating  ${}^{24}\text{Na}$  depth profile. However

there is a deviation in the density distribution in the range area: the maximum in the  $^7\text{Be}$  distribution is  $\sim 70\%$  higher when simulated using FLUKA, in case of  $^{22}\text{Na}$  the relative height of the maximum in FLUKA-simulations is approximately the same as in the experiment, in case of  $^{24}\text{Na}$  no maximum was observed in the experiment. The experimental and simulated by FLUKA partial numbers of the isotopes deposited in the whole target volume agree within the error bars.

### 3.1.2. Activation of aluminum by argon

The thin-foil aluminum target,  $l = 0.1 \pm 0.005$  mm,  $d = 5$  cm, was irradiated by a 426 AMeV argon beam for 6.85 hours. The total number of projectiles accumulated on the target was  $2.38 \cdot 10^{14} \pm 6.65 \cdot 10^{10}$  ions, the beam cross-section was Gaussian with a FWHM of 1 cm. The first gamma-spectra acquisition started 96 minutes after the end of the irradiation. It was then followed by measurements after several delay times and stopped finally 2 weeks after the end of the irradiation. The real time of the measurements varied from 5 minutes with 7 % dead time for the first spectra, up to 25 hours with 0.1% dead time for the spectra acquired 2 weeks after the end of irradiation. Fifty six spectra were measured and analyzed. The obtained numbers of radioactive target fragments  $^7\text{Be}$ ,  $^{22}\text{Na}$  and  $^{24}\text{Na}$  in comparison with FLUKA-simulations are given in Table 9.

**Table 9. Production of  $^7\text{Be}$ ,  $^{22}\text{Na}$  and  $^{24}\text{Na}$  in the thin-foil aluminum target irradiated by a 426 AMeV argon beam: experiment and FLUKA simulations.**

	$^7\text{Be}$ , Nuclides/ion/mm	$^{22}\text{Na}$ , Nuclides/ion/mm	$^{24}\text{Na}$ , Nuclides/ion/mm
Experiment	$2.08 \cdot 10^{-4} \pm 1.29 \cdot 10^{-5}$	$1.62 \cdot 10^{-4} \pm 8.86 \cdot 10^{-6}$	$1.11 \cdot 10^{-4} \pm 5.63 \cdot 10^{-6}$
FLUKA	$2.01 \cdot 10^{-4} \pm 1.13 \cdot 10^{-5}$	$1.62 \cdot 10^{-4} \pm 1.58 \cdot 10^{-5}$	$1.10 \cdot 10^{-4} \pm 7.13 \cdot 10^{-6}$

The production of the radioactive nuclides in the thin-foil aluminum target irradiated by a 426 AMeV argon beam and corresponding FLUKA-simulations agree within the error bars, as can be seen from Table 9.

A thick aluminum target was irradiated by a 496 AMeV argon beam with circular profile and a FWHM of 2 cm. The total number of projectiles on the target was  $1.01 \cdot 10^{13} \pm 1.40 \cdot 10^{10}$ , the irradiation took 16 min. The geometry of the thick aluminum target is listed quantitatively in Table 10. The standard uncertainty of the

### 3.1. Activation of aluminum

thickness does not exceed 0.5 %. The overall length of the target was 11.062 cm, the diameter of all foils and discs was 5 cm. The thin activation foils were used for gamma-spectroscopy. Three series of measurements were performed: 28 – 40 days, 49 – 69 days and 89 – 95 days after the end of irradiation, respectively. The duration of each single-foil measurement was about 24 hours with a dead time below 1%. Fifty two spectra were measured and processed. As the measurements of the spectra started approximately 1 month after the end of irradiation, the short-lived (14.959 h)  $^{24}\text{Na}$  isotope decayed below the minimum detectable activity. Thus only  $^7\text{Be}$  and  $^{22}\text{Na}$  were detected in this case. The measured and simulated depth profiles for those two nuclides are shown in Fig. 27 ( $^7\text{Be}$ ) and Fig. 28 ( $^{22}\text{Na}$ ).

**Table 10. Configuration of the thick aluminum target irradiated by a 496 AMeV argon beam.**

Foil number	[1]	[2]	[3]	[4]	[5]	[6]	[7]
Foil thickness, mm	1.0	14.02	1.0	14.01	1.0	13.89	1.0
Foil number	[8]	[9]	[10]	[11]	[12]	[13]	[14]
Foil thickness, mm	13.88	1.0	1.0	1.0	1.0	1.0	1.0
Foil number	[15]	[16]	[17]	[18]	[19]	[20]	
Foil thickness, mm	14.00	0.98	13.99	0.98	13.89	0.98	

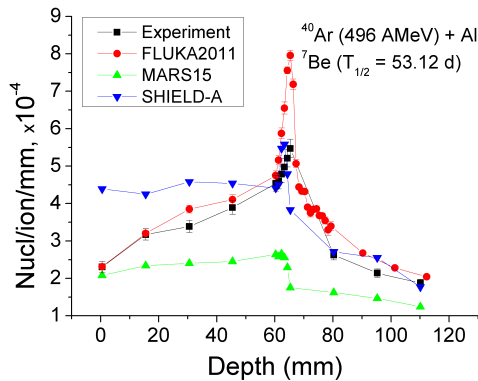


**Fig. 27. Depth profile of  $^7\text{Be}$  produced in an aluminum irradiated by 496 AMeV argon ions.**

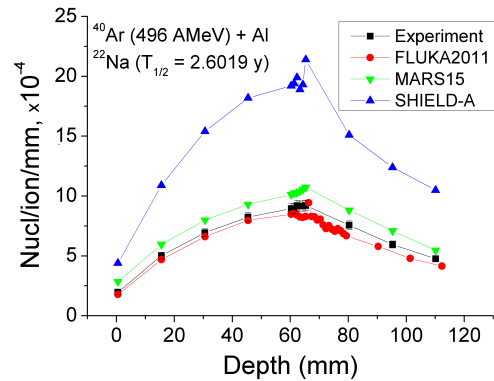


**Fig. 28. Depth profile of  $^{22}\text{Na}$  produced in an aluminum irradiated by 496 AMeV argon ions.**

Partial numbers of deposited isotopes in the whole target volume are shown in Table 11.

## Chapter 3. Experimental results and comparison with the simulations

---

**Table 11. Partial number of deposited isotopes in the whole aluminum target ( $l \approx 11$  cm,  $d = 5$  cm) per projectile. The incident beam was 496 AMeV argon. The numbers are given for zero cooling time.**

Nuclide	Experiment, Nuclides/ion	FLUKA, Nuclides/ion	MARS, Nuclides/ion	SHIELD, Nuclides/ion
$^7\text{Be}$	$0.0358 \pm 0.0018$	$0.0396 \pm 0.0009$	$0.0224 \pm 0.0007$	$0.0407 \pm 0.0008$
$^{22}\text{Na}$	$0.0735 \pm 0.0037$	$0.0690 \pm 0.0010$	$0.0855 \pm 0.0017$	$0.1592 \pm 0.0032$

FLUKA gives on average 5% agreement with the experiment, however peculiarities in the range area should be considered: the maxima in the nuclide distributions. In case of  $^7\text{Be}$  the maximum concentration given by FLUKA is ~70% higher than in the experiment. In case of  $^{22}\text{Na}$  no peak is observed in the experiment, while FLUKA shows just a little discontinuity and in general is in a good agreement.

The MARS-results for the number of  $^7\text{Be}$  agree with the experiment within 5% only in the first disc of the assembly. Otherwise the  $^7\text{Be}$  distribution does not match the shape of the experimental depth profile: MARS gives a constant concentration of  $^7\text{Be}$  upstream and downstream the range and does not reproduce the peak in the range area. The total number of  $^7\text{Be}$  in the whole target volume is underestimated by approximately 40%. Concerning the behavior of  $^{22}\text{Na}$  distribution, MARS describes it in principle correctly, but absolute values differ. The simulations give approximately 10% higher results on average.

Analyzing the results of SHIELD simulations, one could see that the distribution upstream the range is constant and there is a factor two difference in the  $^7\text{Be}$  concentration in the first disc of the target assembly. But comparing to MARS results, SHIELD reproduces a maximum in the range area and agrees with the experiment downstream the range. In case of  $^{22}\text{Na}$ , SHIELD is able to reproduce the shape of the experimental distribution; however the absolute values for the isotope production are at least 2 times higher.

### 3.1.3. Activation of aluminum by uranium

Several thin-foil aluminum targets were irradiated by uranium beams of different energies. Irradiation energies, beam cross-sections (FWHM in horizontal and vertical

### 3. 1. Activation of aluminum

direction), total numbers of the projectiles on the target as well as the thicknesses of the thin aluminum discs are given in Table 12. The diameters of the discs are 5 cm.

**Table 12. Irradiation of aluminum foils by uranium ions: irradiation conditions and foil parameters (diameter of each foil was 5 cm).**

Energy of the beam, AMeV	85	174	279	325	381
Duration of irradiation, sec	1518	2242	3627	4620	2149
Beam cross-section, FWHM, x, y, cm	2.5, 2.5	2.5, 2.5	2.5, 2.5	2.0, 2.0	2.5, 2.5
Total number of projectiles	$3.03 \cdot 10^{12}$ $\pm 2.74 \cdot 10^9$	$3.09 \cdot 10^{12}$ $\pm 2.85 \cdot 10^9$	$5.25 \cdot 10^{12}$ $\pm 3.63 \cdot 10^9$	$1.09 \cdot 10^{13}$ $\pm 8.65 \cdot 10^9$	$3.07 \cdot 10^{12}$ $\pm 2.92 \cdot 10^9$
Foil thickness, mm	0.504	0.503	0.503	0.2	0.504
Energy of the beam, AMeV	483	584	684	785	935
Duration of irradiation, sec	11811	2451	3051	4491	16128
Beam cross-section, FWHM, x, y, cm	1.2, 2.5	2.5, 2.0	2.5, 2.0	2.0, 2.0	2.0, 3.5
Total number of projectiles	$1.21 \cdot 10^{13}$ $\pm 4.5 \cdot 10^9$	$2.8 \cdot 10^{12}$ $\pm 2.45 \cdot 10^9$	$2.79 \cdot 10^{12}$ $\pm 2.2 \cdot 10^9$	$2.73 \cdot 10^{12}$ $\pm 2.06 \cdot 10^9$	$1.6 \cdot 10^{12}$ $\pm 8.72 \cdot 10^8$
Foil thickness, mm	0.505	0.504	0.504	0.504	0.505

The measurements of the residual activity  $\gamma$ -spectra of the thin-foil targets were started a few hours to few days after the end of the irradiation, with the exception of aluminum target irradiated by 935 AMeV. In this case the measurements started several months after the end of irradiation, because this foil was a part of thick-target assembly (not discussed in present work) and due to radiation protection reasons and other running experiments could not be accessed earlier. Therefore the amount of  $^{24}\text{Na}$  could not be studied in this experiment.

All the targets were measured several times. The production of  $^7\text{Be}$ ,  $^{22}\text{Na}$  and  $^{24}\text{Na}$  in the thin aluminum targets irradiated by uranium beams of different energies is shown in Figs. 29 – 31.

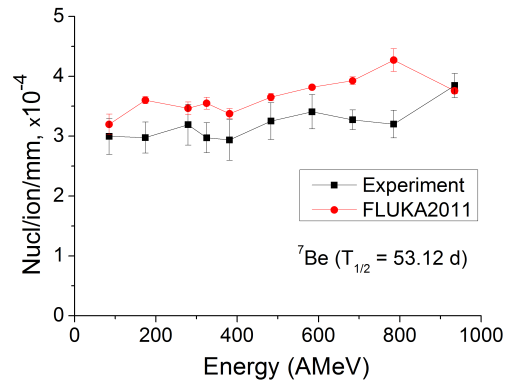


Fig. 29. Production rate of aluminum fragment  ${}^7\text{Be}$  dependence on energy.

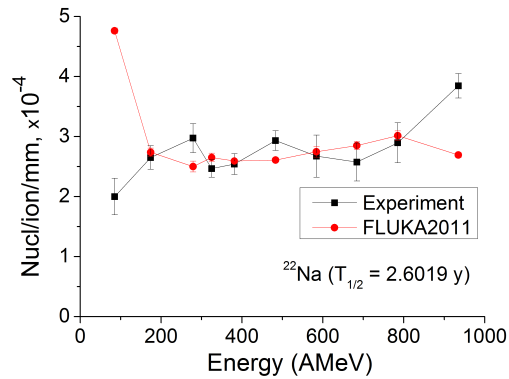


Fig. 30. Production rate of aluminum fragment  ${}^{22}\text{Na}$  dependence on energy.

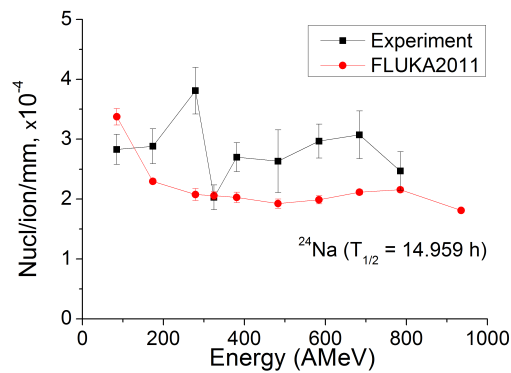


Fig. 31. Production rate of aluminum fragment  ${}^{24}\text{Na}$  dependence on energy.

These data give an overview on the dependence of isotope production on energy. As it can be seen from Fig. 29, on average FLUKA-results for  ${}^7\text{Be}$  agree with the experiment within 5%. The FLUKA-distribution of  ${}^{22}\text{Na}$  (Fig. 30) gives a good agreement with the experiment in the energy range  $150 \text{ AMeV} < E < 800 \text{ AMeV}$ . At 85 AMeV and 935 AMeV the discrepancies are more than a factor 2 and 30%, respectively. In case of  ${}^{24}\text{Na}$  (Fig. 31) the discrepancy is less than 30% for all the energies, but 279 AMeV where the result of simulations is 40% lower than the experimental one. The experimental production rate dependencies on energy reveal irregularities in the behavior, which might be explained by the problems in machine operation and therefore possible errors in measuring the total number of incident ions: bad beam current stabilities at 300 AMeV and at 950 AMeV are shown as an example in Fig. 32. Relatively stable beam currents at 500 AMeV and 700 AMeV are shown as



an example in Fig. 33. The experiment will be repeated to verify the obtained results at more stable beam currents.

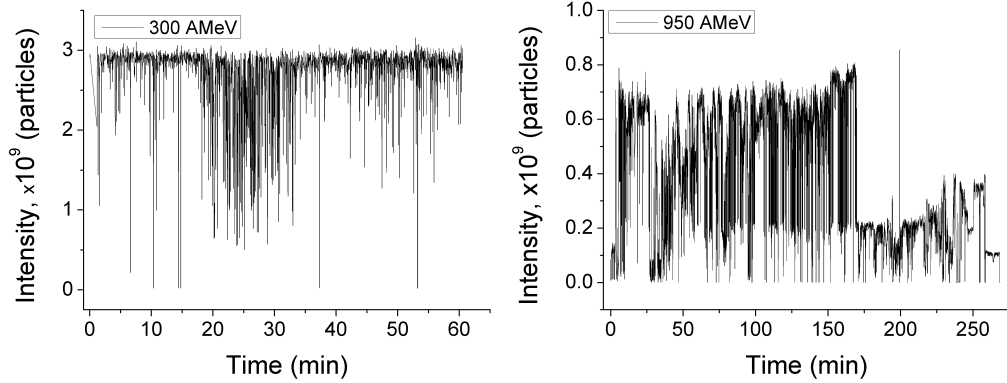


Fig. 32. The beam current variations for the 300 AMeV and 950 AMeV uranium beams irradiating aluminum foils.

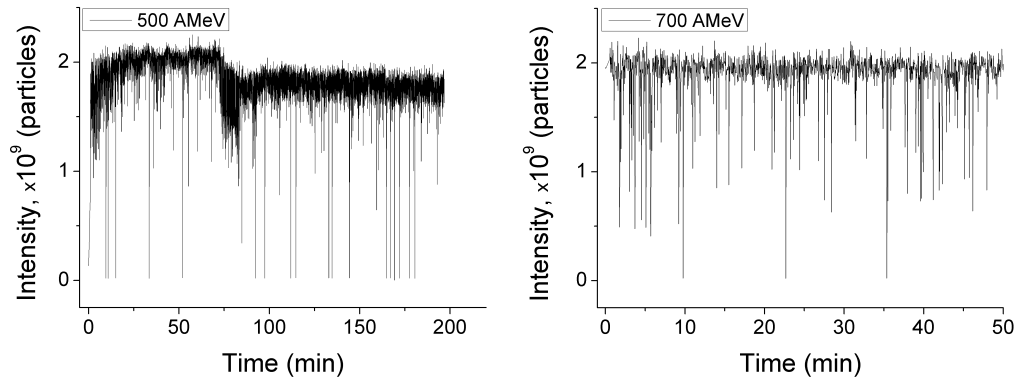


Fig. 33. Examples of a relatively stable uranium beam currents at 500 AMeV and 700 AMeV.

A thick aluminum target was irradiated by a  $^{238}\text{U}$  beam of 483 AMeV for 127 minutes. The total number of the projectiles on the target was  $8.39 \cdot 10^{12} \pm 4.53 \cdot 10^9$  ions, the beam cross-section was Gaussian with FWHM = 2.5 cm. The configuration of the target is shown in Table 13.

Table 13. Configuration of the thick aluminum target (numbers of the foil and its thickness) with diameter  $d = 5$  cm for irradiation by 483 AMeV uranium ions.

Number of the foil	[1]	[2]	[3]	[4]	[5]	[6]	[7]	[8]	[9]
Thickness, mm	0.504	3.61	0.504	2.94	0.505	2.94	0.505	2.493	0.1
Number of the foil	[10]	[11]	[12]	[13]	[14]	[15]	[16]	[17]	[18]
Thickness, mm	0.3	0.1	0.1	0.1	0.1	0.1	0.1	0.1	0.1
Number of the foil	[19]	[20]	[21]	[22]	[23]	[24]	[25]	[26]	
Thickness, mm	0.2	0.1	2.97	0.505	2.97	0.504	3.61	0.505	

### Chapter 3. Experimental results and comparison with the simulations

Gamma-spectra acquisition started approximately 8 days after the irradiation. Spectra acquisition time varied from 1 hour to 7 hours, 250 spectra were measured in total. The measurements were stopped approximately 130 days after the end of irradiation. An example spectrum was shown in Fig. 22.

Seventeen isotopes were identified in the spectra. Just two of them –  $^7\text{Be}$  and  $^{22}\text{Na}$  – are target-like nuclei. The others are the projectile fragments. In case of  $^7\text{Be}$  and  $^{22}\text{Na}$ , their amount at the end of irradiation could be calculated using formula (40). Finding the number of projectile fragments at a certain delay time involves more analysis. Heavy projectile fragments such as  $^{237}\text{U}$ ,  $^{233}\text{Pa}$ ,  $^{230}\text{Pa}$  and  $^{227}\text{Th}$  are produced only directly (see Fig. 34) therefore their number at the end of irradiation could also be calculated using formula (40).

Z	232Pu 33.8 M ε: 90.00% α: 10.00%	233Pu 20.9 M ε: 99.88% α: 0.12%	234Pu 8.8 H ε: 94.00% α: 6.00%	235Pu 25.3 M ε: 100.00% α: 2.8E-3%	236Pu 2.858 Y α: 100.00% SF: 1.9E-7%	237Pu 45.64 D ε: 100.00% α: 4.2E-3%	238Pu 87.7 Y α: 100.00% SF: 1.9E-7%	239Pu 24110 Y α: 100.00% SF: 3.E-10%	240Pu 6561 Y α: 100.00% SF: 5.7E-6%
	93	231Np 48.8 M ε: 98.00% α: 2.00%	232Np 14.7 M ε: 100.00% α: 2.0E-4%	233Np 36.2 M ε: 100.00% α: 1.0E-3%	234Np 4.4 D ε: 100.00%	235Np 396.1 D ε: 100.00% α: 2.6E-3%	236Np 153E+3 Y ε: 86.30% β-: 13.50%	237Np 2.144E+6 Y α: 100.00% SF: 2E-10%	238Np 2.117 D β-: 100.00%
92	230U 20.8 D α: 100.00% SF: < 1E-10%	231U 4.2 D ε: 100.00% α: 4.0E-3%	232U 68.9 Y ε: 100.00% SF: 3E-12%	233U 1.592E+5 Y α: 100.00% 24Ne: 9E-10%	234U 2.455E+5 Y 0.0054% α: 100.00% SF: 1.6E-9%	235U 7.04E+8 Y 0.7204% α: 100.00% SF: 7.0E-9%	236U 2.342E7 Y α: 100.00% SF: 9.4E-8%	237U 6.75 D β-: 100.00%	238U 4.468E9 Y 99.2742% α: 100.00% SF: 5.5E-5%
91	229Pa 1.50 D ε: 99.52% α: 0.48%	230Pa 17.4 D ε: 92.20% β-: 7.80%	231Pa 3.276E+4 Y α: 100.00% SF: 2E-11%	232Pa 1.32 D β-: 100.00% ε	233Pa 26.975 D β-: 100.00%	234Pa 6.70 H β-: 100.00%	235Pa 24.44 M β-: 100.00%	236Pa 9.1 M β-: 100.00%	237Pa 8.7 M β-: 100.00%
90	228Th 1.9116 Y α: 100.00% 200: 1E-11%	229Th 7932 Y α: 100.00%	230Th 7.54E+4 Y α: 100.00% 24Ne: 6E-11%	231Th 25.52 H β-: 100.00% α: 4E-11%	232Th 1.40E10 Y 100% α: 100.00% SF: 1.1E-9%	233Th 21.83 M β-: 100.00%	234Th 24.10 D β-: 100.00%	235Th 7.2 M β-: 100.00%	236Th 37.3 M β-: 100.00%
	138	139	140	141	142	143	144	145	N

Fig. 34. A fragment of the Chart of Nuclides<sup>2</sup> (color code: ■ - EC+β<sup>+</sup>, ■ - β<sup>-</sup>, ■ - α).

The comparison of the simulations and experimentally achieved nuclide distribution depth profiles calculated at the end of irradiation is shown for 483 AMeV

<sup>2</sup> Data Source: *National Nuclear Data Center, Brookhaven National Laboratory*, based on *ENSDF* and the *Nuclear Wallet Cards*.

### 3. 1. Activation of aluminum

uranium ions in Figs. 35 – 40. The integrated depth profiles, i.e. the partial amounts of the nuclides in the whole target volume, are shown in Table 14.

**Table 14. Partial number of deposited isotopes in the whole aluminum target volume ( $l \approx 3$  cm,  $d = 5$  cm) per projectile. The incident beam was 483 AMeV uranium. The numbers are given for zero cooling time.**

Nuclide	Experiment, Nuclides/ion	FLUKA, Nuclides/ion	MARS, Nuclides/ion	SHIELD-A, Nuclides/ion
$^7\text{Be}$	$0.0145 \pm 0.0015$	$0.0164 \pm 0.0003$	$0.0099 \pm 0.0003$	$0.0214 \pm 0.0004$
$^{22}\text{Na}$	$0.0369 \pm 0.0019$	$0.0336 \pm 0.0011$	$0.0404 \pm 0.0016$	$0.1017 \pm 0.0020$
$^{227}\text{Th}$	$(1.297 \pm 0.109) \cdot 10^{-4}$	$(4.656 \pm 0.093) \cdot 10^{-4}$	$(2.667 \pm 0.091) \cdot 10^{-4}$	$(3.007 \pm 0.090) \cdot 10^{-4}$
$^{230}\text{Pa}$	$(1.771 \pm 0.171) \cdot 10^{-4}$	$(3.241 \pm 0.097) \cdot 10^{-4}$	$(2.811 \pm 0.093) \cdot 10^{-4}$	$(4.779 \pm 0.096) \cdot 10^{-4}$
$^{233}\text{Pa}$	$(8.365 \pm 0.995) \cdot 10^{-4}$	$(20.124 \pm 0.612) \cdot 10^{-4}$	$(15.008 \pm 0.603) \cdot 10^{-4}$	$(17.245 \pm 0.511) \cdot 10^{-4}$
$^{237}\text{U}$	$0.01604 \pm 0.00023$	$0.00899 \pm 0.00018$	$0.00796 \pm 0.00018$	$0.0066 \pm 0.00013$

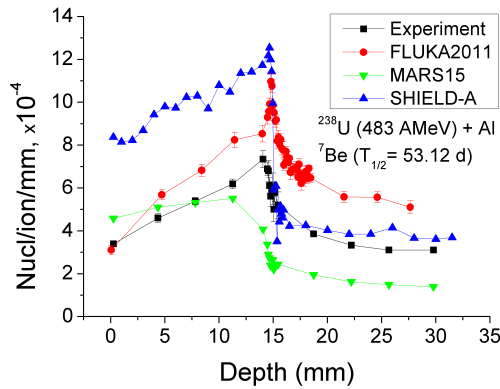


**Fig. 35. The depth profile of  $^7\text{Be}$  in the aluminum target irradiated by a 483 AMeV uranium beam, at zero cooling time.**

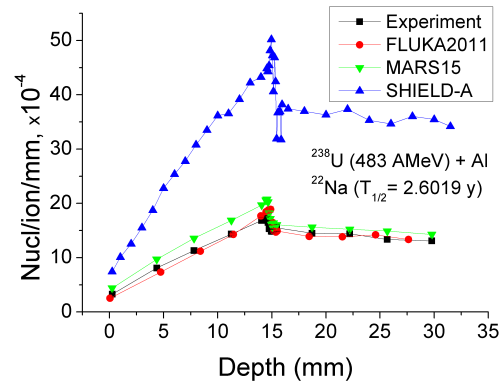


**Fig. 36. The depth profile of  $^{22}\text{Na}$  in the aluminum target irradiated by a 483 AMeV uranium beam, at zero cooling time.**

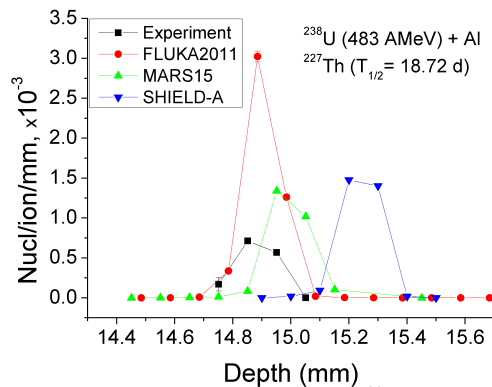


**Fig. 37. The depth profile of  $^{227}\text{Th}$  in the aluminum target irradiated by a 483 AMeV uranium beam, at zero cooling time.**

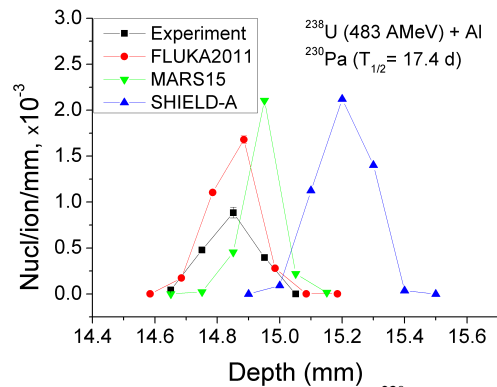


**Fig. 38. The depth profile of  $^{230}\text{Pa}$  in the aluminum target irradiated by a 483 AMeV uranium beam, at zero cooling time.**

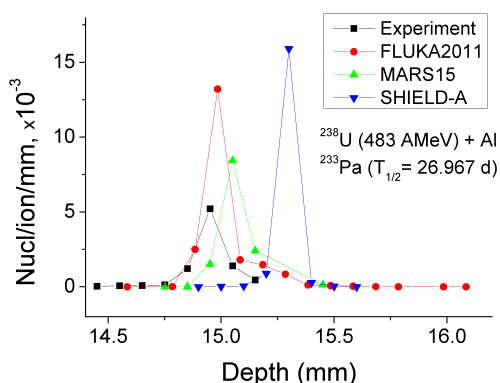


Fig. 39. The depth profile of  $^{233}\text{Pa}$  in the aluminum target irradiated by a 483 AMeV uranium beam, at zero cooling time.

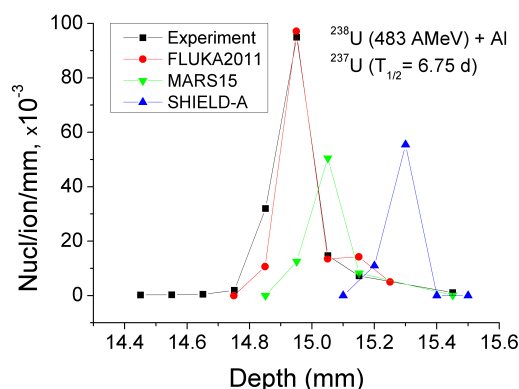


Fig. 40. The depth profile of  $^{237}\text{U}$  in the aluminum target irradiated by a 483 AMeV uranium beam, at zero cooling time.

The shape of the depth profile and the absolute numbers of  $^7\text{Be}$  simulated by FLUKA agree with the experiment within 10% error bars upstream the beam range. At a depth of 15 mm (in the range area) FLUKA shows a maximum which is not observed in the experiment, moreover the amount of  $^7\text{Be}$  downstream the range is overestimated by 50%. The distribution of  $^7\text{Be}$  in the target according to MARS is a step-like function with a 20% higher initial value than the experimental one (the number of nuclei deposited in the first disc). The SHIELD-results for  $^7\text{Be}$  agree with the experiment in shape, however, the absolute values deviate by about factor 2 upstream the beam stopping range, but downstream the agreement with the experiment lies within 10%.

The shape of the  $^{22}\text{Na}$  depth profile is reproduced by all three codes. Talking about absolute numbers of  $^{22}\text{Na}$  nuclei, FLUKA reproduces them within 10% error bars, MARS has ~30% discrepancy, while SHIELD gives at least 2 times higher results.

For heavy projectile fragments, the position of the maximum is reproduced within error bars when calculated using FLUKA, MARS and SHIELD. It should be mentioned that even though the shift of the maximum in SHIELD calculations (Figures 37 – 40) looks significant, in fact it is less than 3% compared to the experimental result. The absolute values for the numbers of  $^{227}\text{Th}$ ,  $^{230}\text{Pa}$  and  $^{233}\text{Pa}$  are

overestimated by FLUKA, MARS and SHIELD by more than 50%. FLUKA results for  $^{237}\text{U}$  agree with the experiment, whereas SHIELD and MARS underestimate its amount by 40%. For calculating the amount of  $^{237}\text{U}$  it is important to take into account that it could be produced in the processes of electromagnetic dissociation. This option was used in FLUKA simulations, however switching it on in SHIELD and MARS dramatically increases the time of calculation, therefore it was not used.

The other projectile fragments  $^{206}\text{Po}$ ,  $^{205}\text{Bi}$ ,  $^{202}\text{Tl}$ ,  $^{188}\text{Pt}$ ,  $^{185}\text{Os}$ ,  $^{169}\text{Yb}$ ,  $^{149}\text{Gd}$ ,  $^{141}\text{Ce}$ ,  $^{127}\text{Xe}$ ,  $^{99}\text{Mo}$ ,  $^{83}\text{Rb}$  are produced not only in direct reactions but also through decays of other radioactive nuclei or through isomeric transitions. Figure 41 shows a fragment of the chart of nuclides which illustrates the modes of radioactive decay. For example, the isotope  $^{206}\text{Po}$  can be produced through  $\alpha$ -decay of  $^{210}\text{Rn}$  or through  $\beta$ -decay of  $^{206}\text{At}$ . An indicator of production through decay chains is the  $^{206}\text{Po}$ -activity dependence on time. In such cases when relatively long-lived nucleus is produced through radioactive decays of the parent nuclei having shorter half-life, its amount is first increased, and after the parent nuclei decay, the decrease of the activity of daughter product can be observed.

The spectra acquisition started 8 days after the end of irradiation in present experiment. No increase in the intensity of the mentioned isotopes was revealed. However respective FLUKA-simulations showed that the increase of the activity of several isotopes is indeed present shortly after the end of irradiation. Figures 42 – 43 show the results of the simulations for activity dependence on time for different isotopes.

It was possible in this experiment to find the numbers of radioactive isotopes, after their production through all the competitive processes was finished, i.e. at a delay time of 1 week. This was done using formulae (39) and (40). The FLUKA-simulations were done respectively. It should be underlined that in this case the duration of the irradiation plays an important role because during the irradiation the decay of the short-lived nuclei also happens and could significantly influence the final results.

The results of the experiment and FLUKA-calculations are presented in Figs. 44 –

## Chapter 3. Experimental results and comparison with the simulations

54, the integrals over the whole target volume are given in Table 15.

Z	203Rn 44 S	204Rn 74.5 S	205Rn 170 S	206Rn 5.67 M	207Rn 9.25 M	208Rn 24.35 M	209Rn 28.5 M	210Rn 2.4 H	211Rn 14.6 H
	$\epsilon$ : 66.00% $\alpha$ : 34.00%	$\epsilon$ : 72.40% $\epsilon$ : 27.60%	$\epsilon$ : 75.40% $\alpha$ : 24.60%	$\alpha$ : 62.00% $\epsilon$ : 38.00%	$\epsilon$ : 79.00% $\alpha$ : 21.00%	$\alpha$ : 62.00% $\epsilon$ : 38.00%	$\epsilon$ : 83.00% $\alpha$ : 17.00%	$\alpha$ : 96.00% $\epsilon$ : 4.00%	$\epsilon$ : 72.60% $\alpha$ : 27.40%
	202At 184 S	203At 7.4 M	204At 9.12 M	205At 26.9 M	206At 30.6 M	207At 1.81 H	208At 1.63 H	209At 5.41 H	210At 8.1 H
	$\epsilon$ : 63.00% $\alpha$ : 37.00%	$\epsilon$ : 69.00% $\alpha$ : 31.00%	$\epsilon$ : 96.09% $\alpha$ : 3.91%	$\epsilon$ : 90.00% $\alpha$ : 10.00%	$\epsilon$ : 99.10% $\alpha$ : 0.90%	$\epsilon$ : 91.40% $\alpha$ : 8.60%	$\epsilon$ : 99.45% $\alpha$ : 0.55%	$\epsilon$ : 95.90% $\alpha$ : 4.10%	$\epsilon$ : 99.82% $\alpha$ : 0.18%
	201Po 15.6 M	202Po 44.6 M	203Po 36.7 M	204Po 3.519 H	205Po 1.74 H	206Po 8.8 D	207Po 5.80 H	208Po 2.896 Y	209Po 102 Y
	$\epsilon$ : 98.87% $\alpha$ : 1.13%	$\epsilon$ : 98.06% $\alpha$ : 1.92%	$\epsilon$ : 99.89% $\alpha$ : 0.11%	$\epsilon$ : 99.33% $\alpha$ : 0.67%	$\epsilon$ : 99.96% $\alpha$ : 0.04%	$\epsilon$ : 94.55% $\alpha$ : 5.45%	$\epsilon$ : 99.98% $\alpha$ : 0.02%	$\alpha$ : 100.00% $\epsilon$ : 4.0E-5%	$\alpha$ : 99.52% $\epsilon$ : 0.48%
	200Bi 36.4 M	201Bi 103 M	202Bi 1.71 H	203Bi 11.76 H	204Bi 11.22 H	205Bi 15.31 D	206Bi 6.243 D	207Bi 31.55 Y	208Bi 3.68E+5 Y
	$\epsilon$ : 100.00%	$\epsilon$ : 100.00%	$\epsilon$ : 100.00%	$\epsilon$ : 100.00%	$\epsilon$ : 100.00%	$\epsilon$ : 100.00%	$\epsilon$ : 100.00%	$\epsilon$ : 100.00%	$\epsilon$ : 100.00%
199Pb 90 M	200Pb 21.5 H	201Pb 9.33 H	202Pb 52.5E+3 Y 3.54 H IT: 90.5% $\epsilon$ : 9.5%	203Pb 51.92 H	204Pb $\geq 1.4E+17$ Y 1.4% $\alpha$	205Pb 1.73E+7 Y	206Pb STABLE 24.1%	207Pb STABLE 22.1%	
$\epsilon$ : 100.00%	$\epsilon$ : 100.00%	$\epsilon$ : 100.00%	$\epsilon$ : 100.00%	$\epsilon$ : 100.00%	$\epsilon$ : 100.00%	$\epsilon$ : 100.00%			
198Tl 5.3 H	199Tl 7.42 H	200Tl 26.1 H	201Tl 3.0421 D	202Tl 12.31 D	203Tl STABLE 29.524%	204Tl 3.783 Y	205Tl STABLE 70.48%	206Tl 4.202 M	
$\epsilon$ : 100.00%	$\epsilon$ : 100.00%	$\epsilon$ : 100.00%	$\epsilon$ : 100.00%	$\epsilon$ : 100.00%		$\beta^-$ : 97.08% $\epsilon$ : 2.92%		$\beta^-$ : 100.00%	
197Hg 64.14 H	198Hg STABLE 9.97%	199Hg STABLE 16.87%	200Hg STABLE 23.10%	201Hg STABLE 13.18%	202Hg STABLE 29.86%	203Hg 46.594 D	204Hg STABLE 6.87%	205Hg 5.14 M	
$\epsilon$ : 100.00%						$\beta^-$ : 100.00%		$\beta^-$ : 100.00%	
	117	118	119	120	121	122	123	124	N

Fig. 41. A fragment of the Chart of Nuclides<sup>3</sup> (color code: ■ - EC+ $\beta^+$ , ■ -  $\beta^-$ , ■ -  $\alpha$ ).

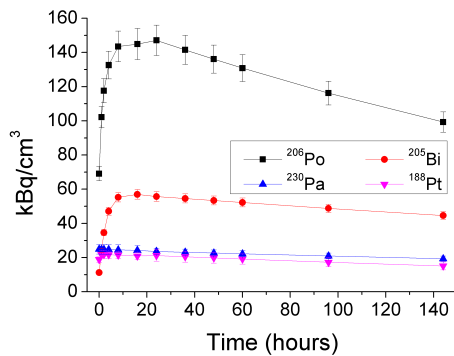


Fig. 42. FLUKA-simulations of the activity dependence on time.

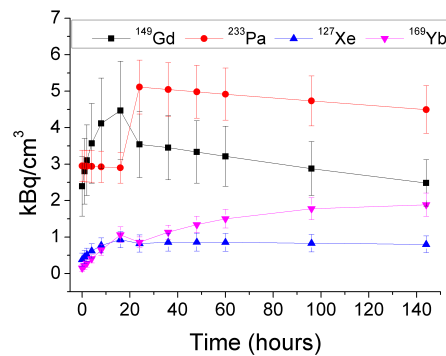


Fig. 43. FLUKA-simulations of the activity dependence on time.

<sup>3</sup> Data Source: *National Nuclear Data Center, Brookhaven National Laboratory*, based on *ENSDF* and the *Nuclear Wallet Cards*

### 3. 1. Activation of aluminum

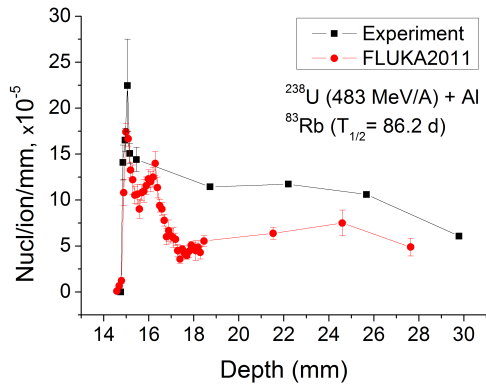


Fig. 44. The depth profile of  $^{83}\text{Rb}$  in the aluminum target irradiated by a 483 AMeV uranium beam, after 7 days of cooling.

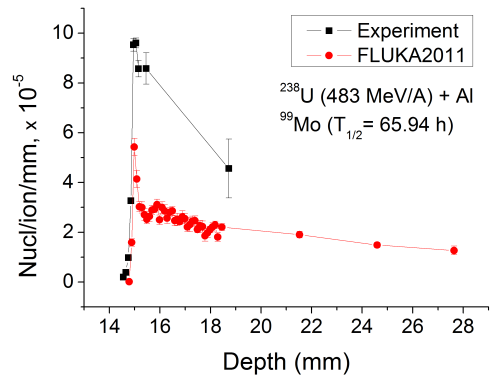


Fig. 45. The depth profile of  $^{99}\text{Mo}$  in the aluminum target irradiated by a 483 AMeV uranium beam, after 7 days of cooling.

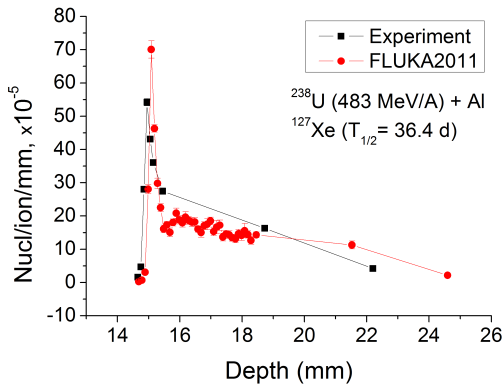


Fig. 46. The depth profile of  $^{127}\text{Xe}$  in the aluminum target irradiated by a 483 AMeV uranium beam, after 7 days of cooling.

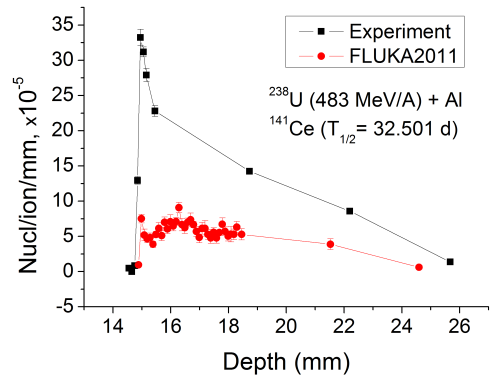


Fig. 47. The depth profile of  $^{141}\text{Ce}$  in the aluminum target irradiated by a 483 AMeV uranium beam, after 7 days of cooling.

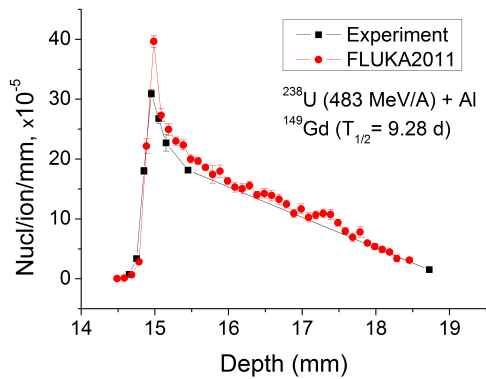


Fig. 48. The depth profile of  $^{149}\text{Gd}$  in the aluminum target irradiated by a 483 AMeV uranium beam, after 7 days of cooling.

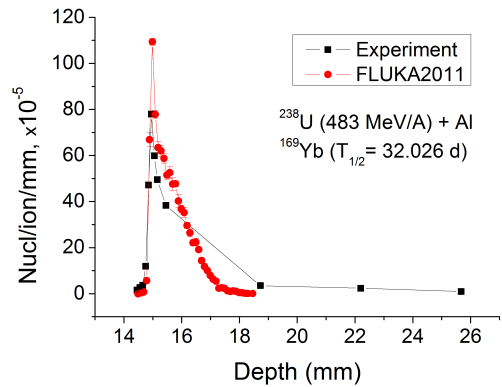


Fig. 49. The depth profile of  $^{169}\text{Yb}$  in the aluminum target irradiated by a 483 AMeV uranium beam, after 7 days of cooling.

### Chapter 3. Experimental results and comparison with the simulations

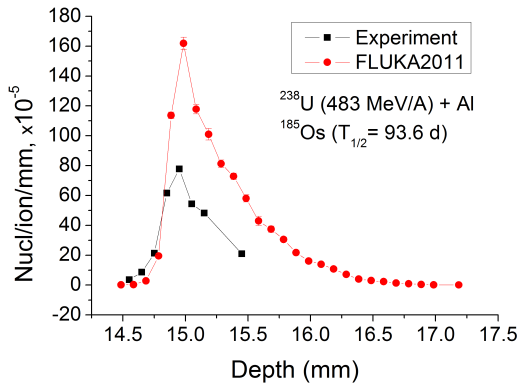


Fig. 50. The depth profile of  $^{185}\text{Os}$  in the aluminum target irradiated by a 483 AMeV uranium beam, after 7 days of cooling.

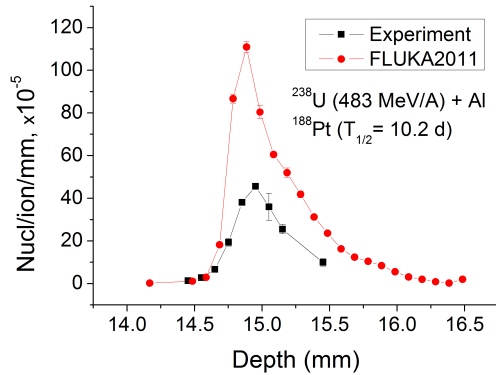


Fig. 51. The depth profile of  $^{188}\text{Pt}$  in the aluminum target irradiated by a 483 AMeV uranium beam, after 7 days of cooling.

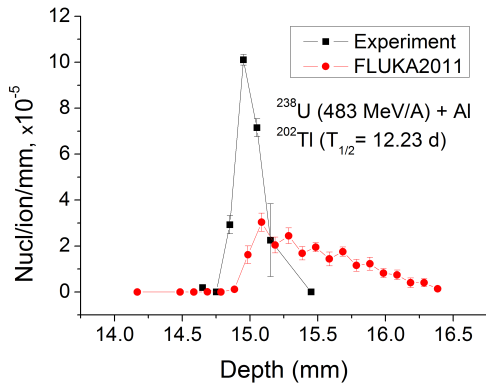


Fig. 52. The depth profile of  $^{202}\text{Tl}$  in the aluminum target irradiated by a 483 AMeV uranium beam, after 7 days of cooling.

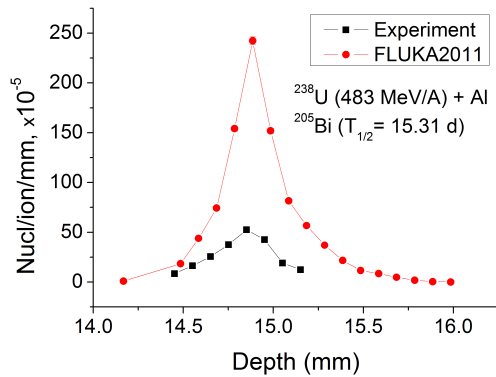


Fig. 53. The depth profile of  $^{205}\text{Bi}$  in the aluminum target irradiated by a 483 AMeV uranium beam, after 7 days of cooling.

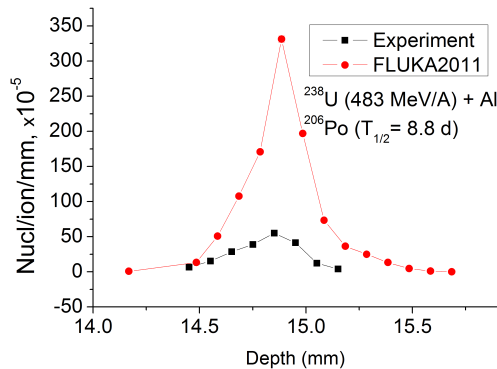


Fig. 54. The depth profile of  $^{206}\text{Po}$  in the aluminum target irradiated by a 483 AMeV uranium beam, after 7 days of cooling.



**Table 15. Partial number of deposited isotopes (produced through decay chains as well as in direct reactions) in the whole target volume per projectile. The numbers are given 7 days after the end of aluminum target irradiation by a 483 AMeV uranium beam.**

Nuclide	Half-life $T_{1/2}$ , days	Decay mode	Energy of the most intense $\gamma$ - line (keV)	Experiment, Nuclides/ion	FLUKA, Nuclides/ion
<sup>83</sup> Rb	86.2	$\epsilon^4$	529.635	$(16.629 \pm 1.650) \cdot 10^{-4}$	$(8.946 \pm 0.268) \cdot 10^{-4}$
<sup>99</sup> Mo	2.7475	$\beta^-$	140.511	$(2.690 \pm 0.321) \cdot 10^{-4}$	$(2.512 \pm 0.051) \cdot 10^{-4}$
<sup>127</sup> Xe	36.4	$\epsilon$	202.860	$(1.317 \pm 0.083) \cdot 10^{-3}$	$(1.291 \pm 0.039) \cdot 10^{-3}$
<sup>141</sup> Ce	32.501	$\beta^-$	145.4405	$(13.441 \pm 0.342) \cdot 10^{-4}$	$(4.193 \pm 0.106) \cdot 10^{-4}$
<sup>149</sup> Gd	9.28	$\epsilon + \beta^+, \alpha$	149.735	$(4.741 \pm 0.252) \cdot 10^{-4}$	$(5.124 \pm 0.154) \cdot 10^{-4}$
<sup>169</sup> Yb	32.026	$\epsilon$	63.12077	$(12.073 \pm 0.471) \cdot 10^{-4}$	$(9.464 \pm 0.243) \cdot 10^{-4}$
<sup>185</sup> Os	93.6	$\epsilon$	646.116	$(3.535 \pm 0.396) \cdot 10^{-4}$	$(9.227 \pm 0.277) \cdot 10^{-4}$
<sup>188</sup> Pt	10.2	$\epsilon, \alpha$	187.59	$(2.152 \pm 0.290) \cdot 10^{-4}$	$(5.716 \pm 0.143) \cdot 10^{-4}$
<sup>202</sup> Tl	12.23	$\epsilon + \beta^+$	439.56	$(2.479 \pm 0.422) \cdot 10^{-5}$	$(2.092 \pm 0.064) \cdot 10^{-5}$
<sup>205</sup> Bi	15.31	$\epsilon + \beta^+$	1764.36	$(2.044 \pm 0.253) \cdot 10^{-4}$	$(9.311 \pm 0.233) \cdot 10^{-4}$
<sup>206</sup> Po	8.8	$\epsilon + \beta^+, \alpha$	1032.26	$(1.969 \pm 0.048) \cdot 10^{-4}$	$(10.407 \pm 0.267) \cdot 10^{-4}$

There is no uniform dependence of the accuracy of FLUKA predictions on the mass number of the reaction product. The total amounts of <sup>185</sup>Os, <sup>188</sup>Pt, <sup>205</sup>Bi and <sup>206</sup>Po are overestimated by factors 2 to 5. The amounts of <sup>83</sup>Rb, <sup>99</sup>Mo, <sup>141</sup>Ce, <sup>202</sup>Tl are underestimated by factors 2 to 4. The amounts of <sup>149</sup>Gd and <sup>169</sup>Yb agree with the experiment.

### 3.2. Activation of copper

Targets of natural copper (Abundance: <sup>63</sup>Cu - 69.17%, <sup>65</sup>Cu - 30.83%) were irradiated by nitrogen and argon beams.

#### 3.2.1. Activation of copper by nitrogen

A thick copper target was irradiated by a nitrogen beam of 498 AMeV for 36 minutes. The total number of projectiles on the target was  $3.03 \cdot 10^{13} \pm 2.78 \cdot 10^{10}$  particles. The beam cross-section was circular with the diameter  $d = 3$  cm. The configuration of the target is presented in Table 16.

---

<sup>4</sup>  $\epsilon$  – electron capture

### Chapter 3. Experimental results and comparison with the simulations

---

Gamma-spectra acquisition started approximately half a year after the irradiation, 69 spectra were measured and analyzed in total.

**Table 16. Configuration of the thick copper target irradiated by 498 AMeV nitrogen beam.**

Disc number	[1]	[2]	[3]	[4]	[5]	[6]	[7]
Disc thickness, mm	0.5	20.02	0.449	20.027	0.449	10.004	0.449
Disc number	[8]	[9]	[10]	[11]	[12]	[13]	[14]
Disc thickness, mm	0.5	0.5	0.449	0.5	0.449	0.5	0.449
Disc number	[15]	[16]	[17]	[18]	[19]	[20]	[21]
Disc thickness, mm	0.5	0.5	9.965	0.449	19.806	0.5	20.035
Disc number	[22]						
Disc thickness, mm	0.5						

All but three nuclides are produced directly through fragmentation of copper nuclei. Their depth profiles at zero cooling time are shown in Figs. 55 – 62.

Three isotopes  $^{46}\text{Sc}$ ,  $^{58}\text{Co}$  and  $^{60}\text{Co}$  are produced in ground and isomeric states. All three isomers are too short-lived for being registered in this experiment. However the decay of the isomeric state increases the number of respective isotopes in the ground state, this could give additional discrepancies in comparing the experimental and calculated results. Depth profiles of these three nuclides calculated at a cooling time 7 days after the irradiation are presented in Figs. 63 – 65 together with respective FLUKA-simulations.

### 3.2. Activation of copper

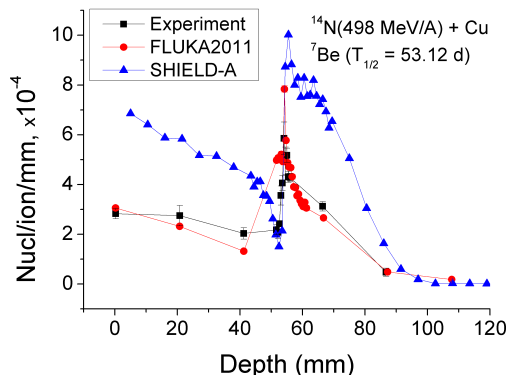


Fig. 55. The depth profile of  ${}^7\text{Be}$  in the copper target irradiated by a 498 AMeV nitrogen beam, at zero cooling time.

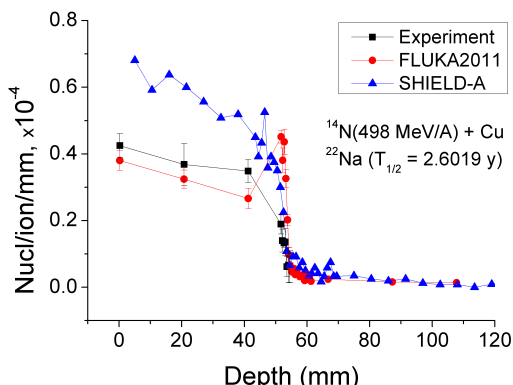


Fig. 56. The depth profile of  ${}^{22}\text{Na}$  in the copper target irradiated by a 498 AMeV nitrogen beam, at zero cooling time.

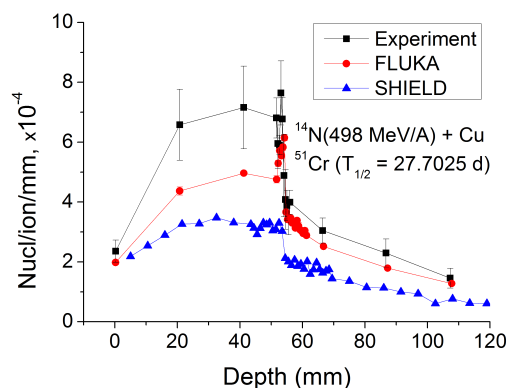


Fig. 57. The depth profile of  ${}^{51}\text{Cr}$  in the copper target irradiated by a 498 AMeV nitrogen beam, at zero cooling time.

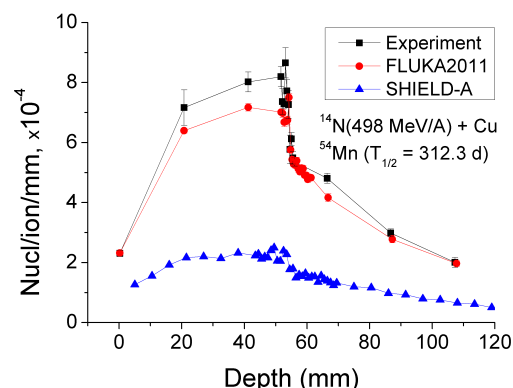


Fig. 58. The depth profile of  ${}^{54}\text{Mn}$  in the copper target irradiated by a 498 AMeV nitrogen beam, at zero cooling time.

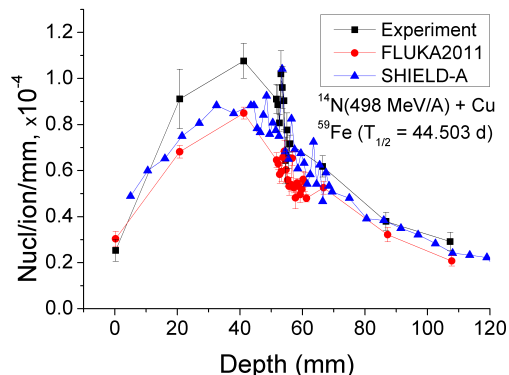


Fig. 59. The depth profile of  ${}^{59}\text{Fe}$  in the copper target irradiated by a 498 AMeV nitrogen beam, at zero cooling time.

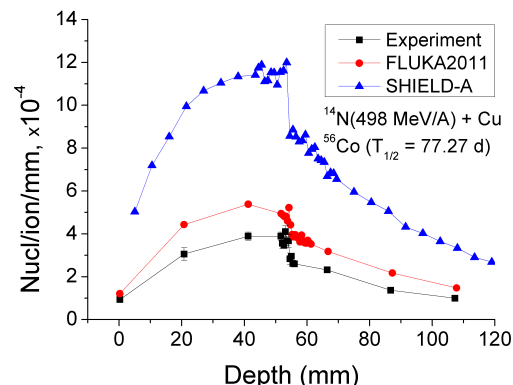


Fig. 60. The depth profile of  ${}^{56}\text{Co}$  in the copper target irradiated by a 498 AMeV nitrogen beam, at zero cooling time.

### Chapter 3. Experimental results and comparison with the simulations

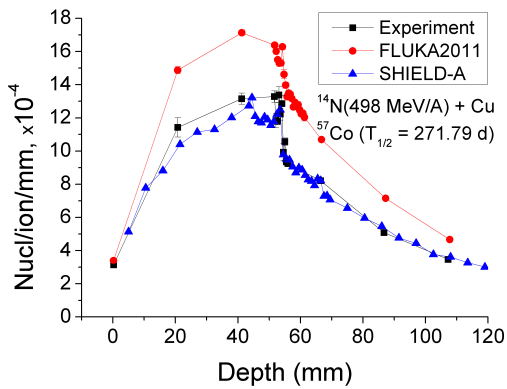


Fig. 61. The depth profile of  $^{57}\text{Co}$  in the copper target irradiated by a 498 AMeV nitrogen beam, at zero cooling time.

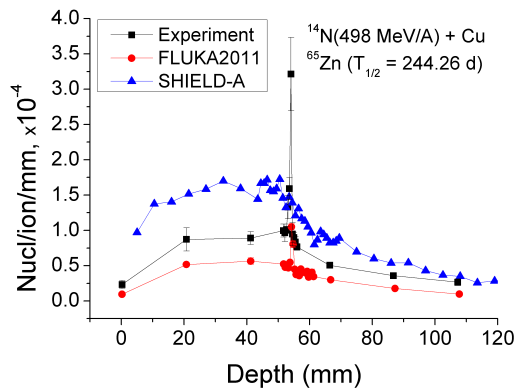


Fig. 62. The depth profile of  $^{65}\text{Zn}$  in the copper target irradiated by a 498 AMeV nitrogen beam, at zero cooling time.

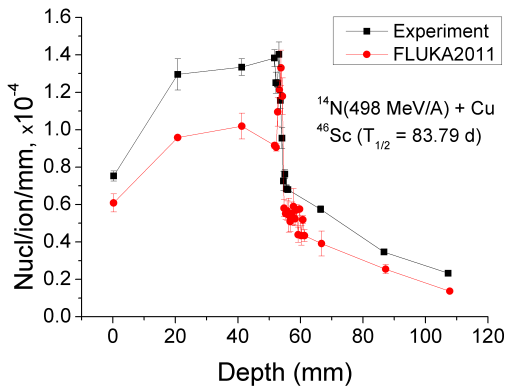


Fig. 63. The depth profile of  $^{46}\text{Sc}$  in the copper target irradiated by a 498 AMeV nitrogen beam, after 7 days of cooling.

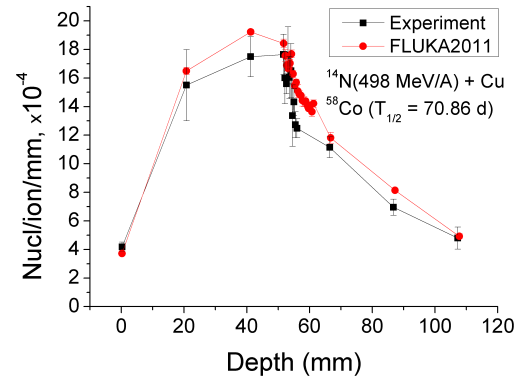


Fig. 64. The depth profile of  $^{58}\text{Co}$  in the copper target irradiated by a 498 AMeV nitrogen beam, after 7 days of cooling.

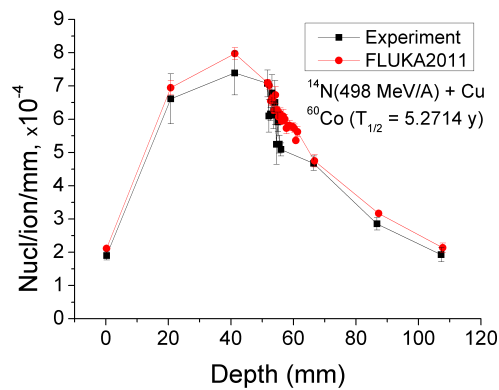


Fig. 65. The depth profile of  $^{60}\text{Co}$  in the copper target irradiated by a 498 AMeV nitrogen beam, after 7 days of cooling.

### 3. 2. Activation of copper

Partial numbers for each nuclide deposited in the target per incident ion are given in Tables 17 and 18 at the end of irradiation and at 7 days delay time, respectively.

**Table 17. Partial number of deposited isotopes in the whole copper target (l = 11 cm, d = 5 cm) at the end of irradiation. The incident beam was a 498 AMeV nitrogen.**

Nuclide	Half-life $T_{1/2}$ , days	Decay mode	Energy of the most intense $\gamma$ - line (keV)	Experiment, Nucl/ion	FLUKA, Nucl/ion	SHIELD, Nucl/ion
<sup>7</sup> Be	53.12	$\epsilon$	477.595	$0.0220 \pm 0.0022$	$0.0220 \pm 0.0009$	$0.0444 \pm 0.0027$
<sup>22</sup> Na	950.324	$\epsilon + \beta^+$	1274.53	$(1.861 \pm 0.245) \cdot 10^{-3}$	$(1.897 \pm 0.180) \cdot 10^{-3}$	$(2.803 \pm 0.065) \cdot 10^{-3}$
<sup>51</sup> Cr	27.7025	$\epsilon$	320.0824	$0.0458 \pm 0.078$	$0.0340 \pm 0.0008$	$0.0240 \pm 0.0008$
<sup>54</sup> Mn	312.3	$\epsilon + \beta^+, \beta^-$	834.848	$0.0551 \pm 0.0029$	$0.0501 \pm 0.012$	$0.0180 \pm 0.0011$
<sup>59</sup> Fe	44.503	$\beta^-$	1099.251	$(7.022 \pm 0.709) \cdot 10^{-3}$	$(5.595 \pm 0.308) \cdot 10^{-3}$	$(6.832 \pm 0.906) \cdot 10^{-3}$
<sup>56</sup> Co	77.27	$\epsilon + \beta^+$	846.771	$0.0255 \pm 0.0016$	$0.0363 \pm 0.0008$	$0.0886 \pm 0.0053$
<sup>57</sup> Co	271.79	$\epsilon$	122.0614	$0.0902 \pm 0.0030$	$0.1189 \pm 0.0016$	$0.0948 \pm 0.0056$
<sup>65</sup> Zn	244.26	$\epsilon + \beta^+$	1115.546	$(6.660 \pm 0.884) \cdot 10^{-3}$	$(3.706 \pm 0.274) \cdot 10^{-3}$	$0.0119 \pm 0.0007$

**Table 18. Partial number of deposited isotopes at 7 days cooling time in the whole target volume of the copper target (l = 11 cm, d = 5 cm) irradiated by a 498 AMeV nitrogen beam.**

Nuclide	Half-life $T_{1/2}$ , days	Decay mode	Energy of the most intense $\gamma$ -line (keV)	Experiment, Nucl/ion	FLUKA, Nucl/ion
<sup>46</sup> Sc	83.79	$\beta^-$	1120.545	$(8.836 \pm 0.393) \cdot 10^{-3}$	$(6.606 \pm 0.389) \cdot 10^{-3}$
<sup>58</sup> Co	70.86	$\epsilon + \beta^+$	810.775	$0.1216 \pm 0.0124$	$0.1327 \pm 0.0023$
<sup>60</sup> Co	1925.338	$\beta^-$	1332.501	$0.0509 \pm 0.0042$	$0.055 \pm 0.015$

Depth profile of <sup>7</sup>Be obtained using FLUKA agrees with the experiment within 10% upstream and downstream the beam stopping range, and in the range area the deviation from the height of the maximum lies within 30%. In SHIELD simulations upstream the range the curve decreases (the amount of <sup>7</sup>Be in the first disc is 2.5 times overestimated) and right after the range it gives an increase – a wide maximum of the distribution – and then decreases again. A similar increase is observed in the experiment, but it is 2 times less.

FLUKA gives an increase of the amount of <sup>22</sup>Na nuclides along the range of the nitrogen beam in copper target which is not observed in the experiment; otherwise the FLUKA depth profile agrees with this experimental one within 10%. The <sup>22</sup>Na curve as simulated using SHIELD is overestimated by 50% upstream the range and agrees with the experiment downstream the range.

## Chapter 3. Experimental results and comparison with the simulations

The simulated depth profiles of heavy isotopes:  $^{60}\text{Co}$ ,  $^{58}\text{Co}$ ,  $^{57}\text{Co}$ ,  $^{56}\text{Co}$  are similar to the experimental ones in shape, however the absolute values are not always accurate. In case of  $^{60}\text{Co}$  and  $^{58}\text{Co}$  FLUKA agrees with the experiment. For  $^{57}\text{Co}$  FLUKA gives higher values, while SHIELD gives an agreement with the experiment. The amount of  $^{56}\text{Co}$  is overestimated by 40 % in case of FLUKA and more than 2 times by SHIELD. The numbers of such nuclides as  $^{65}\text{Zn}$  and  $^{54}\text{Mn}$  are described by SHIELD with more than 70% discrepancy. Besides, the shape of the nuclide distribution is not reproduced. In case of  $^{65}\text{Zn}$  there is a maximum in the range area which is given by FLUKA, but seriously underestimated comparing to experimental results. FLUKA results for  $^{54}\text{Mn}$  agree within the error bars and underestimate the  $^{46}\text{Sc}$  production by 15%. In case of  $^{51}\text{Cr}$  FLUKA and SHIELD underestimate its amount by ~30% and ~50%, respectively. The amount of  $^{59}\text{Fe}$  downstream the range is calculated with a good precision both by FLUKA and SHIELD, upstream the range FLUKA results are underestimating by 20 %.

### 3.2.2. Activation of copper by argon

The configuration of the thick copper target irradiated by a 496 AMeV argon  $^{40}\text{Ar}^{18+}$  beam for 913 sec with  $1.01 \cdot 10^{13} \pm 1.91 \cdot 10^{10}$  projectiles is given in Table 19.

**Table 19. Configuration of the thick copper target irradiated by a 496 AMeV argon beam.**

Disc number	[1]	[2]	[3]	[4]	[5]	[6]	[7]
Disc thickness, mm	1.008	7.002	1.006	7.002	0.992	1.988	0.499
Disc number	[8]	[9]	[10]	[11]	[12]	[13]	[14]
Disc thickness, mm	1.991	0.994	1.997	0.499	1.996	0.994	1.99
Disc number	[15]	[16]	[17]	[18]	[19]	[20]	[21]
Disc thickness, mm	0.499	1.984	0.993	1.993	0.499	1.99	0.994
Disc number	[22]	[23]	[24]	[25]	[26]	[27]	
Disc thickness, mm	1.99	0.499	1.984	0.994	2	0.5	

The measurements of the  $\gamma$ -spectra started 3 months after the irradiation. Eighty two spectra were measured and analyzed in total. The dependences of the number of nuclides on depth produced directly through fragmentation of copper are shown in Figs. 66 – 74 at the end of the irradiation together with FLUKA and SHIELD calculations.

### 3. 2. Activation of copper

Depth profiles of  $^{46}\text{Sc}$ ,  $^{58}\text{Co}$  and  $^{60}\text{Co}$  are given in Figs. 75 – 77 seven days after the end of the irradiation, because these isotopes are produced through isomer transition, as was discussed in previous section.

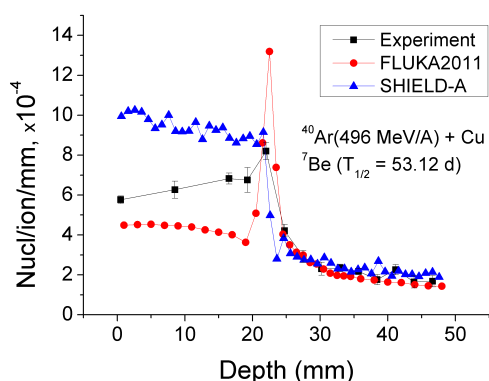


Fig. 66. The depth profile of  $^7\text{Be}$  in a copper target irradiated by 496 AMeV argon ions, at zero cooling time.

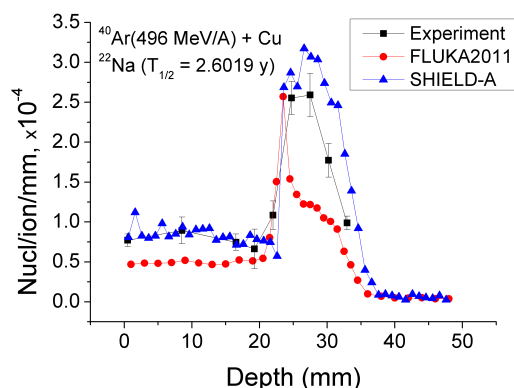


Fig. 67. The depth profile of  $^{22}\text{Na}$  in a copper target irradiated by 496 AMeV argon ions, at zero cooling time.

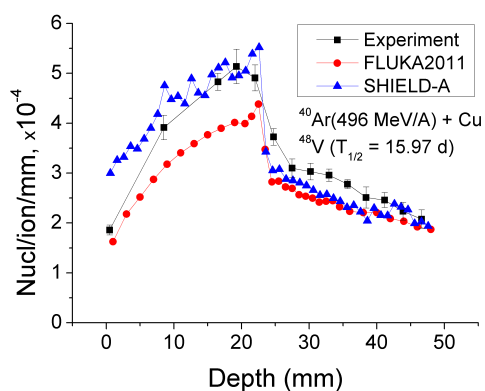


Fig. 68. The depth profile of  $^{48}\text{V}$  in a copper target irradiated by 496 AMeV argon ions, at zero cooling time.

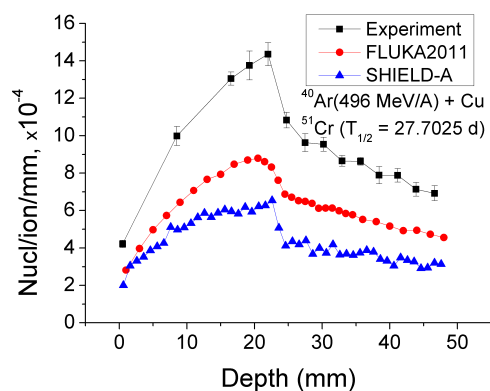


Fig. 69. The depth profile of  $^{51}\text{Cr}$  in a copper target irradiated by 496 AMeV argon ions, at zero cooling time.

### Chapter 3. Experimental results and comparison with the simulations

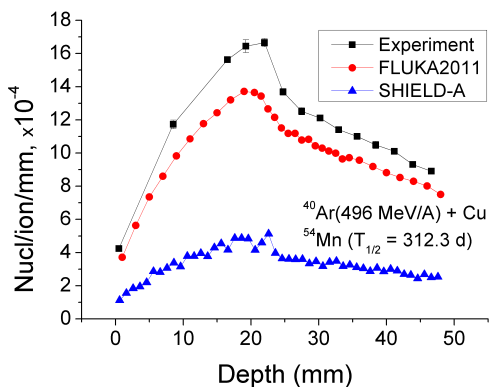


Fig. 70. The depth profile of  $^{54}\text{Mn}$  in a copper target irradiated by 496 AMeV argon ions, at zero cooling time.

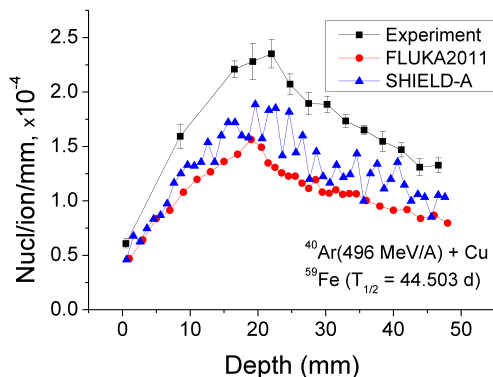


Fig. 71. The depth profile of  $^{59}\text{Fe}$  in a copper target irradiated by 496 AMeV argon ions, at zero cooling time.

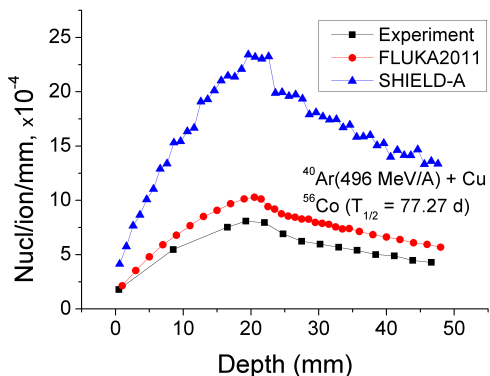


Fig. 72. The depth profile of  $^{56}\text{Co}$  in a copper target irradiated by 496 AMeV argon ions, at zero cooling time.

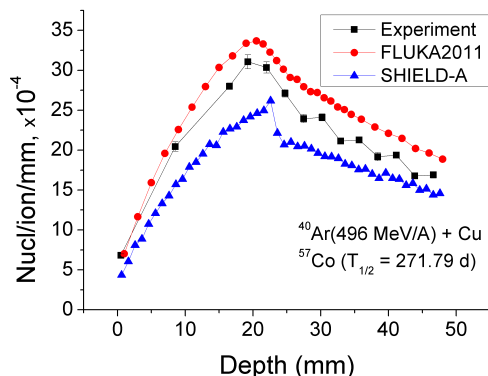


Fig. 73. The depth profile of  $^{57}\text{Co}$  in a copper target irradiated by 496 AMeV argon ions, at zero cooling time.

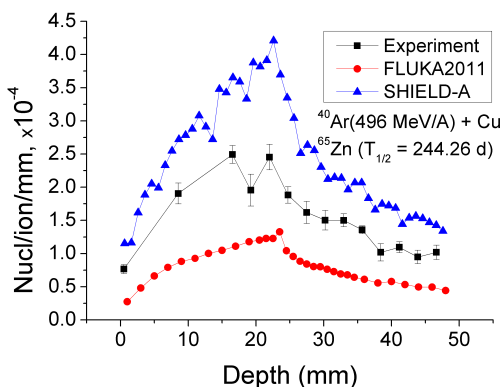


Fig. 74. The depth profile of  $^{65}\text{Zn}$  in a copper target irradiated by 496 AMeV argon ions, at zero cooling time.

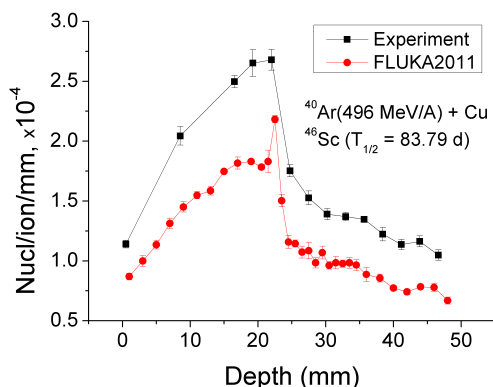


Fig. 75. The depth profile of  $^{46}\text{Sc}$  in a copper target irradiated by 496 AMeV argon ions, after 7 days of cooling.



### 3. 2. Activation of copper

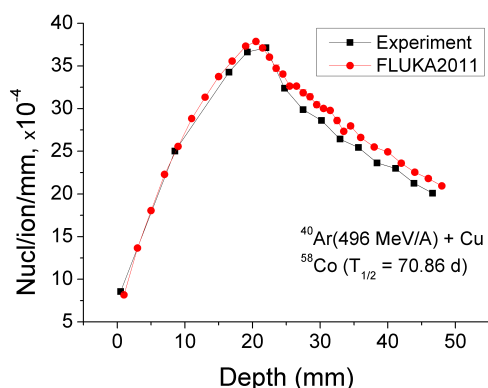


Fig. 76. The depth profile of  $^{58}\text{Co}$  in a copper target irradiated by 496 AMeV argon ions, after 7 days of cooling.

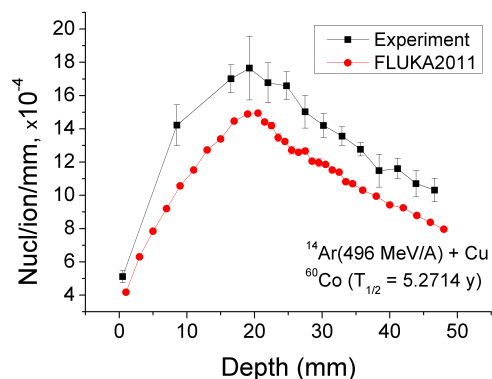


Fig. 77. The depth profile of  $^{60}\text{Co}$  in a copper target irradiated by 496 AMeV argon ions, after 7 days of cooling.

Total numbers of each isotope produced and deposited in the whole target are shown in Table 20 and Table 21 per primary projectile.

Table 20. Partial number of the nuclides in the whole copper target irradiated by 496 AMeV argon beam (at the end of irradiation).

Nuclide	Half-life $T_{1/2}$ , d	Decay mode	Energy of the most intense $\gamma$ -line (keV)	Experiment, Nucl/ion	FLUKA, Nucl/ion	SHIELD-A, Nucl/ion
$^7\text{Be}$	53.12	$\epsilon$	477.595	$0.0207 \pm 0.0015$	$0.0166 \pm 0.0002$	$0.0266 \pm 0.0016$
$^{22}\text{Na}$	950.324	$\epsilon + \beta^+$	1274.53	$0.0039 \pm 0.0005$	$0.0026 \pm 0.0001$	$0.0049 \pm 0.0003$
$^{48}\text{V}$	15.97	$\epsilon + \beta^+$	983.517	$0.0157 \pm 0.0009$	$0.0132 \pm 0.0002$	$0.0161 \pm 0.0010$
$^{51}\text{Cr}$	27.7025	$\epsilon$	320.0824	$0.0445 \pm 0.0019$	$0.0293 \pm 0.0003$	$0.0206 \pm 0.0012$
$^{54}\text{Mn}$	312.3	$\epsilon + \beta^+$ , $\beta^-$	834.848	$0.0546 \pm 0.0009$	$0.0470 \pm 0.0004$	$0.0157 \pm 0.0010$
$^{59}\text{Fe}$	44.503	$\beta^-$	1099.251	$0.0079 \pm 0.0004$	$0.0051 \pm 0.0001$	$0.0060 \pm 0.0004$
$^{56}\text{Co}$	77.27	$\epsilon + \beta^+$	846.771	$0.0263 \pm 0.0004$	$0.0345 \pm 0.0003$	$0.0023 \pm 0.0001$
$^{57}\text{Co}$	271.79	$\epsilon$	122.0614	$0.1006 \pm 0.0021$	$0.1152 \pm 0.0006$	$0.0837 \pm 0.0005$
$^{65}\text{Zn}$	244.26	$\epsilon + \beta^+$	1115.546	$0.0075 \pm 0.0006$	$0.0037 \pm 0.0001$	$0.0115 \pm 0.0007$

Table 21. Partial number of the nuclides in the whole copper target irradiated by 500 AMeV argon beam (7 days after the end of irradiation).

Nuclide	Half-life $T_{1/2}$ , days	Decay mode	Energy of the most intense $\gamma$ -line (keV)	Experiment, Nucl/ion	FLUKA, Nucl/ion
$^{46}\text{Sc}$	83.79	$\beta^-$	1120.545	$0.0080 \pm 0.0003$	$0.0057 \pm 0.0002$
$^{58}\text{Co}$	70.86	$\epsilon + \beta^+$	810.775	$0.1225 \pm 0.0008$	$0.1295 \pm 0.0011$
$^{60}\text{Co}$	1925.338	$\beta^-$	1332.501	$0.0624 \pm 0.0042$	$0.0515 \pm 0.0006$

### Chapter 3. Experimental results and comparison with the simulations

---

The  $^7\text{Be}$  FLUKA-depth profile upstream the range deviates both in shape and in absolute values from the experimental one. Starting with the first disc, the number of nuclei is underestimated by 30% and decreases until a high maximum appears in the range area. The curve downstream the range agrees with the experiment. Analyzing the results of SHIELD simulations one could see a factor 2 difference upstream the range and the distribution is not increasing, but stays constant in this case. The  $^{22}\text{Na}$  distribution differs dramatically from the other presented depth profiles. In this case FLUKA gives not only a maximum at the depth of the stopping range, but also an increase, a “hill”, right after that. Such a behavior contradicts the one observed in the experiment. SHIELD results describe the experiment within 10%. The amount of  $^{46}\text{Sc}$  is underestimated by FLUKA by 20% in the whole target volume. The FLUKA depth profile is similar in shape to the experimental one, with the exception around the penetration depth: it gives a maximum in the  $^{46}\text{Sc}$  distribution, whereas no maximum is observed in experiment. However, the absence of a maximum could be explained by the lack of resolution. In simulating the depth profile of  $^{48}\text{V}$ , FLUKA underestimates its amount by up to 20%, and the simulations again show a peak at the penetration depth. The SHIELD distribution varies from the experimental one: upstream the range it is constant and in the first disc of the assembly the amount of  $^{48}\text{V}$  is overestimated by 50%. The following region is described with ~10% discrepancy on average. The other depth profiles:  $^{51}\text{Cr}$ ,  $^{54}\text{Mn}$ ,  $^{59}\text{Fe}$ ,  $^{56}\text{Co}$ ,  $^{57}\text{Co}$ ,  $^{65}\text{Zn}$  are reproduced in shape both by FLUKA and SHIELD. In case of  $^{51}\text{Cr}$ ,  $^{54}\text{Mn}$ ,  $^{59}\text{Fe}$  the codes underestimate the amount of nuclei: FLUKA gives 20% ÷ 100%, while SHIELD gives 15% ÷ 400% discrepancies. In case of  $^{57}\text{Co}$  and  $^{65}\text{Zn}$  the experimental depth profiles lie in between FLUKA and SHIELD. In the first case FLUKA gives a few percent overestimation; in latter case the results are by a factor 3 underestimated. SHIELD gives on average 30% discrepancy for both cases. The depth profile of  $^{56}\text{Co}$  is overestimated by the codes: ~30% by FLUKA and ~ 3 times by SHIELD. The depth profiles of  $^{58}\text{Co}$  and  $^{60}\text{Co}$  are simulated very well by FLUKA:  $^{58}\text{Co}$  shows a fine agreement and the  $^{60}\text{Co}$  case agrees within 10%. The total number of the identified radioactive nuclei in the whole target volume is overestimated by FLUKA and SHIELD, by 20% and 40%, respectively.

---

---

---

## CHAPTER 4. DISCUSSION

A heavy ion beam hitting the target activates the target material. The level of the average residual activity per unit thickness depends, besides the target material and the irradiation conditions (ion species, flux, duration of irradiation), on the thickness of the target. The accuracy of the Monte Carlo transport codes in predicting the residual activity depends on the specific projectile-target combination. The findings are discussed in the present Chapter, which is divided according to the target configuration into two sections: (1) Thin target approach, (2) Thick target approach. The third section of this Chapter discusses the applications of activation studies for accelerator needs.

### 4.1. Thin target approach

A thin-foil target was chosen in such a way that the energy losses of the primary beam in the target could be neglected, which means that the reactions happen at one beam energy. The secondary projectiles are produced in nuclear reactions with the target; the majority of them are energetic enough to pass through a thin foil as well. In these conditions the fragmentation of the target nuclei is mostly done by the primary projectiles; the effect of secondary projectiles can be neglected. Thus the accuracy of the according simulations is defined by the accuracy of the reaction cross-sections at a well defined projectile energy.

The present work shows the results of the two experiments which were done with thin-foil targets: aluminum was irradiated by a 426 AMeV argon beam and by uranium beams of different energies (85 – 935 AMeV). In the other experiments described in this thesis, the first disc of the thick-target assembly could be treated in a thin-foil assumption, because the backscattering effects [44] are below the accuracy of these experiments.

The reaction cross-sections for different nuclides produced in aluminum and copper by ion beams were reported in several studies [30 – 32; 36 – 38; 40 – 43]. This

work supplements previous findings by adding data for other projectile-target combinations and energies.

The reaction cross-section is calculated from the following relation [40 – 43; 125]:

$$\sigma = \frac{N_{eoi} \cdot \lambda_i}{N_T \sum_{j=1}^k [Q \cdot \exp(-\lambda_i(k-j)\Delta t)]}, \quad (41)$$

where the number of radioactive nuclides of type  $i$  at the end of irradiation  $N_{eoi}$  is found experimentally using formula (40).  $N_T$  is the number of target atoms,  $Q$  is the number of projectiles per shot (per the irradiation time interval  $\Delta t$ ),  $k$  is the number of shots during the irradiation,  $\Delta t$  is the repetition rate ( $t_{irr}$  is the total irradiation time, so that  $t_{irr} = k\Delta t$ ).

The cross-sections for production of radioactive target fragments in aluminum and copper by different ions with energies between ~380 AMeV and ~500 AMeV are shown in Figs. 78 and 79. Figures present the results of this work and the results of the study [43] done at HIMAC.

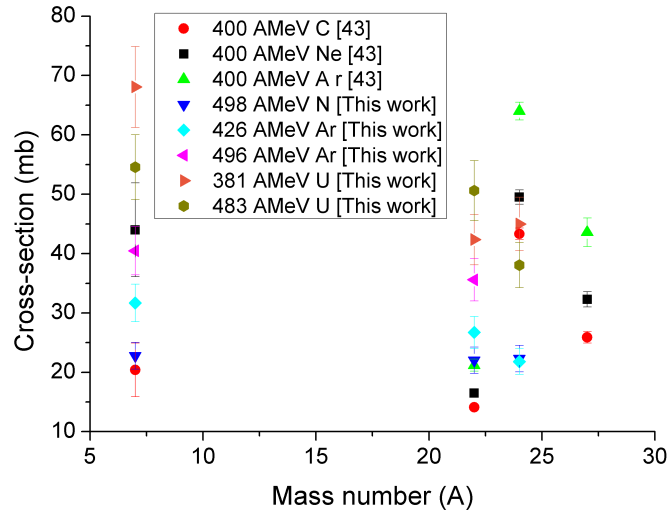


Fig. 78. Reaction cross-sections for  ${}^7\text{Be}$ ,  ${}^{22}\text{Na}$ ,  ${}^{24}\text{Na}$  and  ${}^{27}\text{Mg}$  induced in aluminum by C, N, Ne, Ar and U ions.

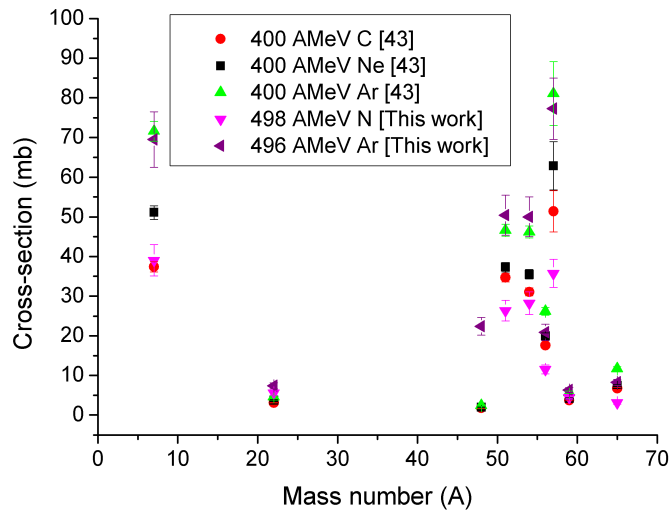


Fig. 79. Reaction cross-sections for  ${}^7\text{Be}$ ,  ${}^{22}\text{Na}$ ,  ${}^{48}\text{V}$ ,  ${}^{51}\text{Cr}$ ,  ${}^{54}\text{Mn}$ ,  ${}^{56}\text{Co}$ ,  ${}^{57}\text{Co}$ ,  ${}^{59}\text{Fe}$  and  ${}^{65}\text{Zn}$  isotopes induced in copper by C, N, Ne and Ar ions.

In general the results obtained in present work follow the pattern: the reaction cross-sections for target-fragments production increase with the mass of the projectile. Factors 3 to 5 are typical for reaction cross-section increase in aluminum and copper targets when the mass of the projectile changes from carbon to uranium at energies around 400 AMeV.

FLUKA calculations agree with the experiment within 10% on average (in case of aluminum: Figs. 24 - 31, 36; in case of copper: Figs. 55 - 62, 64, 65, 72, 73, 76). But there are exceptions where the discrepancy (underestimation) reached up to ~30%. This happened in case of  ${}^7\text{Be}$ ,  ${}^{22}\text{Na}$ , and  ${}^{51}\text{Cr}$  produced in the copper target irradiated by a 496 AMeV argon beam. The number of  ${}^{65}\text{Zn}$  produced in experiments with copper when irradiated by nitrogen and argon ions is underestimated by about a factor 3.

MARS results for  ${}^7\text{Be}$  produced in the aluminum target by a 496 AMeV argon beam agree with the experiment within 5%; in case of  ${}^{22}\text{Na}$  the discrepancy is about 30%. In the experiment with the aluminum target and a 483 AMeV uranium beam the numbers are overestimated by 30% by MARS.

SHIELD gives not more than a factor of 2 discrepancy for all identified fragments discussed above.

## 4.2. Thick target approach

The radioactive nuclei detected in the thick target could be either target-nuclei fragments or projectile fragments. The nuclides found upstream the stopping range of the primary beam are fragments of target-nuclei. The fragmentation is done by the secondary projectiles as well as by the primary beam particles. Downstream the range there is a mixture of the target and the projectile fragments.

The development of the shower of secondary projectiles (secondary beam) during

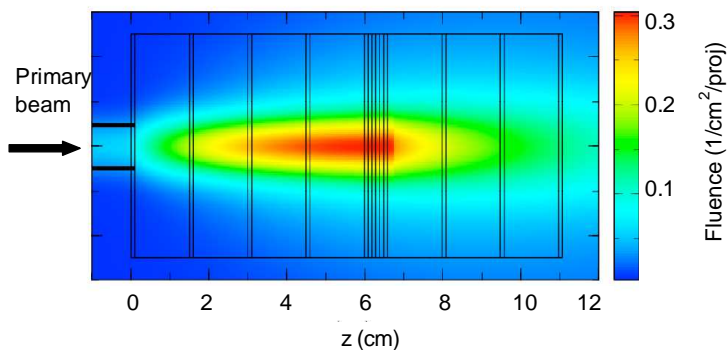


**Fig. 80. PHITS-simulations on a 500 AMeV argon beam with initial cross-section of 1 cm impinging on an aluminum target: tracks of the primary projectiles and the projectile fragments during the irradiation of the target.**

the irradiation of a target material by a heavy-ion beam is given in Fig. 80 for the case of an aluminum target irradiated by a 500 AMeV argon beam.

This Figure shows particles' tracks for the initial projectiles

and for all the projectile fragments as calculated using PHITS code [130]. It could be seen that besides the increase of the beam cross-section, the total fluence of all the projectiles also increases with depth until the primary beam is stopped.

The secondary projectiles can fragment the target nuclei as well as the primary projectiles do. The contribution of the secondary beam to the activation of the target upstream the range could be studied by following the steps: (1) Finding the depth profiles of the radioactive nuclei in a thick target, (2) calculating the primary-projectile energy dependence on depth, (3) finding the dependence of the number of nuclides produced and deposited in thin-foil targets, on energy of the primary projectiles, (4) bringing in correspondence the energy of the beam on the thin foil and the depth in the thick target where the primary beam had the same energy, (5) calculating the difference between the number of radionuclides produced in a thick-



## 4. 2. Thick target approach

target experiment and the number of respective radionuclides produced in thin-foil experiment. This number reveals the nuclei produced by secondary projectiles. If the difference is negligible, this indicated that the nuclei were mainly produced by the primary ions.

Figures 81 and 82 show the contribution of the secondary projectiles in the activation of the target upstream the stopping range, as found in the experiments (see Figs. 29, 30, 35, 36 also including respective simulations) with aluminum targets and uranium beams. With increasing depth, the  ${}^7\text{Be}$  and  ${}^{22}\text{Na}$  production by projectile fragments in this case is growing linearly till the stopping range of the primary beam. At that region the isotope density is increased by factors 2.5 and 8 for  ${}^7\text{Be}$  and  ${}^{22}\text{Na}$ , respectively.

In a next step, the constant production rate of target fragments by the primary beam, as shown in Figs. 81 and 82, was checked for other projectile-target combinations. FLUKA-simulations were done for aluminum and copper foils irradiated by nitrogen and argon beams at different energies.

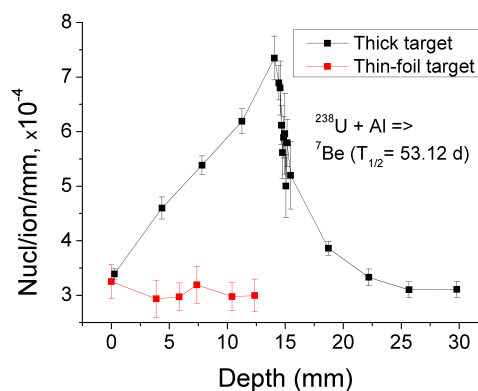


**Fig. 81. Comparison of the amount of  ${}^7\text{Be}$  produced by a uranium beam in a thick-target and in a thin-foil experiment, showing the big influence of the secondary projectiles.**

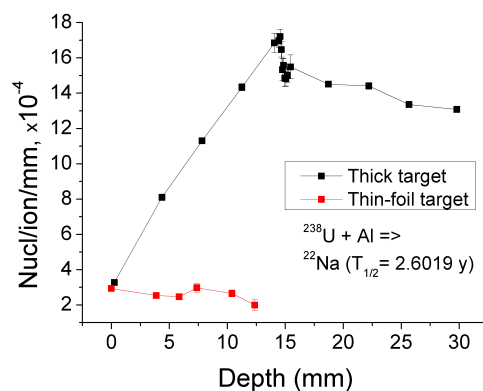


**Fig. 82. Comparison of the amount of  ${}^{22}\text{Na}$  produced by a uranium beam in a thick-target and in a thin-foil experiment, showing the big influence of the secondary projectiles.**

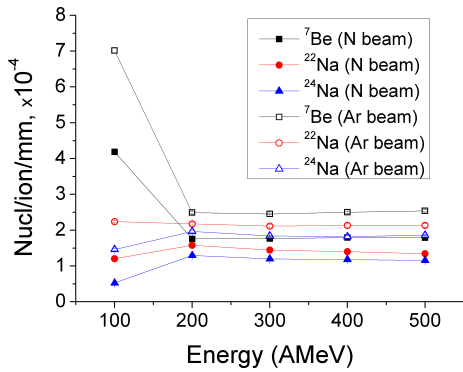


**Fig. 83 . The numbers of target-fragments produced in thin aluminum foils irradiated by nitrogen and argon beams, per primary projectile, per unit thickness vs. beam energy.**

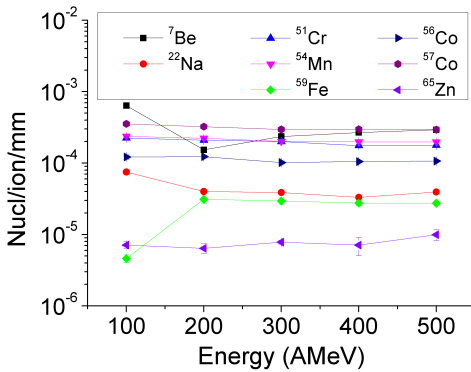


**Fig. 84. The numbers of target-fragments produced in thin copper foils irradiated by nitrogen beams, per primary projectile, per unit thickness vs. beam energy.**

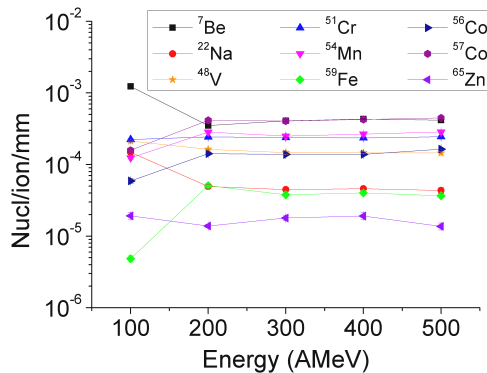


**Fig. 85. The numbers of target-fragments produced in thin copper foils irradiated by argon beams, per primary projectile, per unit thickness vs. beam energy.**

The results of these simulations are given in Figs. 83 – 85. It could be seen, that in the energy range from 200 AMeV to 500 AMeV the number of the produced target fragments stays nearly constant. Therefore, if the depth-distribution of nuclei is constant upstream the range, this indicates that the primary beam was the main reason for target-nuclei fragmentation. Analysis of the depth profiles shows that  $^7\text{Be}$  and  $^{22}\text{Na}$  detected in copper were mainly produced by primary nitrogen and argon beams (Figs. 55, 56, 66 and 67). The  $^7\text{Be}$  detected in aluminum target was mainly produced by primary nitrogen (Fig. 24). All the other target fragments experimentally detected upstream the range were mainly produced by the secondary projectiles.

Downstream the range the activation is done by projectile fragments only. If their energy is not sufficient for fragmenting the target nuclei or the intensity is too low to produce enough radioactive isotopes, then the distribution drops significantly after the stopping range (e.g. Fig. 56). At higher energies and at higher

## 4. 2. Thick target approach

numbers of the secondary particles, the gradual decrease of the number of radioactive nuclides downstream the primary projectile range is observed (e.g. Fig. 61).

According to Ref. [41], when the difference in mass numbers between the target nuclei and their fragments is large, then the primary projectiles play a major role in fragmentation of the target. The secondary beam starts playing an important role in case of a small difference in according mass numbers. It should be noted that the study [41] was done with thick copper targets and different beams from proton up to neon having energies 100 AMeV and 230 AMeV.

The experimental data obtained in present work confirms this statement for a copper target irradiated by nitrogen and argon beams at ~500 AMeV. In case of an aluminum target however, the statement is valid for ~500 AMeV nitrogen and is violated in case of ~500 AMeV argon and uranium irradiations: the heavier projectiles develop a shower of secondary particles while passing through matter. These secondary particles are the main source for production of  $^7\text{Be}$  and  $^{22}\text{Na}$ .

With increasing energy, the number of the produced projectile fragments increases. To illustrate this, the FLUKA-simulations on aluminum targets irradiated by uranium beams having 200, 500 and 950 AMeV were done. The stopping ranges in these three cases would be 3.25 mm, 15.15 mm and 37.2 mm, respectively. Figure 86 shows the heaviest fragment of the primary  $^{238}\text{U}$  beam. It could be seen that at higher energies the number of  $^{237}\text{U}$  drastically increases. The increased number of projectile fragments – leading to high neutron radiation – finally causes the increase of the number of target fragments: the depth distributions of  $^7\text{Be}$  and  $^{22}\text{Na}$  shown in Figs. 87 and 88, respectively, confirm this.

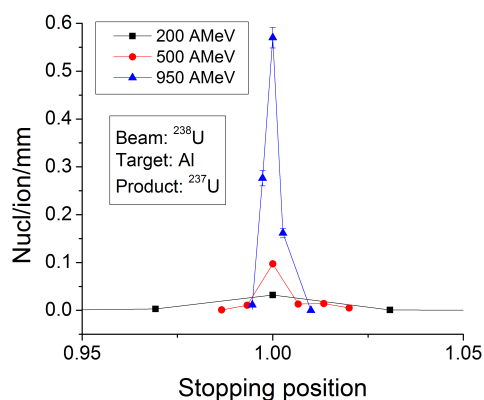


**Fig. 86.** FLUKA-simulations of the  $^{237}\text{U}$  depth distribution in an aluminum target irradiated by uranium beams at different energies: 200, 500 and 950 AMeV, at zero cooling time.

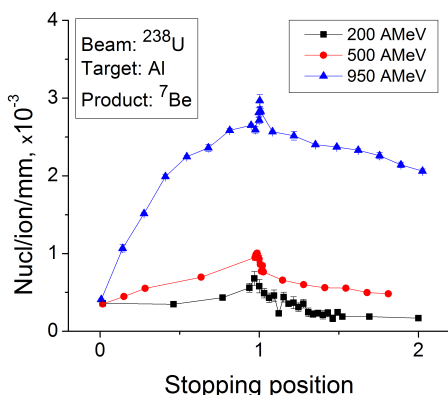


**Fig. 87.** FLUKA-simulations of the  ${}^7\text{Be}$  depth distribution in an aluminum target irradiated by uranium beams at different energies: 200, 500 and 950 AMeV, at zero cooling time.

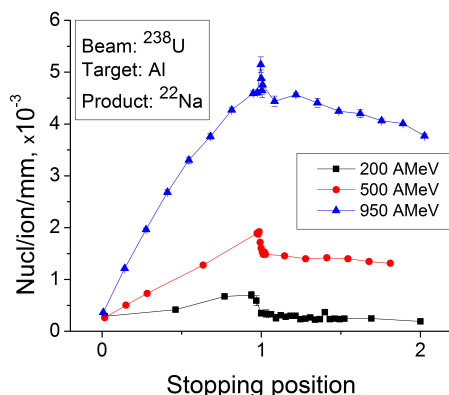


**Fig. 88.** FLUKA-simulations of the  ${}^{22}\text{Na}$  depth distribution in an aluminum target irradiated by uranium beams at different energies: 200, 500 and 950 AMeV, at zero cooling time.

Based on these findings, the previous statement about the influence of the primary and secondary beams on fragmentation of target nuclei appears to be of limited relevance only: with higher energy and heavier primary projectiles the secondary projectiles make a significant contribution to the light fragments production.

There is an interesting peculiarity in the depth profiles of some target fragments (see e.g. Fig. 55): a narrow isotope-density maximum is observed in the primary-projectile range area. (No maxima are observed in the experiments with aluminum and copper targets, and argon beam, possibly because of the low experimental resolution at the range area). These maxima appear in case of increased production cross-sections at low energies. The maximum in the depth-profile of  ${}^{65}\text{Zn}$  produced in copper target irradiated by a nitrogen beam (Fig. 62) is explained by an increased proton-capture rate at low energies.

The depth-distribution of the projectile fragments can be obtained in activation experiments for those isotopes only which are heavier than the target nuclei. If the projectile fragments are lighter than the target, then their inputs could not be carefully distinguished from those of the target fragments.

The behavior of the depth profiles of secondary projectiles depends on their proton number difference from the primary projectiles. The secondary projectiles with a proton number close to those of a primary projectile (in case of uranium beam this

difference is  $\Delta Z < \sim 20$ ) have similar behavior: the distribution is symmetric, with a clear maximum (Fig. 37 – 40; 52 – 54). This maximum appears because the heavy fragments produced at the beginning of the target have approximately the same energy and therefore the same range as the primary uranium ions. The “hill” is also observed in the depth distribution of  $^7\text{Be}$  produced in a copper target when irradiated by a nitrogen beam (Fig. 55), and in the depth distribution of  $^{22}\text{Na}$  produced in a copper target irradiated by an argon beam (Fig. 67). The proton number differences with primary projectile in these cases are  $\Delta Z = 3$  for  $^7\text{Be}$  and  $\Delta Z = 7$  for  $^{22}\text{Na}$ . The maximums are detectable because the number of the respective copper fragments is much less than those of the projectile fragments.

Increasing the difference in the charge numbers ( $\Delta Z > \sim 20$ ) causes the distribution of the projectile fragments to become asymmetric, with a long “tail” (Fig. 44 – 51). This happens because the lighter fragments are produced at different depths of the target and have much longer stopping range. In case of light uranium fragments like  $^{83}\text{Rb}$ ,  $^{99}\text{Mo}$  and  $^{127}\text{Xe}$ , FLUKA-simulations reveal a second maximum in the depth profile. The origin of this maximum is not clear. The resolution of that area in the experiment was too low to observe such a maximum; therefore the experiment with a uranium beam and a thick aluminum target should be repeated with a higher resolution.

The spatial behavior of projectile- and target-fragments for two opposite cases: a heavy beam on a light target, and a light beam on a heavy target, is summarized in Figs. 89 and 90. These figures present the experimental results for an aluminum target irradiated by a  $\sim 500$  AMeV uranium beam and for a copper target irradiated by a  $\sim 500$  AMeV nitrogen beam, respectively.

In the first case the heavy projectile fragments can easily be distinguished by their distribution, while in the latter case this cannot be done as mentioned before.

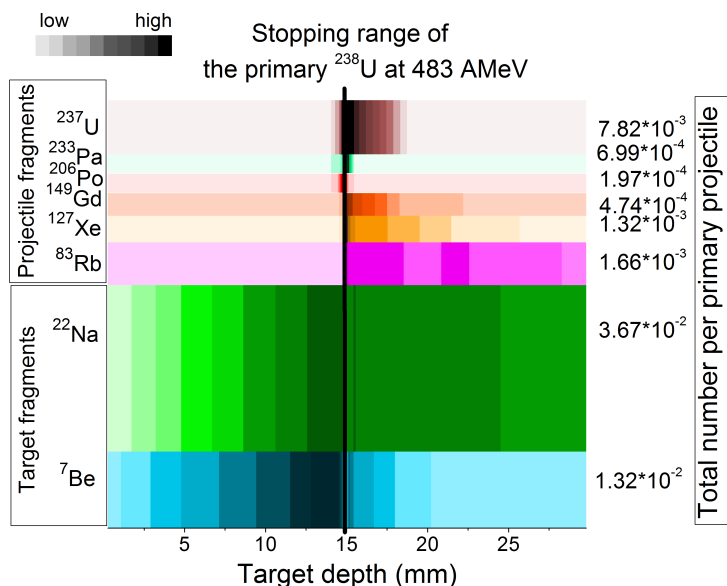


Fig. 89. The experimental depth distribution of the chosen projectile- and target-fragments produced in an aluminum target irradiated by a 483 AMeV uranium beam, after a cooling time of 7 days. The color code is linear, values increasing from pale to deep shade.

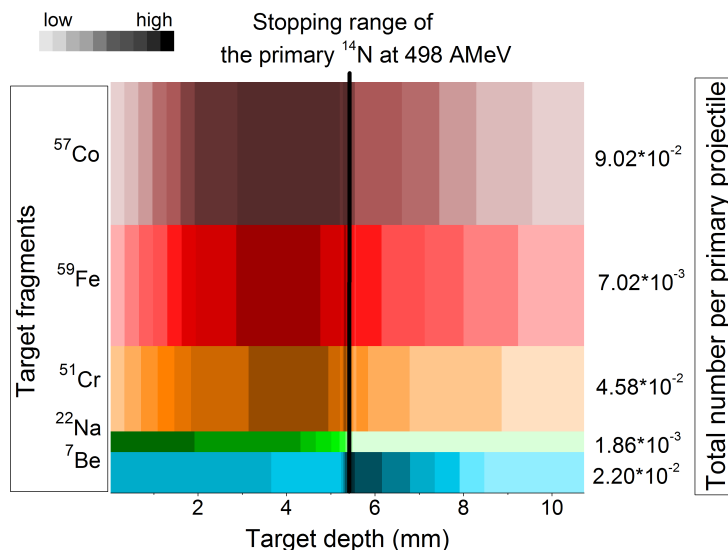


Fig. 90. The experimental depth distribution of the chosen target-fragments produced in a copper target irradiated by a 498 AMeV nitrogen beam, at a zero cooling time. The color code is linear, values increasing from pale to deep shade.

### 4.3. Activation studies for accelerator applications

Keeping residual activity below a certain limit is important to avoid high dose rates and to allow for hands-on maintenance of the machine, as it was pointed out in the Introduction. The heavy-ion beam-loss criteria [9] were introduced for energies of the primary beam between 200 AMeV and 1 AGeV. They are based on the finding that isotope inventory in the target does not strongly depend on the projectile species.

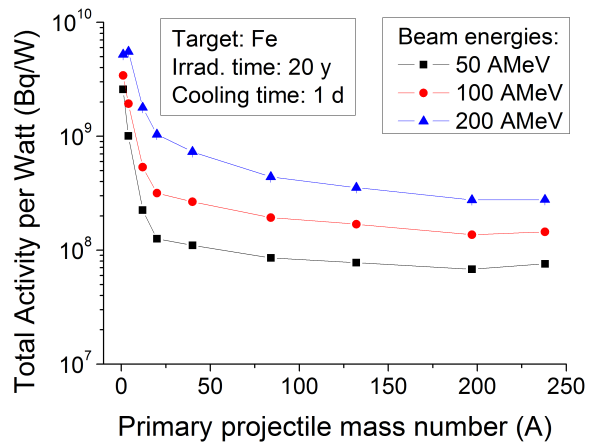


Fig. 91. Total activity per 1 W after 1-day cooling of iron target irradiated for 20 years by different low-energy projectiles

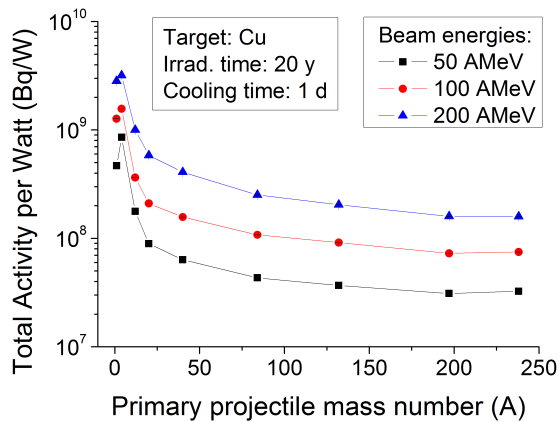


Fig. 92. Total activity per 1 W after 1-day cooling of copper target irradiated for 20 years by different low-energy projectiles.

Present study is a broadening of the heavy-ion beam loss criteria to include beam-target interaction at low energies and long irradiation times.

Let us consider an irradiation of iron and copper bulky targets by ion beams of 50 AMeV, 100 AMeV and 200 AMeV. The target is a cylinder with a radius of 20 cm and a length of 60 cm. The FLUKA-simulations of such targets “irradiated” for 20 years by ion beams of different species (H, He, C, Ne, Ar, Kr, Xe, Au, U) were done. The activation of each target irradiated by different beams was studied at different cooling down times: immediately after the end of irradiation, 4 hours after, 1 day, 1 week, 2 months, 1 year, 2 years, 5 years, 10 years, 20 years and 50 years.

The total activities of iron and copper targets irradiated for 20 years by different ion beams of 1 W at 50, 100 and 200 AMeV are shown in Fig. 91 and 92 after 1-day of cooling. The activity dependence on the projectile mass number for low energies of the beam is in agreement with the earlier findings for high-energy cases (see Fig. 3): i.e. provided the same beam power, the total activity decreases with increasing projectile mass number and decreasing energy.

The residual activity induced in the target by a proton is lower than that induced by a helium ion, because helium fragments into tritium (half life  $T_{1/2} = 12.323$  y). At 50 AMeV this effect is more pronounced (see Fig. 92), because the ions at this energy are able to destroy the nucleus completely and the variety of the produced isotopes is large, whereas the protons are able to knock out maximum 5 nucleons from the initial target.

At low energies and long irradiation times the isotope inventory in the target differs depending on the projectile. Figure 93 [9] presents the relative activities of the radio-nuclides 1 day after the end of 100-days irradiation of a copper target by 1 AGeV ions. Figure 94 presents the relative activities of the same nuclides 1 day after

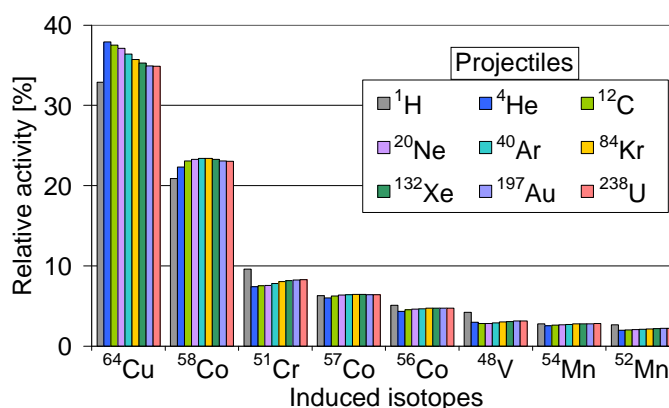


**Fig. 93.** Relative activities of the isotopes induced by 1 AGeV projectiles from proton up to uranium irradiating the bulky copper target for 100 days. Cooling time: 1 day, [9].

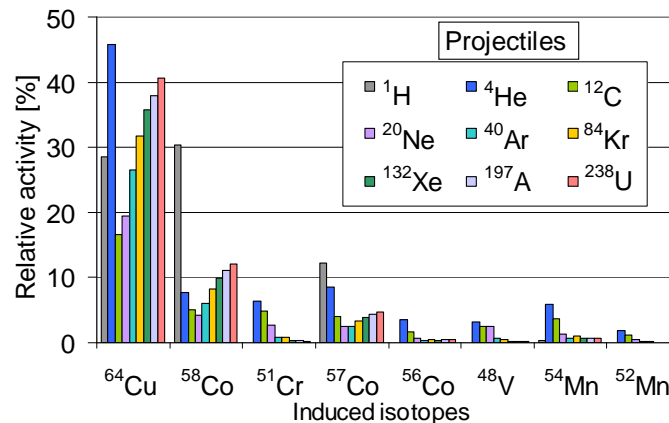


**Fig. 94.** Relative activities of the isotopes induced by 50 AMeV projectiles from proton up to uranium irradiating the bulky copper target for 20 years. Cooling time: 1 day; from FLUKA-simulations.



### 4.3. Activation studies for accelerator applications

the end of 20-years irradiation of a thick copper target by the same projectiles from proton to uranium with energy 50 AMeV. As could be seen from Fig. 94, the relative activities are strongly dependent on the projectile species at low energies. This means that the time evolution of the activity would also be different for each case. Time dependence of the total activity of copper target irradiated by 50 AMeV beams normalized to the total activity of this target at the end of irradiation is given in Fig. 95.

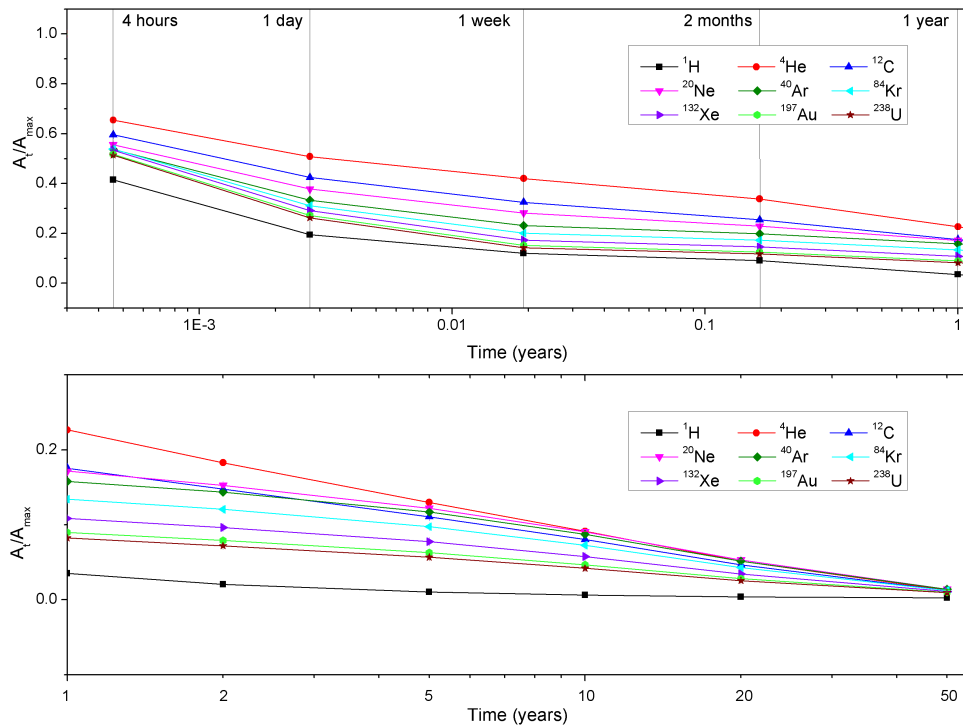


**Fig. 95.** Time-dependence of the total activity of the copper target induced by different beams of 50 AMeV irradiating the target for 20 years, at a time point  $t$ ,  $A_t$ , normalized to the total activity induced by respective beam at the end of irradiation,  $A_{max}$ . Upper plot: cooling time 0 ÷ 1 year; lower plot: cooling time 1 ÷ 50 years.

The evolution of activity could not be described by a generic curve, therefore the heavy-ion beam loss criteria could not be extended to low energies and long irradiation times by scaling the beam intensities as it was done in Ref. [9], because the induced radionuclides have different impact on the dose rate according to the type of the decay and its energy.

Therefore for finding the beam-loss limits at low energies, the dose rates induced by the beam of interest and at a cooling time of interest should be considered.

The maximum dose rates at a distance 30 cm (Fig. 96) from the iron and the copper bulky targets irradiated for 100 days by 1-W beams of different species at 50 AMeV and at 100 AMeV are shown in Figs. 97 – 100 at different cooling times. As discussed earlier, the dose rate of 1 mSv/h at a distance 30 cm from the components surface is considered to be tolerable for the hands-on maintenance. Therefore, as could be seen from the Figures, to ensure the access to iron and copper components after 100-days of machine operation with proton beam and a cooling time of 4 hours, the proton-beam losses at 50 and 100 AMeV should be approximately ~1 W/m. In case of a uranium beam, the beam losses to iron components should be restricted to 200 W/m in case of 50 AMeV beam and to 55 W/m in case of 100 AMeV beam. If the components are made of copper, the beam losses should be restricted to 120 W/m in case of 50 AMeV, and to 80 W/m in case of 100 AMeV uranium beams.

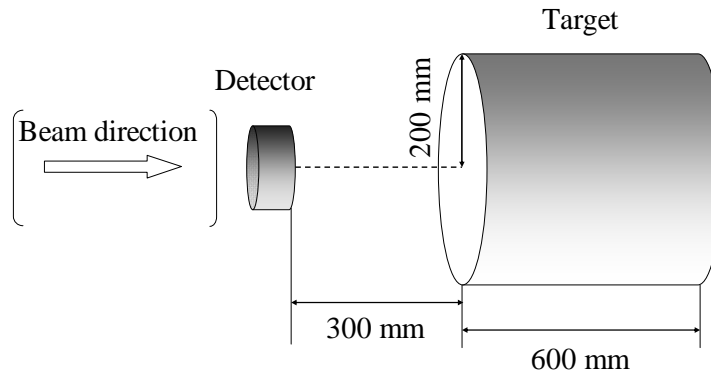


Fig. 96. Position of a detector for counting the dose rate with respect to the bulky target. (The target self-shielding is included in simulations).

### 4.3. Activation studies for accelerator applications

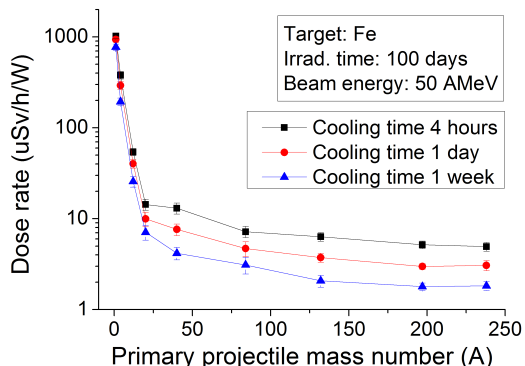


Fig. 97. Maximum dose rate at a distance of 30 cm from the iron target irradiated for 100 days by 1-W beams of different species having 50 AMeV, at different cooling times.

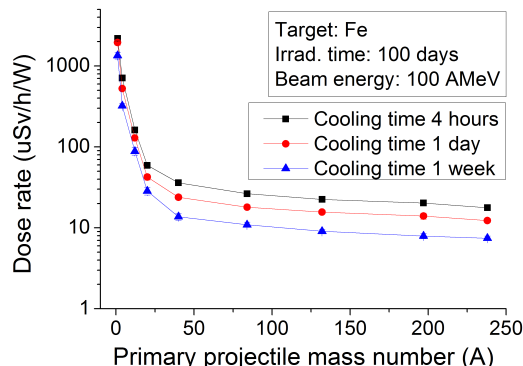


Fig. 98. Maximum dose rate at a distance of 30 cm from the iron target irradiated for 100 days by 1-W beams of different species having 100 AMeV, at different cooling times.

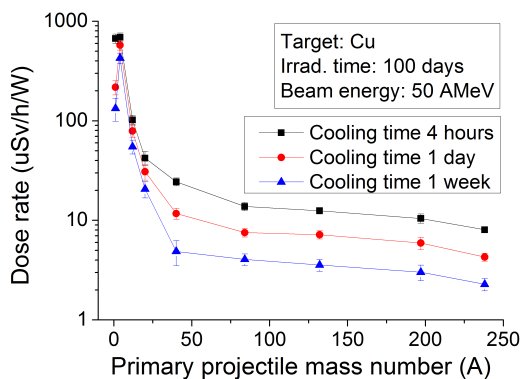


Fig. 99. Maximum dose rate at a distance of 30 cm from the copper target irradiated for 100 days by 1-W beams of different species having 50 AMeV, at different cooling down times.

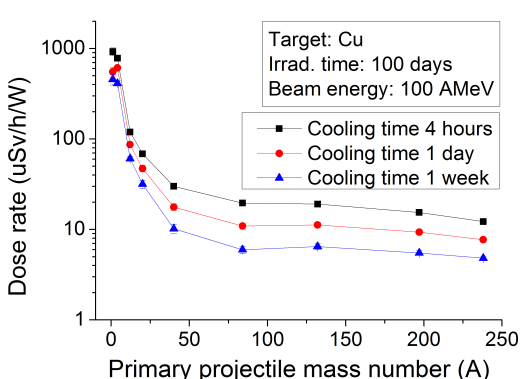
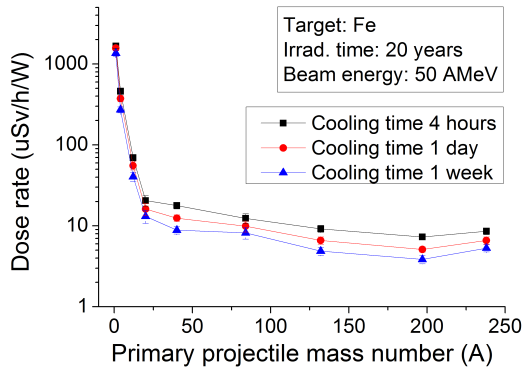


Fig. 100. Maximum dose rate at a distance of 30 cm from the copper target irradiated for 100 days by 1-W beams of different species having 100 AMeV, at different cooling down times.

If the irradiation was 20 years, the maximum dose rates at 30 cm from the same targets would on average be ~40% higher at 4 hours delay time (Figs. 101 – 104). At these conditions uranium beam losses to iron components should be restricted to 120 W/m and 40 W/m for the beams having 50 AMeV and 100 AMeV, respectively. The copper components could accommodate 85 W/m of 50 AMeV and 50 W/m of 100 AMeV uranium beams in order to allow for hand-on maintenance 4 hours after the shut down.

## Chapter 4. Discussion

The obtained uranium beam-loss criteria dependences on cooling times are given in Fig. 105 for 100 days and in Fig. 106 for 20 years irradiation of iron and copper targets by 50 AMeV and 100 AMeV beams.



**Fig. 101.** Maximum dose rate at a distance of 30 cm from the iron target irradiated for 20 years by 1-W beams of different species having 50 AMeV, at different cooling times.

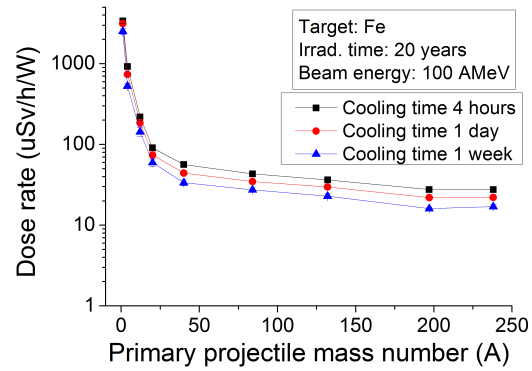


**Fig. 102.** Maximum dose rate at a distance of 30 cm from the iron target irradiated for 20 years by 1-W beams of different species having 100 AMeV, at different cooling times.

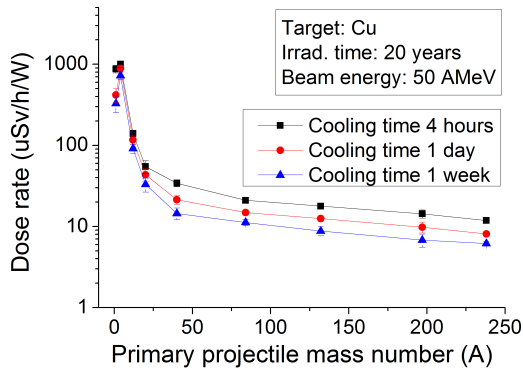


**Fig. 103.** Maximum dose rate at a distance of 30 cm from the copper target irradiated for 20 years by 1-W beams of different species having 50 AMeV, at different cooling times.

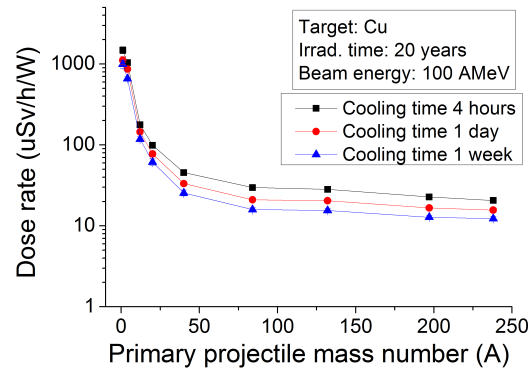


**Fig. 104.** Maximum dose rate at a distance of 30 cm from the copper target irradiated for 20 years by 1-W beams of different species having 100 AMeV, at different cooling times.

### 4.3. Activation studies for accelerator applications

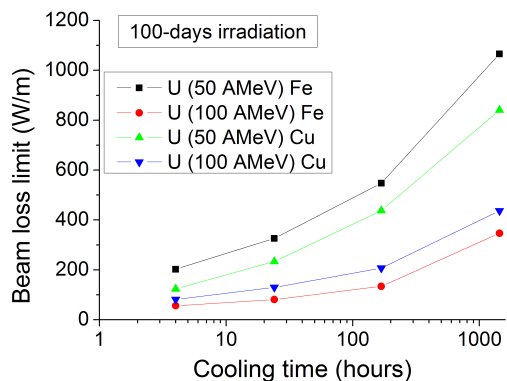


**Fig. 105.** The uranium beam-loss criteria dependence on cooling time, for 100-days irradiation of Fe and Cu at 50 AMeV and at 100 AMeV.

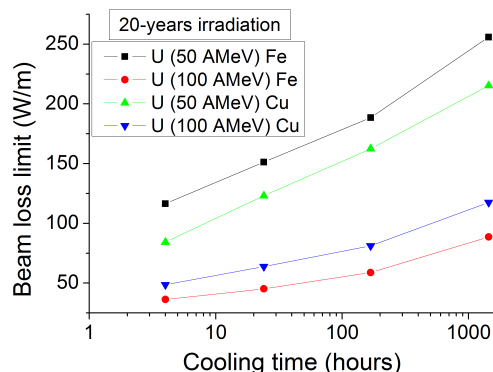


**Fig. 106** The uranium beam-loss criteria dependence on cooling time, for 20-years irradiation of Fe and Cu at 50 AMeV and at 100 AMeV.

It should be noted that the results of the FLUKA-calculations at energies below 150 AMeV are preliminary, because this energy is considered to be the limit of validity of the code at present. The comparison of the FLUKA-simulations with the experiments performed in this work shows that FLUKA gives correct results for low-energy projectiles.

Finally, the situation for 1 AGeV beams is discussed. The study of the best suited (in the sense of radiation hazard) accelerator relevant materials was done in the following way. The FLUKA-simulations of a thick cylindrical target with a radius of 20 cm and a length of 60 cm, irradiated by 1 GeV proton beam of 1 Watt for 100 days and 20 years were done. (Figures 1 and 93 show that at a 1 AGeV beam energy the isotope inventory does not strongly depend on the projectile species, thus the irradiation by a 1 AGeV proton beam gives the same relative activities of the produced nuclides as in case of a uranium beam when the beam powers and irradiation times are identical). Therefore the simulations were done with protons only in order to save CPU time. The target materials were typical ingredients of stainless steel, like Ti, Cr, Mn, Fe, Ni, Nb, Mo, and other materials used for accelerator components or shielding, like C, Al, Cu, Pb. Total residual activities of the targets hit by 1 GeV proton beams of 1 Watt ( $6.24 \cdot 10^9$  particles) are shown in Fig. 107 after 100 days of continuous irradiation, and in Fig. 108 after 20 years of continuous irradiation, for different cooling down times. In general, the heavier the target material is, the

## Chapter 4. Discussion

more active it will get. However, as could be seen from these Figures short-term irradiation differs from the long-term one because of the accumulation of the long-lived radioactive nuclei. In case of 100-days irradiation the least activated materials which are used in stainless steel production would be titanium, iron and manganese. The other possible stainless steel components would be more than factor of 1.5 higher activated. In case of 20-years irradiation, titanium stays the least activated material, whereas all the others, including iron, are at least a factor of two more active; among those is nickel which is 3.5 times more active than titanium. Talking about the absolute values of the total residual activities, such materials as carbon, aluminum, manganese, iron and nickel, get up to 3 times more active after extending the irradiation time to 20 years.

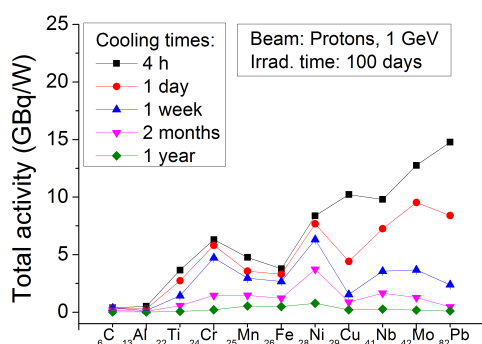


**Fig. 107.** Total activities of the bulky targets per 1-W proton beam of 1 GeV irradiating the target for 100 days, at different cooling times.

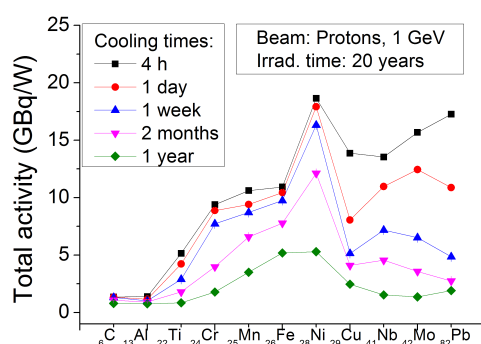


**Fig. 108.** Total activities of the bulky targets per 1-W proton beam of 1 GeV irradiating the target for 20 years, at different cooling times.

As it was mentioned earlier, the dose rates in the vicinity of the irradiated materials could not be derived from the total target activities, because different types of decay have different impacts on the dose calculations. Figures 109 and 110 show the dose rates of the studied targets irradiated for 100 days and 20 years, respectively. These figures in comparison with Fig. 107 and Fig. 108 show that even though the activation of lead is one of the highest, the dose rate at the distance 30 cm from the target would be one of the lowest in comparison with the other studied materials. The highest dose rate would be in the vicinity of nickel, niobium and molybdenum targets several days after the end of irradiation. The dose rates at the distance 30 cm from the

### 4.3. Activation studies for accelerator applications

other studied targets would be approximately 2 times lower; therefore using them for accelerator components is preferable from point of view of the hands-on maintenance.

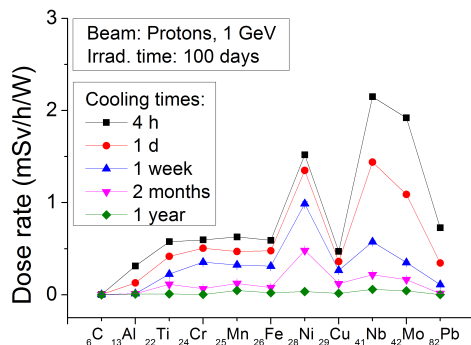


**Fig. 109.** Maximum dose rate per 1 W at a distance of 30 cm from the target irradiated for 100 days by 1 GeV proton beam, at different cooling times.

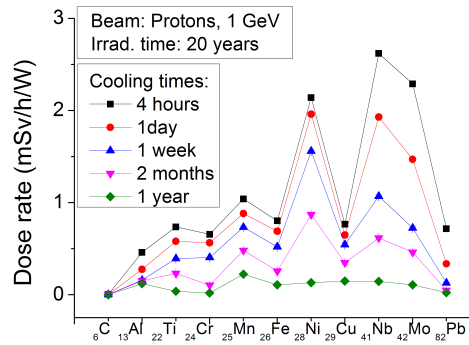


**Fig. 110.** Maximum dose rate per 1 W at a distance of 30 cm from the target irradiated for 20 years by 1 GeV proton beam, at different cooling times.

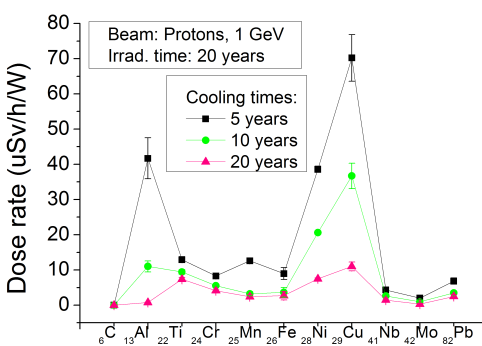


**Fig. 111.** Maximum dose rate per 1 Watt at the distance 30 cm from the surface of the target, irradiated by 1 GeV protons for 20 years, at different cooling times.

Figure 111 shows the dose rates after 20 years of the irradiation by a 1 GeV proton beam of 1 Watt, at a distance of 30 cm. The cooling times in this case are considerably longer than in the previous Figure. It could be seen that aluminum, titanium, nickel and copper are the most radiation-hazardous materials in comparison to the other studied ones. Therefore in case of long irradiation times and from the view point of a handling after 5 years of a cooling down time, aluminum and copper contents play an important role.

---



---

## CONCLUSION AND OUTLOOK

Within the present work several activation experiments were done in order to obtain data on the interactions of heavy ions with different targets for a verification of the Monte Carlo transport codes. Two types of targets were irradiated: a thin foil for studying the species and amounts of radioactive target-nuclei fragments, and a thick target assembled from activation foils and spacers – for studying the depth distribution of the radioactive nuclides produced and stopped in the target. Gamma-spectroscopy analysis was performed after the end of irradiation in order to obtain this information.

The following Table 22 shows the projectile-target combinations which were studied experimentally in the present work and in earlier activation studies.

Forty five depth profiles were obtained in experiments with thick targets. An experiment with copper target and 500 AMeV argon beam was an extension of an earlier study [8]: the depth profiles of activation behind the stopping range of primary projectiles were now obtained with higher resolution. The increase in the  $^{22}\text{Na}$  distribution downstream the stopping range of a 500 AMeV argon was observed for the first time. A similar increase was observed for  $^7\text{Be}$  produced in the copper target irradiated by a nitrogen beam. It appears because the respective projectile fragments stop at this depth of the target.

The obtained experimental results were compared with the results of respective simulations by FLUKA, MARS and SHIELD. These codes use different models for calculating particle transport and interactions, therefore they give different results.

The experiment with a 426 AMeV argon beam and with a thin-foil aluminum target is perfectly described by FLUKA.

In thick-target experiments it was observed that the stopping ranges of ions with energies up to 500 AMeV are described by all three codes in a good way, i.e. within ~5% error bars. The simulated number of produced nuclides, on the other hand, does not always give good agreement with the experiment.

## Conclusion and Outlook

**Table 22. List of the studied target materials, types of the projectiles and their energies.**

Target material	Beam (Energy, AMeV)	Reference
C	<sup>4</sup> He (100, 230)	[39]-[42]
	<sup>12</sup> C (100, 400)	[39] -[42]
	<sup>20</sup> Ne (100, 230, 400)	[39] -[42]
	<sup>28</sup> Si (800)	[40]-[42]
	<sup>40</sup> Ar (230, 400)	[39] -[42]
Al	<sup>4</sup> He (100, 230)	[39] -[42]
	<sup>12</sup> C (100, 200, 230, 400)	[39] -[42]
	<sup>14</sup> N (498)	[This work]
	<sup>20</sup> Ne (100, 230, 400)	[39] -[42]
	<sup>28</sup> Si (800)	[40]-[42]
	<sup>40</sup> Ar (230, 400)	[39] -[42]
	<sup>40</sup> Ar (426, 496)	[This work]
Cr, Fe, Ni, Pb	<sup>238</sup> U (85, 174, 279, 325, 381, 483, 584, 684, 785, 935)	[This work]
	<sup>4</sup> He (100, 230)	[39] -[42]
	<sup>12</sup> C (100, 230, 400)	[39] -[42]
	<sup>20</sup> Ne (100, 230, 400)	[39] -[42]
	<sup>28</sup> Si (800)	[40]-[42]
Co	<sup>40</sup> Ar (230, 400)	[39] -[42]
	<sup>12</sup> C (200)	[44]
Stainless steel	<sup>238</sup> U (500, 950)	[6], [7]
Cu	<sup>4</sup> He (100, 230)	[39] -[42]
	<sup>12</sup> C (100, 135, 200, 230, 400, 2083)	[30], [38],[39] -[42]
	<sup>14</sup> N (278)	[32]
	<sup>14</sup> N (498)	[This work]
	<sup>20</sup> Ne (100, 211, 230, 377, 400)	[37], [39] -[42]
	<sup>28</sup> Si (800)	[40]-[42]
	<sup>40</sup> Ar (230, 400, 2000)	[36], [39] -[42]
	<sup>40</sup> Ar (500, 1000)	[8]
	<sup>40</sup> Ar (496)	[This work]
Ag	<sup>238</sup> U (500, 950)	[6], [7]
	<sup>12</sup> C (2100)	[31]

Comparison of the experiment with FLUKA-simulations on the total number of radionuclides produced and identified in aluminum targets showed an agreement within 5% for FLUKA, within 15% for MARS and within a factor 2 for SHIELD (see Tables 8, 11, and 15, and according figures). In case of copper targets the maximum discrepancies of respective numbers in the whole target volume were ~10% and ~30% in case of FLUKA and SHIELD, respectively (see Tables 17, 18, 20, 21, and according figures).

Summarizing, according to the made experiments and performed simulations with different projectiles in both target materials, the average discrepancies of the total number of detected nuclides in the whole target volume are ~5% for FLUKA, ~15% for MARS and ~50% for SHIELD: For radiation protection applications the disagreement within a factor of 2 is considered to be still tolerable. It should be underlined that not all the experiments were simulated with all the mentioned codes.

For beams with energies above 200 AMeV Ref. [9] showed that a scaling of beam loss criteria for different projectile mass numbers is possible. It was found in this work that at energies below 200 AMeV and after long irradiation times the time-dependence of the residual activity induced in the target could not be described by means of a generic curve (compare Figs. 93 and 94 of this thesis). Therefore a scaling law for the activation cannot be applied. The dose rates should be considered individually in such cases.

**Table 23. The calculated beam-loss criteria for uranium ions impinging on various bulky targets for 100 days and for 20 years, allowing for hands-on maintenance 4 hours after the shutdown.**

Target material	Energy, AMeV	Beam-loss limits, W/m	
		Irradiation time: 100 days	Irradiation time: 20 years
Fe [This work]	50	200	120
	100	60	40
Cu [This work]	50	120	85
	100	80	50
Stainless steel [9]	200	60	-
	500	12	-
	1000	5	-

Table 23 shows the beam loss limits as simulated with FLUKA for iron and copper targets irradiated by 50 AMeV and 100 AMeV uranium beams. The loss limits between 40 W/m and 200 W/m are clearly less strict than in case of protons, or in case of higher energy uranium beams (see Table 23 for stainless steel targets irradiated with energies up to 1 AGeV).

The activation studies of the materials most commonly used in accelerator construction (typical stainless steel components plus carbon, aluminum, copper and lead) were done.

The bulky targets made of chromium, nickel, niobium, copper, molybdenum and lead showed the highest total activity shortly after the end of the irradiation.

## Conclusion and Outlook

---

However the dose rates at the distance 30 cm from the bulky target surface were the highest in case of nickel, niobium and molybdenum few days after the irradiation.

The dose rates in the vicinity of carbon, aluminum, titanium, chromium, copper and lead targets were twice lower which makes their use for accelerator applications preferable from point of view of the hands-on maintenance.

In case of long irradiation and long cooling time aluminum, titanium, nickel and copper show the highest dose rates at the distance 30 cm from the target surface. This should be taken into account when long irradiation periods are foreseen and a further storage of the irradiated materials is needed.

The increased energies of accelerators and their ability to operate with various heavy ions allow for studying the relevant heavy-ion interactions quantitatively and to compare them with code predictions. The further development of theoretical methods for a description of such processes is strongly linked with obtaining these experimental results.

The Monte Carlo transport codes used for simulating the heavy-ion reactions are improved accordingly to fit the experimental data. Lack of data is filled in by the extrapolation of existing data on the region of interest. Table 22 showed the list of studied projectile-target combinations, used for benchmarking of the codes. As could be seen from this table, the experiments on interaction of medium-mass beams (e.g. Kr, Xe, Ta) with various target-materials are missing, as well as data on an interaction of heavy beams with heavy targets. Next activation experiments are already planned at GSI.

---

---

## REFERENCES

- [1] M. Silari, E. Mauro, Nucl. Instr. and Meth. in Phys. Res. A 605 (2009) 249.
- [2] S. Agosteo, M. Magistris, M. Silari, Nucl. Instr. and Meth. in Phys. Res. A 545 (2005) 813.
- [3] M. Silari, L. Ulrici, Nucl. Instr. and Meth. in Phys. Res. A 526 (2004) M510.
- [4] V.I. Gol'danskii, Yu.P. Nikitin, I.L. Rozentel, Kinematic methods in high-energy physics, Chur, Switzerland: Harwood Acad. Publ., 1989 (Soviet Scientific Rev. Suppl. Ser. Physics. Vol. 2).
- [5] FAIR Technical Design Report SIS100, December 2008.
- [6] A. Fertman et al., Nucl. Instr. Meth. Phys. Res. B 260 (2007) 579.
- [7] I. Strasik et al., Nucl. Instr. Meth. Phys. Res. B 266 (2008) 3443.
- [8] I. Strasik, E. Mustafin, T. Seidl, M. Pavlovic, Nucl. Instr. Meth. Phys. Res. B 268 (2010) 573.
- [9] I. Strasik, E. Mustafin, M. Pavlovic, Phys. Rev. Sp. Topics – Acc. and Beams 13 (2010) 071004.
- [10] N. V. Mokhov and W. Chou (Eds.), Beam Halo and Scraping, The 7th ICFA Miniworkshop on High Intensity High Brightness Hadron Beams, Wisconsin, USA, 13 - 15 September 1999.
- [11] J. Alonso, Beam loss working group report, Proc. of the 7th ICFA Miniworkshop on High Intensity High Brightness Hadron Beams, Wisconsin, USA, 13 - 15 September 1999.
- [12] N.M. Sobolevsky, Monte Carlo method for calculating the interaction of the particles with matter, INR RAN, 2007 (in Russian).
- [13] N. Metropolis, Los Alamos Science Special Issue (1987) 125.
- [14] R. Eckhardt, Los Alamos Science Special Issue (1987) 131.
- [15] W.W.Scott, R.G.Alsmiller Jr, ORNL-RSIC-22 (1968).

- 
- [16] K. Wille, *The Physics of Particle Accelerators*, Oxford University Press (2000).
- [17] A.V. Dementyev, N.M. Sobolevsky, *Radiation Measurements* 30 (1999) 553, <http://www.inr.ru/shield/>.
- [18] N. Sobolevsky, Modification of the Monte-Carlo particle transport code SHIELD for needs of the FAIR project, GSI internal note, DOC-2008-Nov-116-1, 16 November 2008.
- [19] G. Battistoni, S. Muraro, P.R. Sala et al., *The FLUKA Code: Description and Benchmarking*, Proc. of the Hadronic Shower Simulation Workshop 2006, Fermilab 6-8 September 2006, AIP Conference Proceeding 896 (2007) 31.
- [20] A. Fasso, A. Ferrari, J. Ranft, P.R. Sala, FLUKA: a multi-particle transport code, CERN-2005-10 (2005), INFN/TC\_05/11, SLAC-R-773.
- [21] N.V. Mokhov, "The Mars Code System User's Guide", Fermilab-FN-628 (1995).
- [22] N.V. Mokhov, K.K. Gudima, C.C. James et al, *Radiation Protection and Dosimetry*, vol. 116, part 2 (2005) 99; Fermilab-Conf-04/053 (2004).
- [23] N.V. Mokhov, K.K. Gudima, S.G. Mashnik et al., "Physics Models in the MARS15 Code for Accelerator and Space Applications", in Proc. of International Conference on Nuclear Data for Science and Technology, Santa Fe, NM, 2004, AIP Conf. Proc. 769, part 2 (2004) 1618; Fermilab-Conf-04/269-AD.
- [24] N.V. Mokhov, S.I. Striganov, "MARS15 Overview", Fermilab-Conf-07/008-AD (2007); in Proc. of Hadronic Shower Simulation Workshop, Fermilab, September 2006, AIP Conf. Proc. 896 (2007) 50.
- [25] <http://www-ap.fnal.gov/MARS/>

## References

---

- [26] I. Remec and R.M. Ronningen, Benchmarking of Heavy Ion Transport Codes, Proc. of the 14th International Symposium on Reactor Dosimetry, May 22-27, 2011, Bretton Woods, USA.
- [27] L. Beskrovnaia et al., Nucl. Instr. and Meth. in Phys. Res. B 266 (2008) 4058.
- [28] N. Mokhov, S. Striganov, Recent verifications in MARS15, Proc. of Hadronic Shower Simulation Workshop, Fermilab, September 6 – 8, 2006.
- [29] P. Sala, G. Battistoni, Benchmarking of the FLUKA code, Proc. of Hadronic Shower Simulation Workshop, Fermilab, September 6 – 8, 2006.
- [30] J. B. Cumming, R. W. Stoenner and P. E. Haustein, Phys. Rev. C 14 (1976) 1554.
- [31] N. T. Porile, G. D. Cole, and C. R. Rudy, Phys. Rev. C 19 (1979) 2288.
- [32] J. B. Cumming, P. E. Haustein, R. W. Stoenner, L. Mausner and R. A. Naumann, Phys. Rev. C 10 (1974) 739.
- [33] E. Kozlova et al., Nuclear Technology, Vol. 168 (2009) 747.
- [34] I. Strasik et al., Nuclear Technology, Vol. 168 (2009) 643.
- [35] L. Beskrovnaia et al., Physics of Particles and Nuclei letters, vol. 8 (2011) 364.
- [36] J. B. Cumming, P. E. Haustein, T. J. Ruth, and G. J. Virtes, Phys. Rev. C 17 (1978) 1632.
- [37] K. H. Hicks et al., Phys. Rev. C 26 (1982) 2016.
- [38] Y. K. Kim et al., Nucl. Phys. A 578 (1994) 621.



- 
- [39] Yu. E. Titarenko, V. F. Batyaev, V. M. Zhivun, A.B. Koldobsky, Yu.V. Trebukhovsky, E.I. Karpikhin, R.D. Mulambetov, S.V. Mulambetova, Yu.V. Nekrasov, A.Yu. Titarenko, K.A. Lipatov, B.Yu. Sharkov, A.A. Golubev, A.D. Fertman, V.I. Turtikov, A.V. Kantsyrev, I.V. Roudskoy, G.N. Smirnov, V. S. Barashenkov, K. Gudima, M. Baznat, S.G. Mashnik, and R.E. Prael, in Proc. of the AccApp'03 Meeting, San Diego, USA, 2003.
- [40] H. Yashima et al., *Radio Chimica Acta* 91 (2003) 689.
- [41] H. Yashima et al., *Phys. Rev. C* 66 (2002) 044607.
- [42] H. Yashima et al., *Radiat. Prot. Dosim.* 112 (2004) 195.
- [43] H. Yashima et al., *Nucl. Instrum. and Meth. in Phys. Res. B* 226 (2004) 243.
- [44] T. Nakamura, L. Heilbronn, *Handbook on Secondary Particle Production and Transport by High-Energy Heavy Ions*, World Scientific Publishing Co Pte. Ltd., 2006, ISBN 981-256-558-2.
- [45] T. Ogawa et al., Measurement and simulation of the radionuclide product yields in iron from 400 AMeV carbon ions, Proc. of SATIF10, Geneva, Switzerland, 2-4 June 2010, p. 281.
- [46] I. Strasik, *Activation Study of High-Energy Heavy-Ion Accelerators*, Dissertation Thesis, Slovak University of Technology, Faculty of Electrical Engineering and Information Technology, Department of Nuclear Physics and technology, Bratislava, 2009.
- [47] J. Alonso, Review of ion accelerators, LBL-29228, DE90 015430.
- [48] E. Mustafin et al., *Radiation Effects & Defects in Solids*, Vol. 164 (2009) 460.
- [49] A. Ferrari, P.R. Sala, R. Guaraldi, F. Padoani, *Nucl. Instr. Meth.* B71, (1992) 412.
- [50] A. Ferrari et al., FLUKA: a multi-particle transport code (Program version 2011), CERN-2005-010, INFI TC\_05/11, SLAC-R-773, 12 October 2005.

## References

---

- [51] H.A. Bethe, , Ann. Physik 5 (1930) 325.
- [52] H.A. Bethe, Z. Phys. 76 (1932) 293.
- [53] H.A. Bethe and W. Heitler, On the stopping of fast particles and on the creation of positive electrons, Proc. Roy. Soc. A146 (1934) 83.
- [54] F. Bloch, Ann. Physik 16 (1933) 285.
- [55] F. Bloch, Z. Phys. 81 (1933) 363.
- [56] E. Fermi, Phys. Rev. vol. 57 (1940) 485.
- [57] W.H. Barkas, W. Birnbaum, F.M. Smith, Phys. Rev. 101 (1956) 778.
- [58] W.H. Barkas, J.N. Dyer, H.H. Heckman, Phys. Rev. Lett. 11 (1963) 26 (Erratum 11, 138 (1963)).
- [59] N.F. Mott, The scattering of fast electrons by atomic nuclei, Proc. R. Soc. London A124 (1929) 425.
- [60] Insoo Jun, Wousik Kim and R. Evans, IEEE Trans. Nucl. Sci. 56 (2009) 3229.
- [61] A. Fasso, Progress in Nucl. Science and Tech., vol. 2, (2011) 769.
- [62] A. Fasso, A. Ferrari, J. Ranft, P.R. Sala, New developments in FLUKA modelling hadronic and EM interactions, Proc. 3rd Workshop on Simulating Accelerator Radiation Environments (SARE 3), 7-9 May 1997, KEK, Tsukuba (Japan). Ed. H. Hirayama, KEK Proceedings 97-5 (1997) 32.
- [63] H.A. Bethe, Phys. Rev. vol. 89 (1953) 1256.
- [64] <http://www-linux.gsi.de/~weick/atima/>
- [65] P.V.Vavilov, Soviet Physics JETP 5 (1957) 749.
- [66] J. Lindhard, A.H. Soerensen, Phys. Rev. A53 (1996) 2443.
- [67] H. Bichsel, D.E. Groom, and S.R. Klein, Phys. Rev., D66 (2002) 010001-195.

- 
- [68] J.F. Ziegler, J.B. Biersack, U. Littmark, The stopping and range of ions in solids, Vol.1, Pergamon Press (1985).
- [69] O.B. Firsov, Sov. Phys. JETP 5 (1957) 1192.
- [70] P. Hvelplund, Dan. Mat. Fys. Medd. Dan. Vid. Selsk. 38 no.4 (1971).
- [71] S.I. Striganov, On the theory and simulation of multiple Coulomb scattering of heavy charged particles, Tech. rep., Fermilab-Conf-04/056-AD (2004).
- [72] I.L. Rakhno, Modeling Heavy Ion Ionization Energy Loss at Low and Intermediate Energies, FERMILAB-FN-0835-APC November 2009.
- [73] T.E. Pierce and Marshall Blann, Phys. Rev. 173 (1968) 390.
- [74] F. Hubert, R. Bimbot and H. Gauvin, Nucl. Instrum. Meth. in Phys. Res. B 36 (1989) 357.
- [75] B.A. Weaver, A.J. Westphal, Nucl. Instrum. and Meth. in Phys. Res. B 187 (2002) 285.
- [76] J.F. Ziegler, J.P.Biersack, M.D. Ziegler, "SRIM: The Stopping and Range of Ions in Matter", <http://www.srim.org>.
- [77] H. Weick, H. Geissel, C. Scheidenberger et al., Nucl. Instrum. Meth. Phys. Res. B 164 - 165 (2000) 168.
- [78] "Physical Reference Data," National Institute of Standards and Technology, <http://physics.nist.gov/PhysRefData/contents.html>.
- [79] K. Tasaka, DCHAIN2: A Computer Code for Calculation of Transmutation of Nuclides, JAERI-M-8727, 1980.
- [80] P. Aarnio, Decay and transmutation of nuclides, CMS-NOTE-1998/086, CERN (1998).
- [81] M. Cavinato et al, Physics Letters B 382 (1996) 1.
- [82] G.D. Harp, J.M. Miller and B.J. Berne, Phys. Rev. 165 (1968) 1166.
- [83] G.D. Harp and J.M. Miller, Phys. Rev. C 3 (1971) 1847.

## References

---

- [84] M. Cavinato et al., Phys. Letters B 405 (1997) 219.
- [85] M. Cavinato et al., Nuclear Physics A 643 (1998) 15.
- [86] M. Cavinato et al., Nuclear Physics A 679 (2001) 753.
- [87] M. Blann, Phys. Rev. C 23 (1981) 205.
- [88] M. Blann, Phys. Rev. C 31 (1985) 1245.
- [89] B.A. Remington, M. Blann and G.F. Bertsch, Phys. Rev. C 35 (1987) 1720.
- [90] B.A. Remington et al., Phys. Rev. C 38 (1988) 1746.
- [91] E. Fabrici et al., Phys. Rev. C 40 (1989) 2548.
- [92] E. Fabrici et al., Phys. Rev. C 42 (1990) 2163.
- [93] E. Fabrici et al., Z. Phys. A 338 (1991) 17.
- [94] I. Cervesato et al., Phys. Rev. C 45 (1992) 2369.
- [95] M. Cavinato et al., Z. Phys. A 347 (1994) 237.
- [96] C. Brusati et al., Z. Phys. A 353 (1995) 57.
- [97] H. Sorge, Phys. Rev. C 52, 3291 (1995).
- [98] H. Sorge, H. Stöcker, and W. Greiner, Ann. Phys. 192 (1989) 266.
- [99] H. Sorge, H. Stöcker, and W. Greiner, Nucl. Phys. A 498 (1989) 567c.
- [100] K. Chen, Z. Fraenkel, G. Friedlander, J. R. Grover, J. M. Miller, and Y. Shimamoto, Phys. Rev. 166 (1968) 949.
- [101] F. Ballarini et al., Nuclear models in FLUKA: present capabilities, open problems and future improvements, SLAC-PUB-10813, October 2004.
- [102] A.S.Botvina, A.V.Dementyev, O.N.Smirnova, N.M.Sobolevsky, V.D.Toneev. MSDM - Multi Stage Dynamical Model. In International Codes and Model Intercomparison for Intermediate Energy Activation Yields, Eds. R.Michel and P.Nagel, NSC/DOC(97)-1, NEA/P&T No 14, OECD, Paris, 1997, p.307.

- 
- [103] N. M. Sobolevsky, Numerical investigation of interaction of hadrons and nuclei with complex matter, Second doctoral dissertation INR RAS Moscow, 2003, In Russian. (Н.М. Соболевский, Компьютерные исследования взаимодействия адронов и ядер со сложными средами, Докторская диссертация, ИЯИ РАН, Москва 2003).
- [104] V.D.Toneev, K.K.Gudima, Nucl. Phys. A 400 (1983) 173c.
- [105] P.Danielewicz, G.F.Bertsch, Nucl. Phys. A 533 (1991) 712.
- [106] V.S. Barashenkov. Interaction cross-section of the particles and nuclei with nuclei, preprint JINR, Dubna, 1993.
- [107] V.S. Barashenkov, Nucleon-nucleus cross-sections, JINR, P2-89-770, Dubna, 1989.
- [108] V.S. Barashenkov. Pion-nucleus cross-sections, JINR P2-90-158, Dubna, 1990.
- [109] V.S.Barashenkov, A.Polanski. Electronic Guide for Nuclear Cross-Sections. JINR E2-94-417, Dubna, 1994.
- [110] B.S.Sychev. Interactions cross-sections of high-energy hadrons with atomic nuclei, MRTI RAS, Moscow, 1999.
- [111] K.K.Gudima, S.G.Mashnik, V.D.Toneev, Nucl. Phys. A401 (1983) 329.
- [112] K.K.Gudima, G.A.Ososkov, V.D.Toneev, Sov. J. Nuclear Phys. 21 (1975) 260 (in Russian).
- [113] E.Fermi, Progr. Theor. Phys. 5 (1950) 570.
- [114] A.S.Botvina, A.S.Iljinov, I.N.Mishustin et al., Nucl.Phys. A475 (1987) 663.
- [115] G.D.Adeev, A.S.Botvina, A.S.Iljinov et al. A Method of Calculation of Mass and Energy Distributions of Fission Residuals in Reactions Induced by Intermediate Energy Particles.Preprint INR, 816/93, Moscow, 1993 (in Russian).

## References

---

- [116] J.P.Bondorf, A.S.Botvina, A.S.Iljinov et al., *Physics Reports* 257 (1995) 133.
- [117] A.S.Botvina, A.S.Iljinov, I.N. Mishustin, *Nucl.Phys. A*507 (1990) 649.
- [118] N.V. Mokhov, K.K. Gudima, S.G. Mashnik, I.L. Rakhno, and S.I. Striganov, *Towards a Heavy-Ion Transport Capability in the MARS 15 Code*, Tech. rep., Fermilab-Conf-04/052 (2004).
- [119] Gudima, K. K., Mashnik, S. G., and Sierk, A. J. *User manual for the code LAQGSM*, LA-UR-01-6804, Los Alamos National Laboratory (2001).
- [120] V. S. Barashenkov, H. Kumawat, *Integral nucleus-nucleus cross-sections*, JINR E2-2003-128, Joint Inst. for Nuclear Research (2003).
- [121] M. V. Kossov, *Eur. Phys. J. A* 14 (2002) 377.
- [122] Mashnik, S. G et al., *CEM03.03 and LAQGSM03.03 Event Generators for the MCNP6, MCNPX, and MARS15 Transport Codes*, LANL Report LA-UR-08-2931, arXiv:0805.0751v2 [nucl-th] 12 May 2008.
- [123] S. Furihata, *Nucl. Instrum. and Methods in Phys. Res. B* 171 (2000) 251; Furihata, S. *The GEM code version 2. User's manual*, Mitsubishi Research Institute, Inc., Tokyo, Japan (2001).
- [124] *Verordnung über den Schutz vor Schäden durch ionisierende Strahlen*, 20. Juli 2001 (BGBl. I S. 1714; 2002 I S. 1459).
- [125] Gordon R. Gilmore, *Practical Gamma-Ray Spectrometry*, Warrington, UK, 2008, ISBN: 978-0-470-86196-7.
- [126] H. Reeg and N. Schneider, in *Proceedings of the Fifth European Workshop on Diagnostics and Beam Instrumentation DIPAC2001*, ESRF, Grenoble, France, 2001, (ESRF, Grenoble, France, 2001), PS08.
- [127] L.P. Ekström and R.B. Firestone, *WWW Table of Radioactive Isotopes*, database version 2/28/99 from URL <http://ie.lbl.gov/toi/index.htm>.

- 
- [128] C.L. Dunford and T.W. Burrows, Online Nuclear Data Service, Report IAEA-NDS-150 (NNDC Informal Report NNDC/ONL-95/10), Rev. 12/01 (2012), International Atomic Energy Agency, Vienna, Austria.
- [129] S. S. Belyshev, A. A. Kuznetsov, A. S. Kurilik, K. A. Stopani, Automation of data-processing for gamma-activation experiment, In Proc. of 58 International Workshop on nuclear spectroscopy and nuclear structure, Nucleus-2008, Moscow (2008) 282. In Russian. (Бельшев С. С., Кузнецов А. А., Курилик А. С., Стопани К. А., Автоматизация обработки данных гамма-активационных экспериментов. 58 Международное совещание по ядерной спектроскопии и структуре атомного ядра "Ядро 2008". Москва, 2008 г, с. 282).
- [130] I. Sihver et al., Adv. Space Res. 45 (2010) 892–899.

---



---

## ACKNOWLEDGEMENTS

I would like to express my greatest thanks to my family, colleagues and friends – all the people who helped and supported me during these years.

I am grateful to Prof. Dr. Ulrich Ratzinger for giving me the opportunity to accomplish this work, for his support and patience, and of course for interesting discussions not only in physics but also in various other topics. Thank you for your good mood!

I address many thanks to my supervisor Dr. Edil Mustafin for his trust and for giving me enough freedom for creativity; for numerous conversations and useful advice.

Many thanks to Prof. Dr. Oliver Kester for his support and interest in students' life, for being always positive and inspiring.

I would like to sincerely thank Prof. Dr. Oliver Boine-Frankenheim for being friendly and helpful, for supporting me in my attempts to get closer to accelerator physics, for workshops and schools that I could attend thanks to his help.

Special thanks go to Dr. Giuliano Franchetti who motivated me to come to GSI for a PhD, shared many interesting ideas and gave a lot of advice.

I address my gratitude to Dr. Peter Spiller and Dr. Andreas Tauschwitz who provided enough support and beam time for the experiments; and to Dr. Bettina Lommel and Targetlabor team for preparing endless number of targets, which made this work possible.

I would like to express my heartfelt gratitude to my collaborators Dr. Lyudmila Latisheva and Dr. Nikolai Sobolevsky for SHIELD simulations, Dr. Nikolai Mokhov for MARS simulations and Dr. Hiroshi Iwase for PHITS simulations. I very much appreciate their cooperation, their help in understanding the physics of nuclear interactions and theories behind the codes.

---

I also want to thank Prof. Dr. M. Pavlovic. He supported me a lot in a difficult task of scientific writing in English. Marius, thank you for the friendly atmosphere and “See you next time! ☺”

Many thanks to Dr. Ivan Strasik, Anton Belousov and Dr. Stefan Sorge who helped in preparing the experimental setup and in measuring the spectra.

My endless gratitude to Johanna Otto for her patience in correcting and improving the translation of Zusammenfassung. Et bien sûr pour CERN- and Niederweimar- times ;)

I’m especially grateful to Dr. Rudolf Tiede for his help and support that were so important during the final stage of my work!

Also I would like to thank all my colleagues from former FAIR AT and presently BPhy department for creating a good atmosphere and for making it a real pleasure to work here.

My special infinite thanks to Prof. Dr. B. S. Ishkhanov who one day believed that I could make it, who supported and inspired me from my first steps, who gave me knowledge and advice.

My sincere gratitude to all my friends for the beautiful times we had, for nice conversations, for having fun together, for your support and belief.

And finally thanks to my family for always being there and encouraging me day by day.

---

---

## CURRICULUM VITAE

### Vera Chetvertkova

September, 19, 1984

Born in Obninsk, Russia



### Education

April 2009 – Present: Goethe University, Institute for Applied Physics, Frankfurt am Main, Germany: PhD student,

Subject of the thesis: "Verification of Monte Carlo Transport Codes by Activation Experiments".

Supervisors: Prof. Dr. U. Ratzinger (IAP), Dr. E. Mustafin (GSI)

2002 – 2008: Lomonosov Moscow State University, Physics Faculty, Moscow, Russia: Masters degree in nuclear and particle physics,

Subject of the thesis: "Photodisintegration of  $^{209}\text{Bi}$ ".

Supervisors: Prof. Dr. Ishkhanov, I. Makarenko

### Research experience

2009 – present: GSI Helmholtzzentrum für Schwerionenforschung, Accelerator Physics department, Darmstadt, Germany: PhD Student.

Field of studies: Activation of accelerator relevant materials by heavy-ion beams.

2008 – 2009: Skobeltsyn Institute of Nuclear Physics (Moscow State University), Moscow, Russia: junior researcher.

Field of studies: photonuclear reactions, photodisintegration of tin isotopes.

---

## List of peer-reviewed publications

1. I. Strašík, V. Chetvertkova, E. Mustafin, M. Pavlovič, A. Belousov, Depth-profiling of residual activity of  $^{237}\text{U}$  fragments as a range-verification technique for  $^{238}\text{U}$  primary ion beam, *Physical Review Special Topics Accelerators and Beams* 15, 071001 (2012).
2. B.S. Ishkhanov, S.Yu. Troschiev, V.A. Chetvertkova, Yields of photonuclear reactions on Sn isotopes at 29.1 MeV, *Bulletin of the Russian Academy of Sciences: Physics*, 76, 481 (2012).
3. V. Chetvertkova, I. Strasik, A. Belousov, H. Iwase, N. Mokhov, E. Mustafin, L. Latysheva, M. Pavlovic, U. Ratzinger, N. Sobolevsky, Activation of aluminum by argon: Experimental study and simulations, *Nuclear Instruments and Methods in Physics Research B* 269, 1336 (2011).
4. B.S. Ishkhanov, S.Yu. Troschiev, V.A. Chetvertkova, Photodisintegration of Sn isotopes, *Bulletin of the Russian Academy of Sciences. Physics*, 75, 558 (2011).
5. V.V. Abramov et al., Preparation of new polarization experiment SPASCHARM at IHEP, *Journal of Physics: Conference Series*, 295, 134 (2011).
6. V.V. Varlamov, B.S. Ishkhanov, V.N. Orlin, V.A. Chetvertkova, Evaluated cross-sections of the  $\Sigma(\Gamma, \text{NX})$  and  $\Sigma(\Gamma, 2\text{NX})$  reactions on  $^{112,114,116,117,118,119,120,122,124}\text{Sn}$  isotopes, *Bulletin of the Russian Academy of Sciences. Physics*, 74, 833 (2010).
7. Belyshev S.S., Ermakov A.N., Ishkhanov B.S, Kapitonov I.M., Makarenko I.V., Chetvertkova V.A., Shvedunov V.I. Yields of multiparticle photoneutron reactions on  $^{209}\text{Bi}$ , *Vestnik MSU (Herald Of Moscow State University)*, vol 3, *Physics & Astronomy*, 3, 57 (2008).
8. Asanov Zh.A, Ermakov A.N., Ishkhanov B.S, Kapitonov I.M., Kyaw Kyaw Htun, Makarenko I.V., Salakhutdinov D.R., Chetvertkova V.A, Multiparticle photonuclear reactions on  $^{203}\text{Tl}$  isotope, *Bulletin of the Russian Academy of Sciences. Physics*, 71, 332 (2007).